CARBON NANOTUBE FORESTS:

SYNTHESIS, PATTERNING, MILLING, MECHANICS, AND APPLICATIONS

A Thesis

presented to

the Faculty of the Graduate School

at the University of Missouri

In Partial Fulfillment

of the Requirements for the Degree

Master of Science

---

by

BENJAMIN F DAVIS

Dr. Matthew R. Maschmann, Thesis Supervisor

MAY 2018

The undersigned, appointed by the dean of the Graduate School, have examined the thesis entitled

CARBON NANOTUBE FORESTS:
SYNTHESIS, PATTERNING, MILLING, MECHANICS, AND APPLICATIONS

presented by Benjamin F Davis,

a candidate for the degree of master of science,

and hereby certify that, in their opinion, it is worthy of acceptance.

Professor Matthew Maschmann

Professor Tommi White

Professor Zheng Yan

DEDICATION

To my family, you've given me relentless love, reassurance, nourishment, and motivation. I would be lost without it. To my friends, you've entertained, questioned my knowledge, distracted my focus, and I'd be joyless without you. To the dogs in my life, you've given me enough loose fur to weave an awful quilt. I'd have it no other way. To my girlfriend, Christy, you have supported me day in and day out and have inspired a happy future. You are the human to my robot and the art to my science.

ACKNOWLEDGMENTS

I express my genuine gratitude to my advisor, Dr. Matt Maschmann, for his endless encouragement and support during my academic career. His guidance and confidence in me has helped me accomplish so many of my life goals. My graduate research career has been smooth-sailing and free of the hardships typically associated with advisor-student relationships. I am forever indebted. I also thank my thesis committee members, Dr. Tommi White and Dr. Zheng Yan, for their provision and accommodation during the writing and editing process. You have shared many valuable insights during this time.

I thank my collaborators from AFRL, Vanderbilt, MIT, and New Hampshire, for numerous fruitful discussions and direction. My colleagues here at Mizzou have also been a guiding light for my research, career, and perspective; thank you Joe, Matt, Taher, Ryan, and Dami. I've learned much about science and the world from you. Finally, I'd like to acknowledge and thank the U.S. Department of Defense and the Air Force Office of Scientific Research for funding my projects and for providing visionary direction to the field of nanomaterials development.

TABLE OF CONTENTS

Page

LIST OF FIGURES

LIST OF TABLES

ABSTRACT

Carbon nanotube (CNT) forests are a nano-structured material consisting of vertically oriented carbon nanotubes. The material has many exceptional and unique physical properties that have motivated considerable research in the past 10 years. CNT forests hold promise for diverse applications in the fields of thermal interfaces, mechanical interfaces, electrical interconnects, molecular sensors, battery cathodes, energy storage devices, and low reflectance coatings.

This thesis seeks to introduce the reader to nanotechnology and nano-carbon materials, and explain several processes for creating, patterning, shaping, modifying physical properties, testing, and using carbon nanotube forests in novel applications. The thesis is organized so that each chapter describes an individual project or publication and is independent of other chapters.

CHAPTER 1 - INTRODUCTION

Nanotechnology & Nanomaterials

Nanotechnology is the field of science which aims to create, manipulate, monitor, and utilize material structures that have critical features in the nanoscale (1-100 billionths of a meter), termed nanomaterials. These aims require a deep understanding of the properties and interactions that arise uniquely as the size and surface characteristics of materials reach the nanoscale. The field is still emerging, in the larger context of materials science and physics, and began to flourish no earlier than the 1960s. Nanomaterials physical size is often less than the length scale associated with physical phenomena: mean free path of phonons and electrons, grain size of metals, diffusion length of reactive materials, etc. The most important breakthroughs in the field involve discovering the unique physical, chemical, mechanical, thermal, and electrical properties of nanomaterials that result from the large surface-area-to-volume ratio and unique molecular structures. Hence, a great deal of scientific research is currently being directed towards creating and improving how nanomaterials are synthesized, characterized, assembled, and understood. The ultimate goal of nanotechnology is integrating nanomaterials into real-world functional devices and applications.

Carbon Nanotubes

Carbon nanotubes (CNTs) are a family of nanomaterials and are an allotrope of carbon with a hollow cylindrical structure. The typical CNT diameter is in the range of nanometers and the length is highly variable, from nanometers to centimeters. Since the first discovery of CNTs in 1991[13], tremendous research has sought to understand the

structure, physical properties, growth mechanisms, and characterization methods. Figure 1-1 shows the carbon allotropes and their effective dimensionality due to the nanostructure.

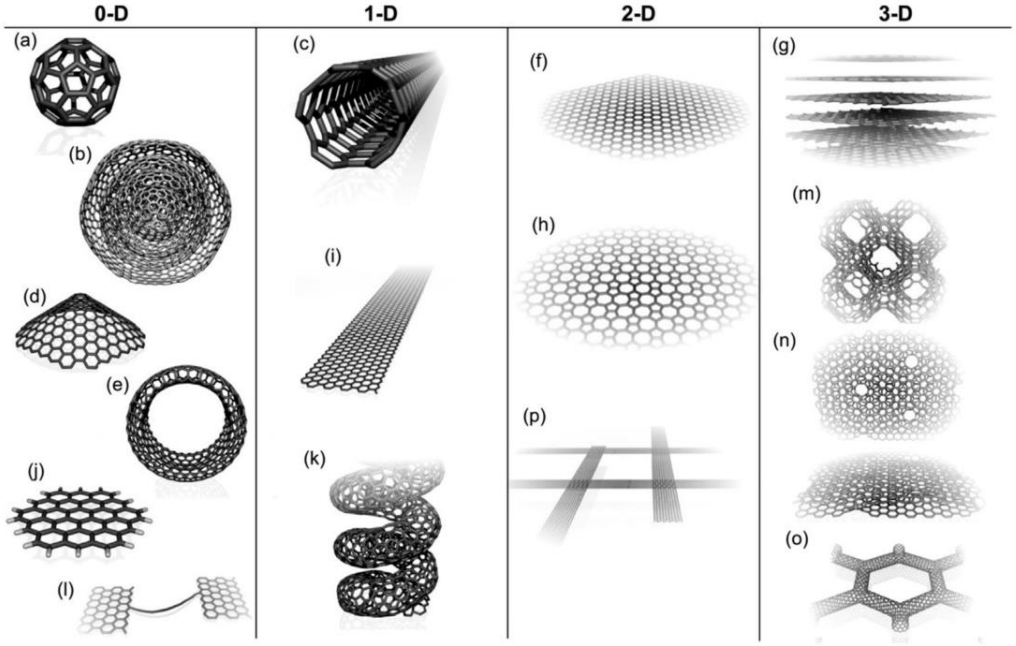

Figure 1-1. Allotropes of nano-structured carbon, organized by their dimensionality. CNT is shown in 1-D (c) [11].

History

Fullerenes, a family of large molecules consisting of strongly bonded carbon, were discovered in 1985[14]. By 1991, the structure of CNTs were theoretically proposed by Millie Dresselhaus, as extended C_{60} buckyballs. The first experimental evidence of their structure came later in 1991 by Sumio Iijima[13], where multiwall CNTs were directly observed in a high-resolution transmission electron microscope. Numerous breakthrough reports of CNT properties and application have since been reported, due to the huge array of applications supported by CNTs. Figure 1-2 shows the progression of CNT publications and patents in the previous decade, with trends presumably at the same pace still today.

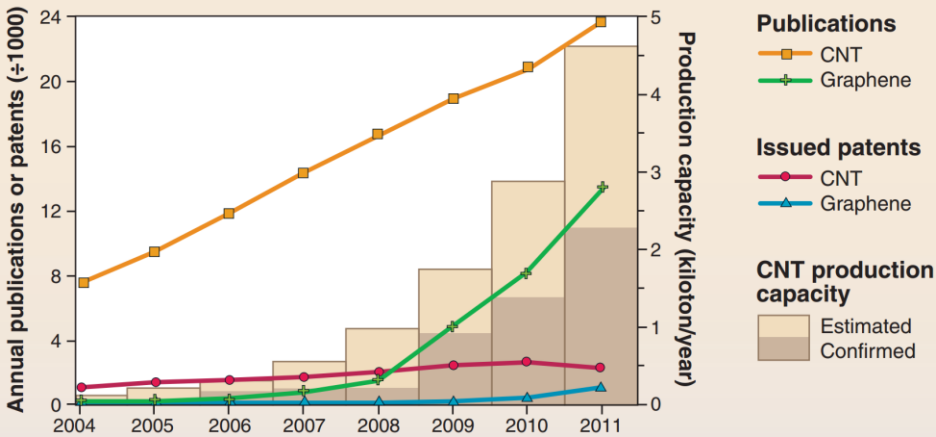

Figure 1-2. Peer-reviewed publications, patents, and production capacity of CNTs [4].

Structure of CNTs

CNTs have an atomic structure that is best understood by first understanding their 2D analog, graphene. Graphene is a planar sheet of carbon atoms, where each atom is bonded to three neighboring atoms via sp^2 hybridized bonds (σ-bonds) with equilibrium bond length of 1.42 Å. The carbon atom's fourth valence shell electron forms a delocalized π-bond which is oriented perpendicular to the plane of σ-bonding. The planar crystal structure can be seen in Figure 1-3. This bond structure has a lattice energy of 7.4 eV per atom, which is one of the strongest bonds found in nature, 37% higher than the lattice energy of diamond.

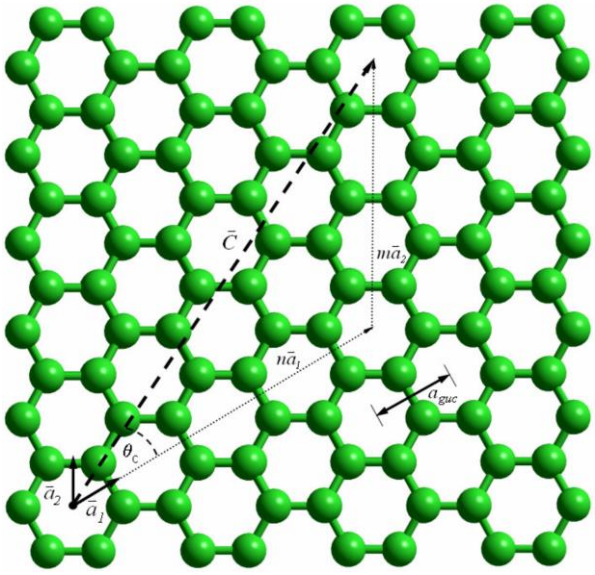

Figure 1-3. Graphene crystal structure, showing unit cell length a_{guc}, unit cell base vectors $\bar{a}_1$ and $\bar{a}_2$, chiral vector $\bar{C}$, chiral indices (n,m), and chiral angle θ_c.

A CNT may be thought of as a sheet of graphene rolled along the chiral vector $\bar{C}$. This chiral vector determines structural properties of the CNT, as listed in Table 1-1. The chiral vector also has a large effect on the electrical properties, determining whether it behaves like a metallic conductor or a semi-conductor.

Table 1-1. Structural Properties of single wall carbon nanotubes

Property	**Symbol**	**Equation**	**Value/Limits**
C-C σ-bond length, sp^2	a_{c-c}	*constant*	1.42 Å
Unit cell length	a_{guc}	$\sqrt{3}a_{c-c}$	2.46 Å
Unit cell base vectors	$\bar{a}_1$, $\bar{a}_2$		60° from each other
Chiral indices	(n,m)		
Chiral vector	$\bar{C}$	$n\bar{a}_1 + m\bar{a}_2$	
Diameter	d_{CNT}	$\frac{a_{guc}}{\pi}\sqrt{n^2 + nm + m^2}$	SWCNTs typically less than 50 Å
Elastic modulus	E_g	*constant*	1.06 TPa
Effective graphitic thickness	t_g	*constant*	3.4 Å
Formation energy	U_r	$\frac{\sqrt{3}E_g {t_g}^3 {a_{guc}}^2}{24{d_{CNT}}^2}$	Energy to roll graphene into a CNT
Chiral angle	θ_g	$\tan^{-1}(\frac{\sqrt{3}m}{m+2n})$	

Metallic conducting CNTs		$\lvert n-m\rvert = 3q$	$q = 0,1,2,\ldots$
Semi-conducting CNTs		$\lvert n-m\rvert \neq 3q$	$q = 0,1,2,\ldots$
Semi-conducting bandgap	U_{gap}	$= a_{guc}\frac{\zeta}{d_{CNT}}$	$\zeta = 2.5 - 3.2eV$ Hopping parameter
Three chiralities of CNTs	Zig-zag Arm-chair Chiral	$m = 0$ $m = n$ All other combinations	$\theta_g = 0°$ $\theta_g = 30°$ $0° < \theta_g < 30°$
Chiral parameter	P_{CNT}	$\gcd(2m+n, 2n+m)$	integer
Unit cell length	T_{nuc}	$a_{guc}\frac{\sqrt{3(n^2+nm+m^2)}}{P_{CNT}}$	
CNT length	L_{CNT}	qT_{CNT}	$q = 1,2,3,\ldots$
Number of atoms per unit cell	N_C	$\frac{4(n^2+nm+m^2)}{P_{CNT}}$	

CNTs can also have multiple walls (MWCNTs), consisting of several single-wall CNTs that are coaxially nested. Each wall of the MWCNT may have a different chirality, though these chiralities are usually complementary matched to minimize the non-bonded energy between the walls of the MWCNT. The walls are nominally spaced 3.41 Å, the interlayer spacing of graphene, but increases with higher curvature. The nested structure of a MWCNT allows it to reach diameters in excess of 100 nm, while SWCNTs are typically 5 nm or less. A depiction of chiralities and multi-walled CNTs is given in Figure 1-4.

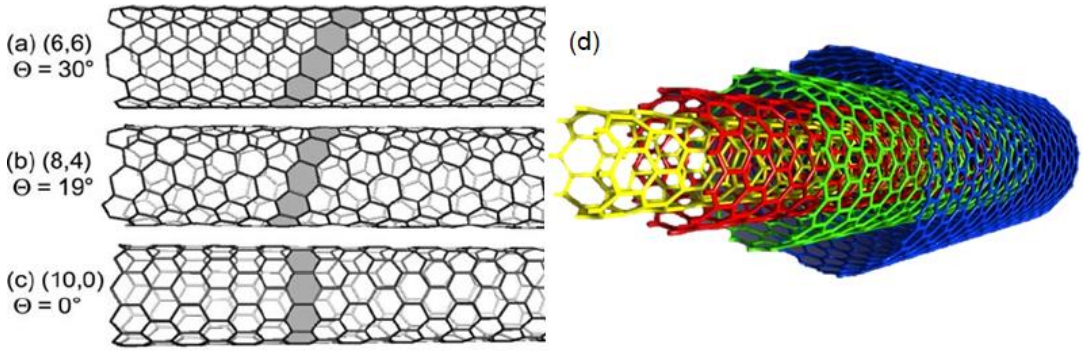

Figure 1-4. Representation of CNT chirality and of a multi-walled CNT. (a) arm-chair (b) chiral (c) zig-zag (d) multi-walled CNT.

The CNT structure discussed so far has consisted of highly idealized construction. In reality, CNTs invariably have defects of many kinds. SWCNTs may have local vacancies and bond-rotations dispersed throughout their structure, as shown in Figure 1-5. The surface of CNTs are prone to chemical reaction because of the delocalized π-electrons, so many types of organic and extended-inorganic functional groups are capable of attaching to the surface and affecting CNT properties, whether intentionally or otherwise. CNTs may also have non-constant diameter along their length, which is a result of the nucleation/catalysis process. The defects, among others degrade properties of CNTs and ultimately affect their applicability for real-world applications. An inconvenient truth of nanomaterials is that defects and impurities govern the behavior, especially in mechanical properties. As a heuristic, electrons flow on the path of least resistance so less-conductive defect regions have a less important role, whereas mechanical failure is limited by the weakest component or structure so defect regions fail first, accumulate and massively degrade bulk properties.

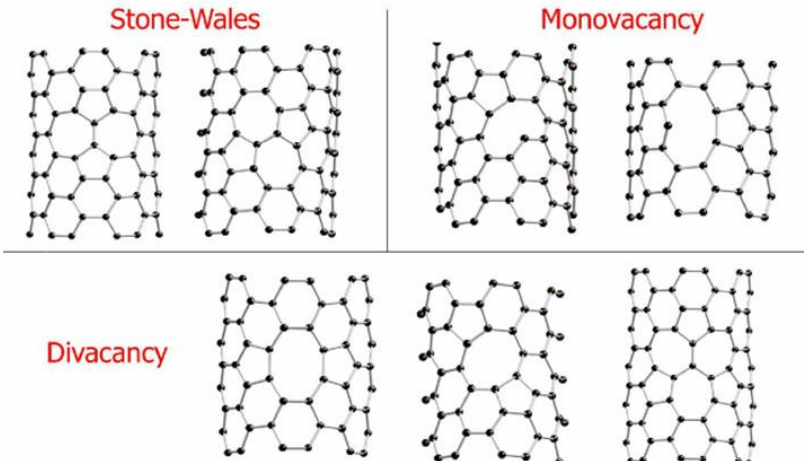

Figure 1-5. Vacancy and bond defects in single wall CNTs [7].

Physical Properties

CNTs have been shown to exhibit extreme behavior on several fronts. All properties arise due to the nature of sp^2 σ-bonds and due to CNTs huge aspect ratio (length/diameter), largest of any known material, on the order of 100 million. This tunable anisotropy lends itself well to novel functions.

Mechanical

CNTs are among the strongest and stiffest materials yet discovered, having Tensile Strength of up to 100 GPa and Elastic Modulus over 1 TPa, for ideal defect-free SWCNTs. The radial elasticity is relatively low, however, so they are extremely flexible because of their ability to flatten and form a non-circular cross-sectional shape. Above a certain diameter and below a certain number of walls, CNTs will spontaneously collapse to a flattened structure, for energy minimization, a balance between attractive van der Waals potential and high-curvature strain energy. They tend to buckle when placed under compressive, torsional, or bending stress, because of their hollow structure and high aspect ratio. Figure 1-6 illustrates some possible mechanisms of failure for various loading situations of individual SWCNTs. In MWCNTs, shells can undergo failures somewhat independently of other shells. Shells can also easily slip in position relative to each other, telescopically sliding only against weak van der Waals forces.

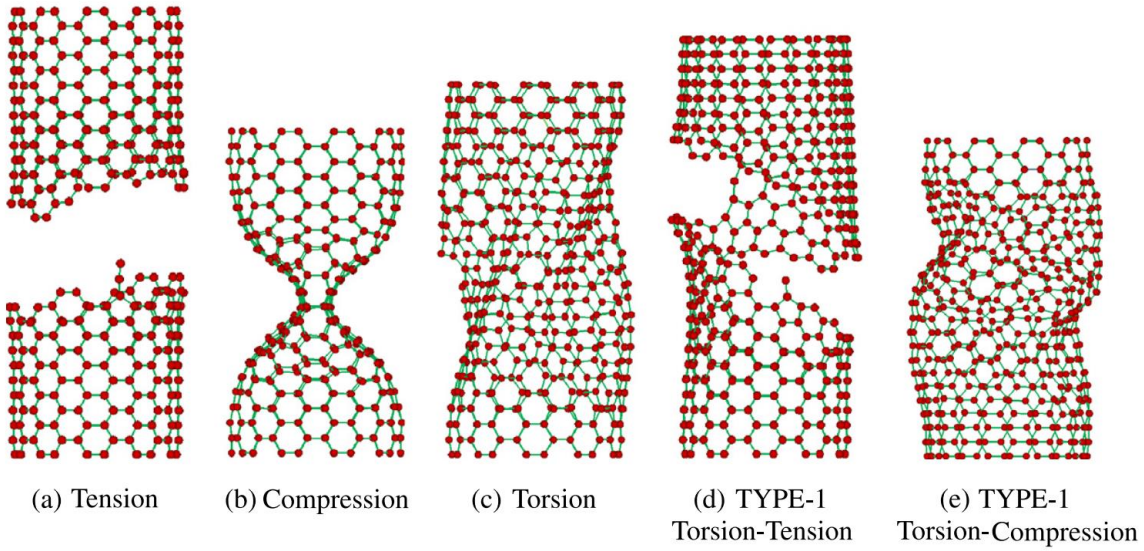

Figure 1-6. Failure modes of SWCNTs with low defect density [8].

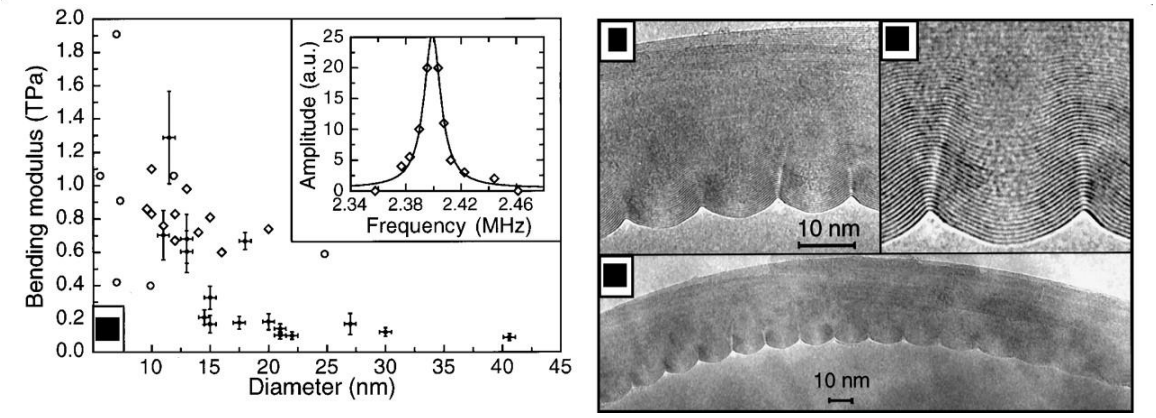

Figure 1-7. MWCNT during bending. (a) Bending modulus as a function of outer diameter, with inset dynamic response. (b,c,d) TEM images of shell structure showing wave-like distortions[2].

Thermal, Electrical, and Optical

All CNTs, regardless of chirality, are expected to exhibit ballistic phonon conduction behavior along their length and are therefore excellent thermal conductors, with k=3500 W/mK (copper k = 385 W/mK). In the transverse direction, the conductivity drastically drops to k = 2 W/mK, similar to earth soil. Crystallographic defects lead to phonon scattering, increased phonon relaxation rate, reduced mean free path and ultimately, strongly reduced thermal conductivity.

Electronic conductivity of CNTs depends on the crystal structure (chirality); CNTs are either metallic or semiconducting along the axis. In theory, metallic nanotubes can carry an electric current density of 4×10^9 A/cm^2 (1000x more than copper). Electrons propagate only along the CNT axis, so they are commonly called one-dimensional conductors. Boron or nitrogen dopant substitution in CNTs leads to p-type and n-type behavior, respectively, as in silicon. Intercalated or adsorbed dopants, however, cause different behavior in CNTs than in silicon.

Carbon nanotubes have useful optical properties such as absorption, photoluminescence, and Raman spectroscopy properties. Spectroscopic methods offer quick and non-destructive characterization; a quantifiable way of assessing CNT quality and measuring defect density.

CNT Forests

CNT forests are vertically oriented populations of CNTs with some degree of bulk parallel alignment relative to each other and usually grown normal to the surface of a substrate. The term forest arises because of the similarity with trees in a forest, or grass in a field. The size (width) of CNT forests is typically in the centimeter range and height in the millimeter range. Three levels of magnification of CNT forests are shown in Figure 1-8. Forests typically consist of many billions of individual CNTs, having a distribution of diameters, spacing, defect density, and physical properties. The collective behavior of the bulk CNT forest material is much different than the behavior of individuals. Forests are mechanically compliant and electrically and thermally conductive, albeit much less than individuals. Applications include thermal interface materials[15-17], electrical interconnects[18, 19], physical sensors[20-22], energy generation[23, 24], storage

devices[25, 26], and extreme light absorbing surfaces[27]. The main focus of this thesis is to develop an understanding of how the collective behavior of CNT forests is influenced by the constituent CNTs, which is still an ongoing field of study in nanotechnology research.

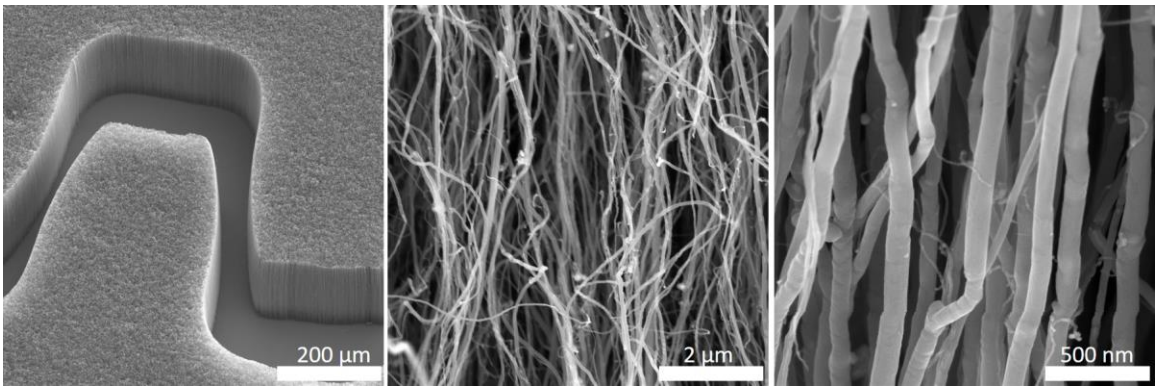

Figure 1-8. CNT forest shown at three levels of magnification. (a) isometric view of a typical patterned CNT forest, showing a high degree of CNT alignment and clean edge distinction from the substrate surface. (b,c) At higher magnification, interstitial void space, misalignment, and CNT defects become more apparent.

CNT Forest Synthesis

CNT forests are typically formed on flat substrates and self-organize by crowding during the initial stage of the growth process.[28] Growth is best accomplished by chemical vapor deposition (CVD), in which gases are passed through a furnace to react and synthesize materials on top of a catalyst particle coated substrate. The most important parameters for achieving high density and thus an aligned forest are the carbon source material, the catalyst composition, the support material composition, and the growth temperature. The carbon source must be reactive enough to dissociate into active carbon species without resulting in soot formation; some common hydrocarbon precursors include methane, ethylene, acetylene, benzene, carbon monoxide, cyclohexane, and xylene. The requirements for a CNT catalyst are that it can break down the carbon source into active

carbon species, allow for diffusion of those active carbon species, and serve as a template for the proper cylindrical morphology of CNTs. There are many options for catalysts, but typically are transition metals: iron, cobalt, and nickel. The catalyst-substrate interaction is also important, as a strong interaction could reduce catalytic behavior, though some interaction is necessary to prevent catalyst sintering and agglomeration. In many cases, a thin "support" oxide layer such as alumina or silica is deposited to improve the catalyst-substrate interaction. The catalyst is usually sputtered onto the support layer, then breaks up into discrete nanoparticles at high temperature. Figure 1-9 explains the mechanism of CNT growth. Finally, the growth temperature must be high enough to allow for the decomposition of the carbon source without being so high that the formation of polymeric carbon chains predominates that of graphitic carbon. MWNTs tend to grow at temperatures between 600°C-900°C, while SWNTs are often grown at higher temperatures, between 900°C-1200°C.

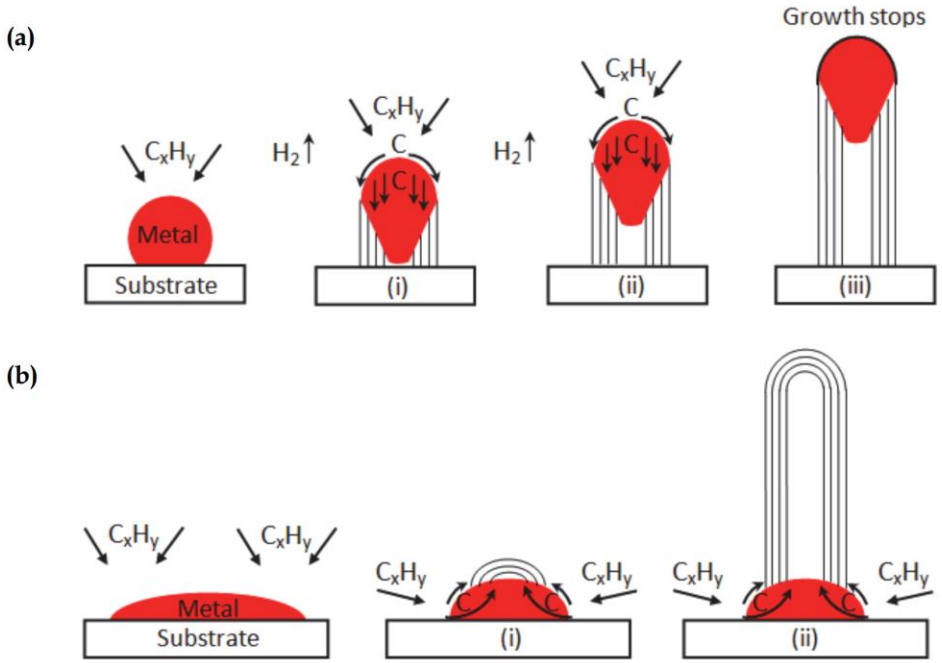

Figure 1-9. Two growth mechanisms of CNTs (a) tip-growth (b) base-growth. In both models, hydrocarbon gas diffuses to the catalyst and decomposes. Carbon dissolves into the metal catalyst particle and precipitates out in a crystalline cylindrical network having no dangling bonds and hence energetically stable [3].

Comparison with Other CNT Formats

Many other bulk assemblages of CNTs have been created, including entangled networks, films, randomly dispersed foams, yarns, flat tapes, forests, patterned pillars, bundles, nanofibers, and yarns. Most of these formats are grown in a similar way to forests then post-processed into other architectures. Figure 1-10 shows the relationship of CNT scale and order, and the progression of technology in the field. In the current state of research, forests and yarns receive the most attention for emerging applications, as there is now good understanding of the synthesis and processing techniques necessary to create them. Figure 1-11 shows the relationship of mechanical stiffness and the number of CNTs comprised in a structure. Notice the exponential drop-off in stiffness as CNTs are scaled into large domains.

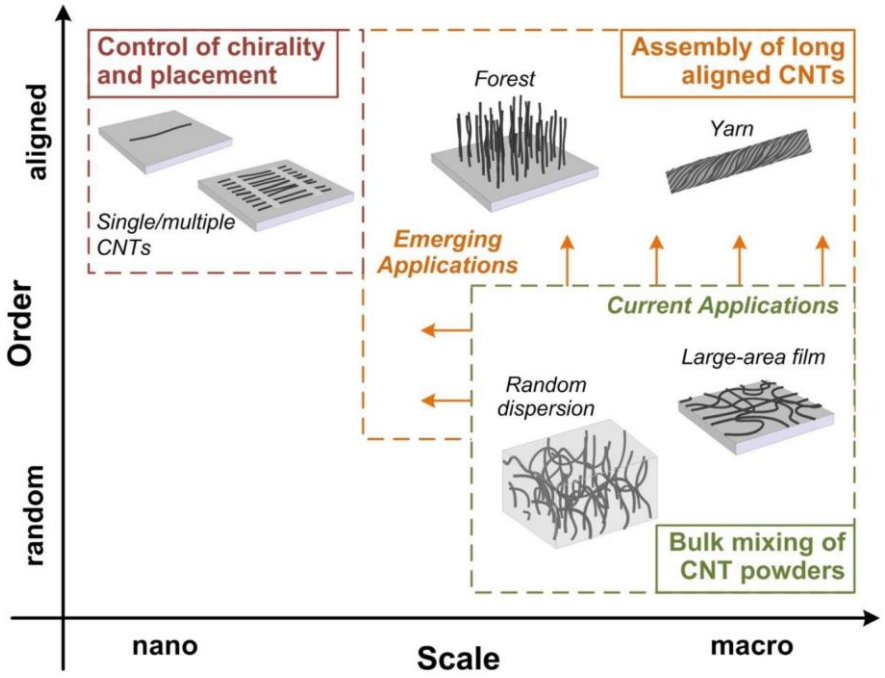

Figure 1-10. Emerging CNT applications rely on ordering of CNTs at hierarchical scales, moving from large-scale dispersions and films that are presently commercialized, to ordered macrostructures and nanoscale devices in the future. [4].

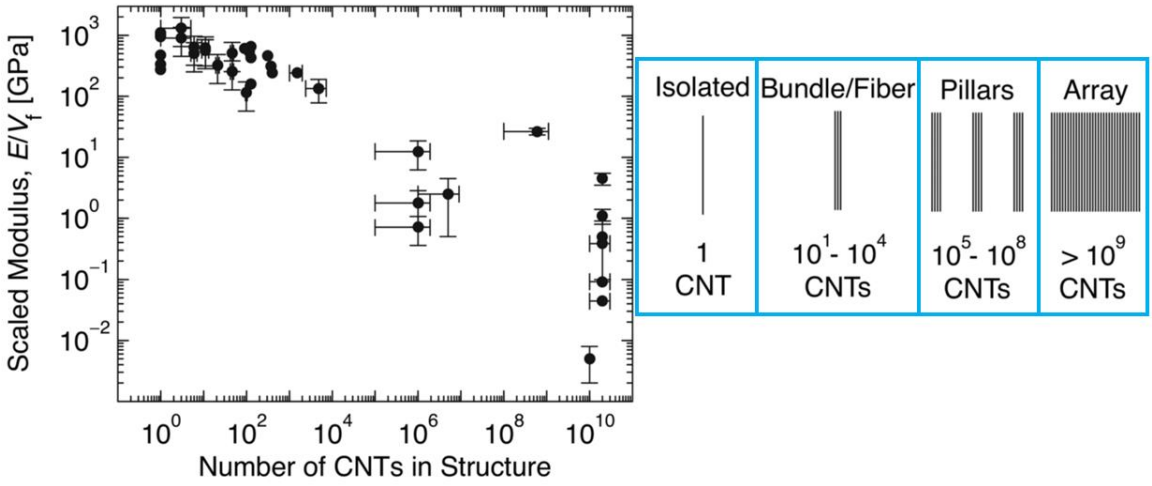

Figure 1-11. Stiffness of CNT systems as a function of their size. Elastic modulus (E) normalized by CNT volume fraction (V_f), scales with the number of CNTs enclosed in the structure. Isolated CNTs and CNT bundles/fibers exhibit $E/V_f > 100$ GPa, whereas larger scale CNT pillars and arrays exhibit $E/V_f < 1$ GPa. Adapted from [5].

Unique mechanical properties of CNT forests

CNT forests synthesis is highly scalable, enabling wafer-scale manufacturing and features approaching the meter-scale. CNT forest properties such as areal density, alignment, uniformity, and defect-density strongly depend on the synthesis process, so a precise understanding of the catalyst behavior and gas thermodynamics is crucial. In an ideal forest, constituent CNTs would be perfectly straight and defect free and their packing density (areal density) would approach 100%. Realistically, forests have relatively low areal density, stochastic and tortuous morphology, and mechanical anisotropy[29-31]. This unique structure-process-property relationship limits their use for typical micro-mechanical structure applications. The elastic modulus of CNT forests in axial compression typically ranges from 0.1 to 100 MPa[6, 21, 29, 32-41], orders of magnitude less than the elastic modulus of individual CNTs. This discrepancy is not surprising considering the preferred alignment of CNTs within a forest and that the typical areal density (CNT number density/average cross-sectional area of a CNT) of CNT forests ranges between 1-5% [42, 43], with 12% areal density[44] considered ultra-dense. Although the strength of individual CNT shells is extremely high, weak shear interactions between adjacent CNTs significantly reduce the effective strength. They can easily slip relative to another. These behaviors sum to unique mechanical properties exhibiting compressive behavior like an open cell foam. Chapter 5 investigates the mechanics of CNT forest in depth.

CHAPTER 2 - SYNTHESIS OF HIERARHICAL CNT FORESTS

Abstract

Carbon nanotubes (CNTs) are synthesized in vertically aligned "forests" by the floating catalyst chemical vapor deposition (FC-CVD) method. A novel synthesis process is presented here that allows the creation of electrically-addressable hierarchical CNT forests with tunable mechanical response. In this process, small-diameter branch-CNTs are synthesized directly from larger-diameter trunk-CNTs in a forest via an intermediate alumina coating that is applied to the trunk-CNTs using atomic layer deposition (ALD). The branch-CNTs (8 nm average) grow directly from the trunk-CNTs, partially filling the interstitial regions. The hierarchical forests exhibit a 5-10-fold increase in stiffness, and the two populations are electrically addressable despite the interfacial alumina layer between them. This work enables the design of complex CNT architectures with hierarchical features that bring tailored properties such as high specific surface area and robust mechanical properties that can benefit a range of applications.

Introduction

Nanostructured materials with tunable, multifunctional properties are desirable for many applications. Properties such as electrical and thermal conductivity, energy absorption, high specific surface area, and the ability to chemically functionalize are most often mutually exclusive. If a given material has exceptional properties in one area, other properties will be inferior. CNT forests are unique in that they have shown promise in all these areas and could theoretically be formed to retain exceptional properties across the board, simultaneously. Additionally, the ability to tune each property nearly independently has not yet been realized in other materials. This work takes inspiration from biology for a

novel hierarchical structure, much like well-ordered trees in a forest, as in Figure 2-1. Hierarchical structures naturally develop abundant surface area with minimal mass and supporting structure. They also have increased strength and conductivity between adjoining members due to the improved intersection and interconnection architecture. Thus, hierarchical structures provide a viable path towards tunable, multifunctional materials.

Figure 2-1. Human-designed forest, with well-ordered, hierarchical structure [1].

The significant free volume within CNT forests affords an opportunity for applying functionalized coatings that may enhance desired performance metrics. Additive processing of CNT forests through coating or grafting has advanced using several different methodologies. To enhance mechanical stiffness or functionality in device applications such as energy storage, CNT forests have been coated using atomic layer deposition (ALD) of alumina[45-47]. The gas phase ALD chemical precursors penetrate and deposit deep within CNT forests. The ALD films add a rigid coating to the outer surface of CNTs and encapsulate and strengthen the CNT-CNT contact points. In another additive processing

technique[48], thin graphene petals were directly synthesized from CNT forests using microwave plasma-enhanced CVD. The graphene petals are covalently bonded to the CNTs, leading to enhanced thermal transport and increased mechanical stiffness. However, coverage of graphene petals diminishes within the length of a CNT forest, with most petals occupying regions near the CNT forest's free surface.

In the traditional CNT forest growth procedure, the catalyst layer remains either at the bottom or top of the growing CNTs, and growth from the same catalyst can be achieved in successive steps by interrupting or pulsing hydrocarbon gas delivery with time. Each cessation of gas flow terminates the synthesis of one CNT forest layer, and reestablishing the gas flow nucleates a new CNT forest layer below the previous. This sequential CVD process has produced hundreds of vertically stacked CNT forest layers for both fixed catalyst and floating catalyst CVD methods[49]. The physical interfaces between successive layers, however, may lead to poor adhesion between layers. In addition, CNTs have been synthesized in the form of a concentric sheath around host CNTs or as short protrusions from host CNTs by a two-step synthesis requiring an intermediate solution-based processing step[50].

This work[51] reports the first successful growth of small CNTs directly from larger CNTs in a hierarchical structure. Extending the analogy of the CNT forest and tree, trunk-CNTs will serve as the host substrate for smaller-diameter branch-CNTs. The general outline of the synthesis process is depicted in Figure 2-2. First, trunk-CNTs are synthesized on a thermally oxidized silicon wafer with the floating catalyst chemical vapor deposition (FC-CVD) method[41]. Next, alumina is deposited on trunk-CNTs using ALD, which minimally affects the original CNT forest morphology. Finally, in a second FC-CVD step,

branch-CNTs are synthesized, where gas phase ferrocene catalyst can penetrate deep within the forest and selectively attach on the deposited alumina. Physical analysis of the forests shows several unique characteristics and properties: branch-CNTs originate from the alumina deposited on the trunk-CNTs, the hierarchical structure increases the mechanical stiffness to the forest, the hierarchical CNT forest exhibits electrical connectivity despite the insulating alumina layer, and the synthesis process enables the simultaneous tuning of electrical, thermal, mechanical, and electrochemical properties.

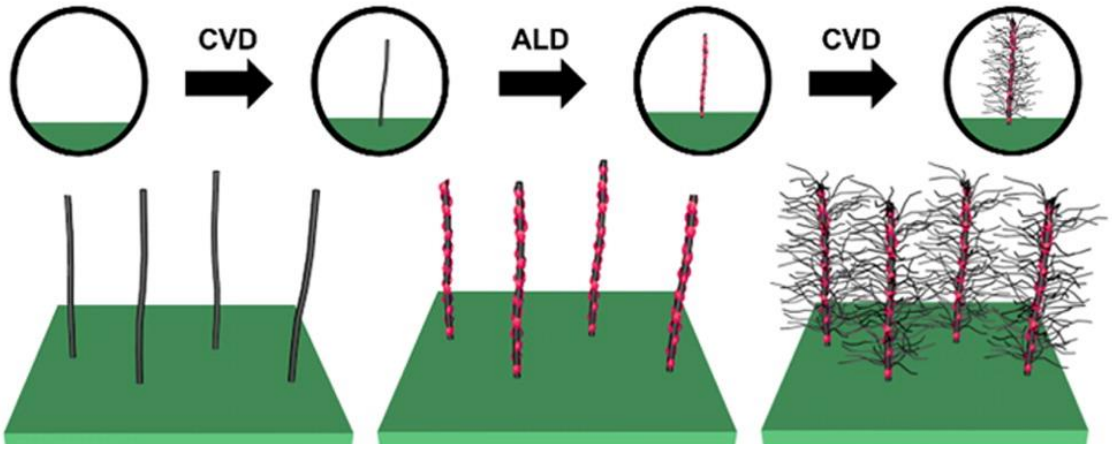

Figure 2-2. Scheme of the synthesis process used to generate hierarchical carbon nanotube forests. A CNT forest is grown on an oxidized substrate and then subjected to atomic layer deposition of alumina. Then, branch CNTs are then synthesized from the intermediate alumina layer, producing a hierarchical CNT forest structure.

Methods

Trunk-CNT Synthesis with floating catalyst chemical vapor deposition (FC-CVD)

CNTs were synthesized using the floating catalyst chemical vapor deposition (FC-CVD) method[41]. A 10 wt % solution of ferrocene in xylenes was injected into a 25 mm diameter tube furnace held at 750 °C. Process gases of Ar and H_2, introduced at 500 and 50 sccm, flowed throughout the entire synthesis. To initiate CNT synthesis, the solution was injected into the furnace by a programmable syringe pump at a rate of 1.0 mL/h. The

substrate was a 1 cm^2 undoped silicon wafer with ~500 nm thermal oxide layer. The trunk-CNTs were grown for 3600 sec.

Atomic layer deposition of alumina as a low-density catalyst support

ALD was used to deposit alumina within the trunk-CNT forest. The precursor gases of water vapor and trimethylaluminum (TMA) were each introduced for 100 cycles at a processing temperature of 200 °C. The gaseous ALD precursors penetrate and deposit deep into the trunk-CNT forest rather than depositing on only the exterior forest surfaces. ALD alumina is known to promote the synthesis of small diameter CNTs by stabilizing catalyst particles from Ostwald ripening and catalyst deactivation[52]. Utilizing these conditions, the nominal rate of alumina deposition is ~1.2 Å/cycle, leading to a coating ~12 nm thick for an ideal process. However, the low seeding density of the ALD chemistry on the CNT surfaces led to sparse formation of nanoparticles and continuous seeding that yields a low density of alumina particles coated on the CNTs with diameters less than 12 nm, as seen in Figure 2-4.

Branch-CNT Synthesis with FC-CVD

The alumina-coated CNTs were then subjected to a second round of FC-CVD CNT synthesis using identical conditions to those used to create the trunk-CNT forest for 30 min. Both FC-CVD and ALD systems are seen in Figure 2-3.

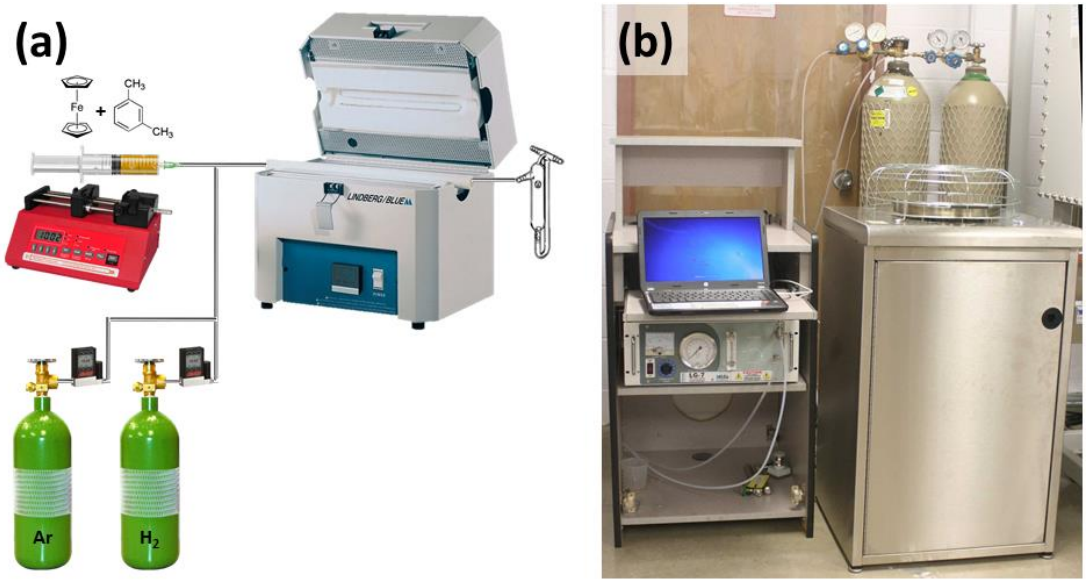

Figure 2-3. Equipment needed to grow hierarchical CNT forests. (a) floating-catalyst chemical vapor deposition system comprised of a tube furnace, gas cylinders for precursor and carrier gases, syringe pump, and a solution of hydrocarbon liquid and catalyst particle (b) atomic layer deposition system.

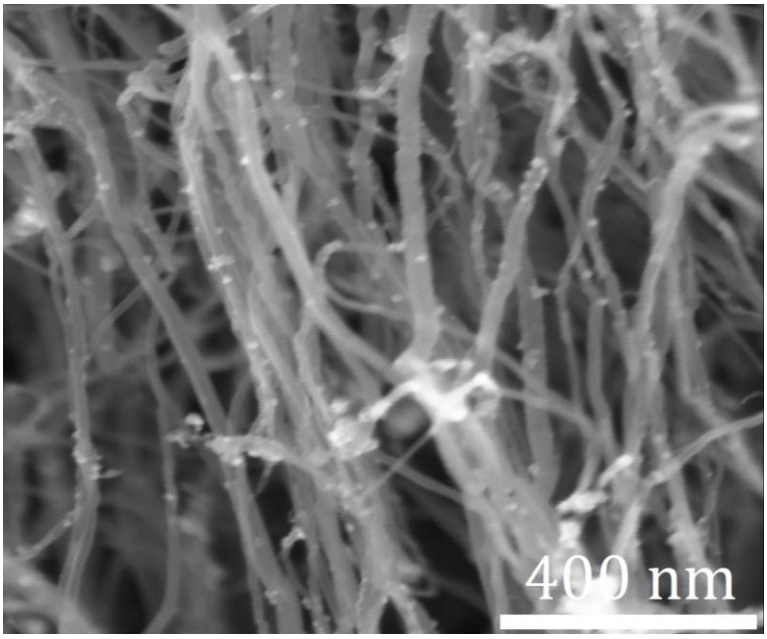

Figure 2-4. SEM image of a CNT forest after 100 ALD alumina cycles shows that the CNT sidewalls are decorated with alumina nanoparticles.

Materials Characterization: Raman, SEM, TEM, nanoindentation

Raman spectroscopy of the samples was conducted using a Renishaw inVia Raman microscope at an excitation wavelength of 632 nm. Samples were imaged using a FEI Tecnai F30 Twin high resolution TEM and an FEI Quanta 600 FEG SEM. The CNT forest mechanical stiffness was examined using nanoindentation using an Agilent G200 nanoindenter and a 100 μm diameter diamond flat punch indenter tip. Each CNT forest sample was examined in nine locations, with each test consisting of 10 sequential loading and unloading segments at exponentially increasing loads. The elastic stiffness of the material was obtained from the unloading curve slope of each unloading segment.

Electrochemical Analysis

For electrochemical analysis, two sets of samples were prepared: substrates with only trunk-CNT forests and substrates with trunk & branch-CNT forests. Both sets of substrates were cleaved into two identical electrodes having the same footprint area (~0.5 cm^2). These samples were then vacuum infiltrated with 1-ethyl-3-methylimidazolium tetrafluoroborate (EMIBF4) (>98%, Aldrich) as the electrolyte for electrochemical measurements and placed together with a Celgard separator into a symmetric two-electrode configuration. Electrochemical impedance spectroscopy (EIS) was performed using a Metrohm Autolab Multichannel Testing system in the frequency range of 0.01-1 MHz with zero DC bias and amplitude of 5 mV RMS. Equivalent circuit analysis was performed using the Metrohm Autolab software package.

Results & Discussion

The first-step synthesis of trunk-CNTs produced a forest with relatively large diameters (~25-60 nm). For the synthesis times used in this study, CNT forests were 150-

200 μm tall on the substrate. The ALD of alumina on the trunk-CNTs is heterogeneous in nature, often decorating the side walls of the trunk-CNTs as sub-12 nm diameter particles. This is possible due to the energetically unfavorable surface of CNTs, having high curvature. The alumina deposition minimally disrupts the native CNT forest morphology. Cleaving the samples for imaging disrupts the native alignment of the CNTs; however, it enabled confirmation that alumina and branch-CNTs successfully penetrated fully the sample volume.

Inspection of the CNT forest after the branch-CNT growth reveals clusters of small diameter CNTs surrounding the trunk-CNTs, as seen in Figure 2-5. The alumina particles observed after ALD deposition present as relatively bright particles decorating the side walls of the trunk-CNTs. The branch-CNTs wrap around the trunk-CNTs within the forest, filling what was previously free space between the trunk-CNTs. The linear nucleation density of branch-CNTs is estimated to be one CNT per 100 nm length of trunk-CNTs based on SEM images. Additionally, no CNT growth was observed from the substrate below the trunk-CNT forest, as has been typically observed for sequential CNT forest growth. Such hierarchical growth of small diameter CNTs from a host CNT forest has not been previously reported.

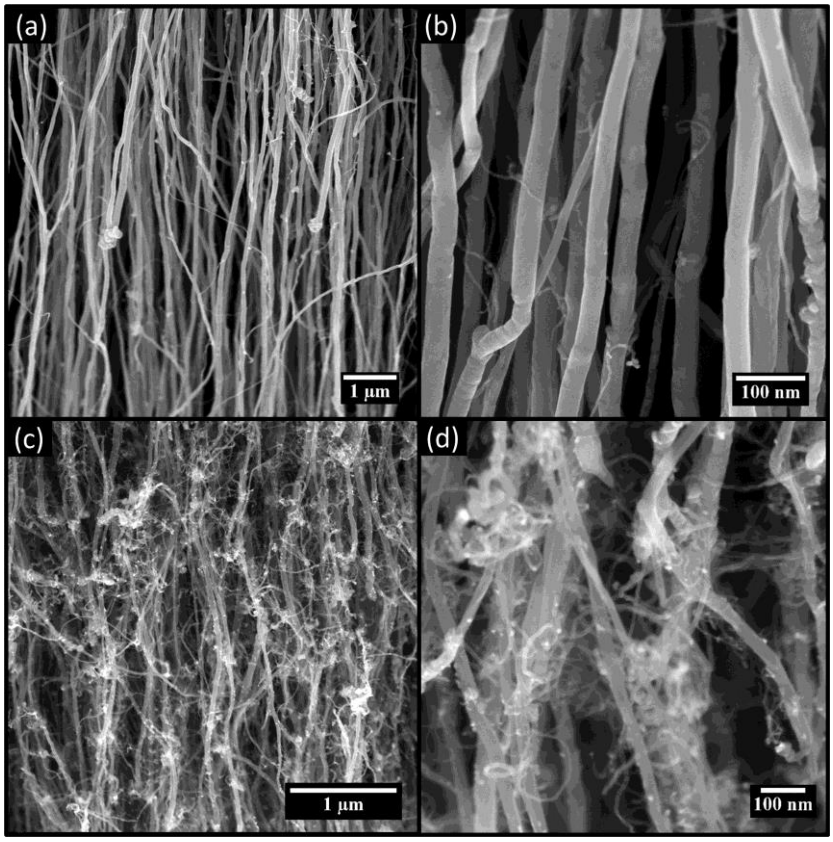

Figure 2-5. SEM micrographs show a CNT forest before (a, b) and after the synthesis of smaller, branch-CNTs (c, d). All images were obtained by first cleaving the sample substrate then imaging the exposed internal CNT forest morphology.

To ensure that the hierarchical growth was a direct result of the alumina layer, the synthesis methodology was repeated without the ALD alumina deposition step. These syntheses produced a different architecture, with vertically stacked CNT layers, and lacking intermediate branch-CNTs. This layered architecture is consistent with previous reports[53], as seen in Figure 2-6.

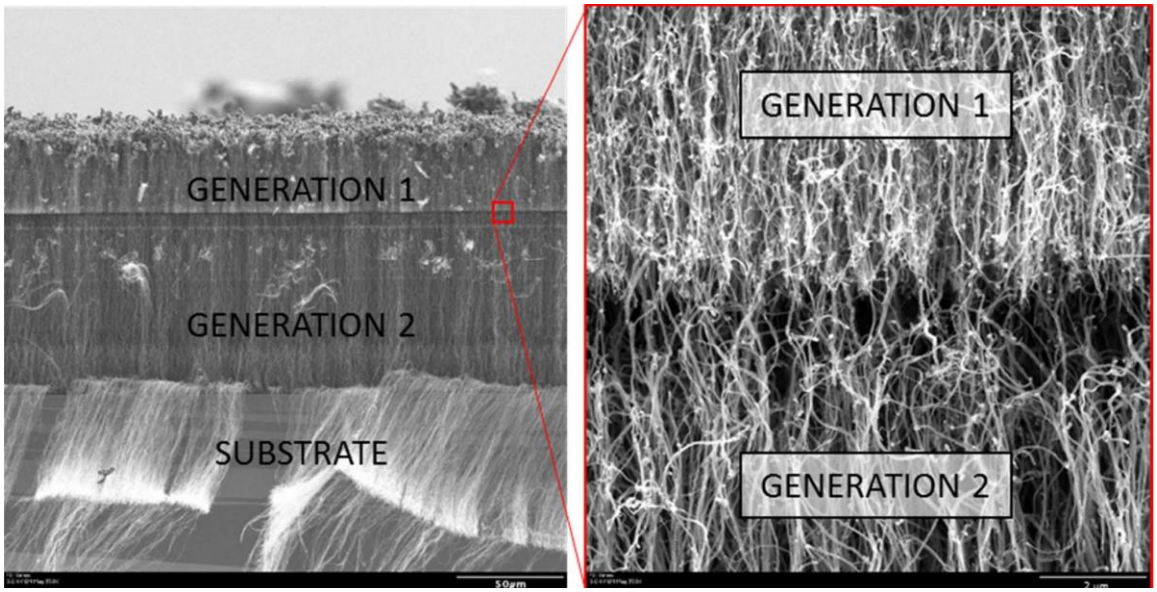

Figure 2-6. Multiple-step CNT synthesis without an intermediate alumina layer produced forest layers, with a discernable gap between layers. Scale bar is 50 µm in (a) and 2 µm in (b).

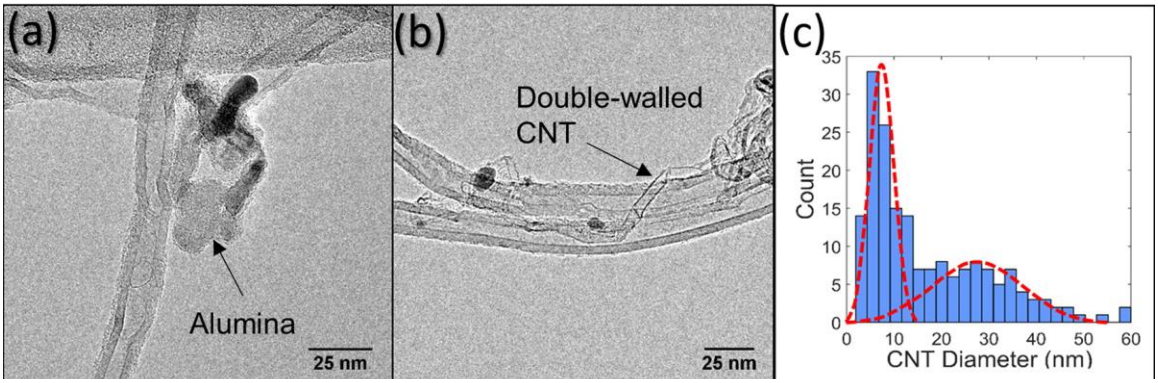

Figure 2-7. TEM micrographs of the CNT forest after branch-CNT synthesis. (a) Nucleation of branch-CNTs observed originating from the surface of an alumina particle. (b) Double-walled CNTs were observed after the branch-CNT growth step. (c) Distribution of diameters is bimodal, with peaks near 8 and 28 nm for trunk and branch-CNTs, respectively.

The mass of samples was tracked throughout the processing steps for three samples. A typical oxidized silicon substrate with approximately 1 cm^2 area had an average mass of approximately 132 mg. The first FC-CVD step of trunk-CNTs has an average mass of 1.5 mg, the alumina deposition adds negligible mass, and the second FC-CVD step of branch-CNT also adds an average mass of 1.5 mg.

TEM samples were prepared by gently sonicating a liberated section of a CNT forest in ethanol before dispersing the solution on a lacy carbon TEM grid. Two distinct populations of CNTs were observed during TEM analysis, consisting of large diameter CNTs (25-60 nm) and smaller diameters (2- 15 nm), as shown in Figure 2-7. The quantity of smaller diameter CNTs is significantly larger than that of larger diameter CNTs. A histogram of the outer diameter of 185 CNTs from five TEM micrographs is shown in Figure 2-7. Diameter measurements were obtained using ImageJ analytical software[54]. The resulting distribution in strongly bimodal in nature. Average diameters are 8 nm for the trunk-CNTs and 28 nm for branch-CNTs, obtained by fitting the data with two normal distributions.

Alumina deposition on the trunk-CNTs was heterogeneous in morphology. Discrete nodes of alumina are readily observed on the outer surface of trunk-CNTs in Figure 2-7a, while a relatively conformal coating may be seen in Figure 2-7b. Dark iron particles resided inside of both the small and large diameter CNTs, as is typical when using the FC-CVD method. In addition, iron particles resided on the exterior surface of the larger CNTs. Some larger iron particles were coated in a carbonaceous shell and did not support CNT growth. Smaller iron particles, however, frequently supported growth of small diameter CNTs. The nucleation sites of two smaller diameter CNTs from an alumina nanoparticle observed by TEM is highlighted in Figure 2-7a. Few-walled CNTs were also observed after branch-CNT synthesis (see Figure 2-7b).

Raman spectra of the CNT samples were obtained after both trunk and branch-CNT syntheses, with results plotted in Figure 2-8. The ratio of the peak intensity related to disordered carbon, located near 1340 cm^{-1}, relative to the peak intensity for graphitized

carbon, located near 1580 cm^{-1}, is used to estimate CNT quality. A lower value is desirable, as it represents a relatively low quantity of disordered carbon relative to well graphitized CNTs. The I_D/I_G ratios before and after branch-CNT growth were similar (0.68 and 0.63, respectively); however, radial breathing mode (RBM) signatures emerge at approximately 130 and 192 cm^{-1} after branch-CNT growth, representative of single-walled or double-walled CNTs. These peaks are associated with single-walled CNTs with diameter 1.91 and 1.29 nm, respectively, according to the relationship[55] $\omega_{RBM} = 248/d$ (nm), where ω_{RBM} represents the frequency of RBM peak and d represents the diameter of the CNT. While it is not clear if the observed RBM peaks represent single- or few-walled CNTs, they nevertheless demonstrate the presence of few-walled CNTs not present after the trunk-CNT synthesis, consistent with TEM findings.

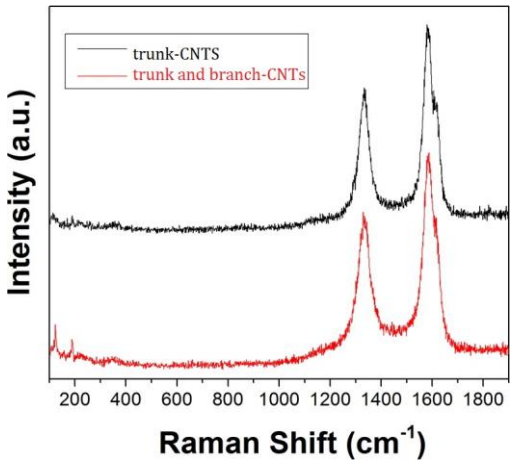

Figure 2-8. Raman spectra of CNT forest after trunk-CNT and branch-CNT syntheses. The intensities of the G- and D-peaks are similar between the syntheses. However, the RBM peak is present after branch-CNT growth, suggesting the presence of desirable few-walled CNTs.

The alumina coating and growth of branch-CNTs are expected to increase the relative stiffness of the forest relative to the trunk-only CNT forest. A concentric alumina coating acts to increase the bending and axial stiffness of each CNT, while alumina

particles affixed to CNT-CNT bonding points would increase rigidity of the contacts. To examine mechanical behavior, CNT forests were indented using a 100 µm diamond flat punch. A total of nine locations were examined for each sample. Samples were examined after initial CNT synthesis, after ALD deposition, and after branch-CNT synthesis. Each nanoindentation test consisted of 10 incremental loading and unloading cycles to examine stiffness as a function of depth. The slopes of the unloading curves are used to represent the elastic stiffness of the CNT forest. The maximum load applied to samples was 100 mN.

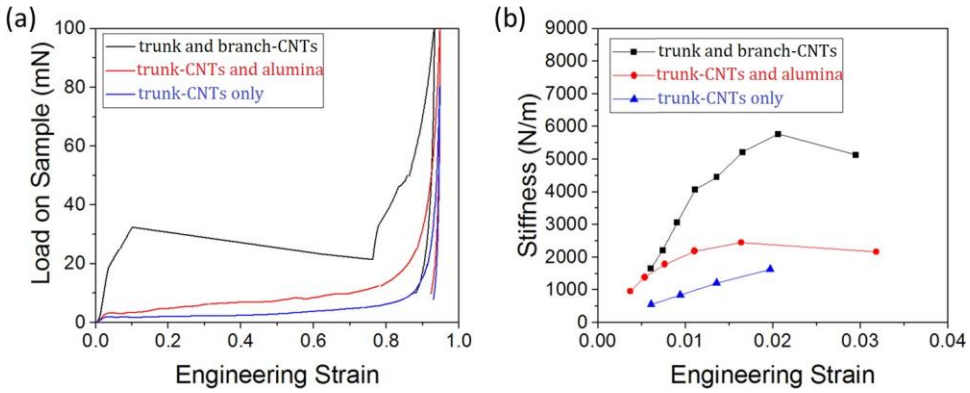

Figure 2-9. Mechanical performance of CNT forests grown on oxidized silicon substrates. (a) Indentation load as a function of engineering strain for as-grown trunk-CNT forests, alumina-coated CNT forest, and after synthesis of a branch-CNTs (b) Elastic (unloading) stiffness of the CNT forests further demonstrates the enhanced stiffness provided by the alumina coating and branch-CNT forest relative to the as-grown trunk-CNT forest.

Figure 2-9a shows the load-displacement characteristics of a trunk-CNT forest, an alumina-coated forest, and a hierarchical forest. Initial loading produces a linear-elastic response, followed by an elongated plateau region and a rapid increase in slope during cellular densification. For CNT forests, the onset of the nearly horizontal plateau region is initiated by coordinated CNT buckling. As previously observed, the stiffness of an alumina-coated CNT forest increases due to the increased bending stiffness of constituent CNTs and increased rigidity of CNT-CNT bonds. For the relatively large diameter trunk-

CNT forests tested here, the increased stiffness due to alumina coating was approximately 100% relative to uncoated CNT forests. Branch-CNTs provide mechanical reinforcement by filling the interstitial regions between adjacent large diameter trunk-CNTs.

The compressive load required to deflect the hierarchical CNT sample approaches a factor of 10 greater than the trunk-only CNT forest. The multiple unloading segments of the indentation curves are removed in the figure for clarity. The trunk-CNT forest and alumina coated CNT forest buckle at approximately 10 μm displacement (5% engineering strain), as denoted by the initiation of the elongated plateau region. The presence of the branch-CNTs in the hierarchical CNT forest, however, delayed buckling until approximately 20 μm displacement (10% engineering strain). Further, the hierarchical CNT forest induces a rapid buckling and collapse with a negative effective stiffness, while the trunk-CNTs and alumina-coated CNTs show a slightly positive plateau slope. The elastic stiffness obtained from unloading, shown in Figure 2-9b, similarly shows that the alumina coating and branch-CNT forest growth increase rigidity. The alumina coating increases elastic stiffness by a factor of ~2 relative to the uncoated trunk-CNT forest, while the branch-CNT forest increased the elastic stiffness by a factor of 5.

Electrical connectivity between the trunk and branch-CNTs is critical for applications of the hierarchical CNTs, such as energy conversion and storage. To form the hierarchical forest, a thin alumina layer bridging the trunk and branch-CNTs is necessary, even though it is not evident that such an interface would sustain electrical connectivity between the different CNT populations. To explore this concept, trunk and branch-CNT forests were subjected to cyclical voltammetry (CV) and electrochemical impedance spectroscopy (EIS) in ionic liquid electrolytes to assess electrical transport properties

across key interfaces (Figure 2-10). The CV scans shown in Figure 2-10a (taken at 100 mV/s) show that the hierarchical forest leads to an increased current density and indicates a greater accessible surface area in this material. Whereas an increased current density can also be correlated with pseudo-capacitance, the negligible mass of alumina and the extensive studies focused on using alumina as an inert passivation material for electrochemical energy storage elucidates this effect to be correlated to increased surface area from the branch-CNTs[56]. Notably, this qualitatively indicates that the branch-CNTs are electrically addressable since their signature is evident in CV curves. If the alumina barrier between the trunk and branch-CNTs was insulating in nature, the increased current density would not be observed.

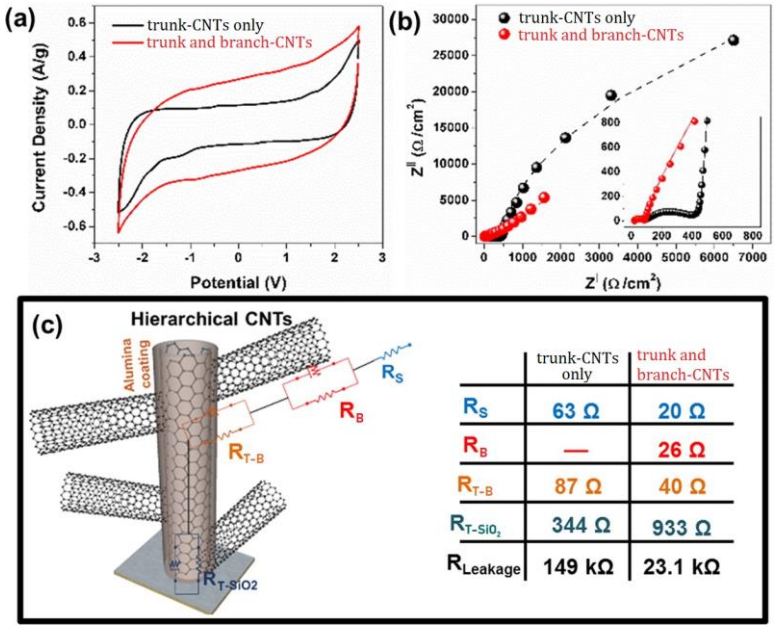

Figure 2-10. Electrochemical behavior of CNT forests. (a) Cyclic voltammograms show that hierarchical CNT forests exhibit greater current density than trunk-only forests. (b) Electrochemical impedance spectroscopy provides quantitative estimation of electrical resistance components within a trunk and branch-CNT forest, with values tabulated in (c). In the table, the subscript S refers to solution, B refers to branch-CNTs, T refers to the trunk-CNTs, and SiO_2 represents the oxidized silicon substrate. A circuit representation of $R_{Leakage}$ is not included in (c) since this represents the low-frequency desorption (or self-discharge) of ions from sites at exposed carbon surfaces and therefore cannot simply be represented schematically.

To quantitatively deduce electrical addressability in the hierarchical CNT material, frequency-dependent EIS was compared between the trunk-only forest and trunk and branch forests. By fitting the response to an equivalent circuit model, key resistances in the CNT forests, including the resistance across the trunk and branch connection were analyzed. The most accurate fits to the EIS spectral response reflect an additional time constant in the frequency response of the hierarchical CNT forest that is not present in the trunk-only CNT forest. The resistances associated with each time constant and their meaning are tabulated in Figure 2-10c, along with a schematic illustration generally highlighting the meaning of each resistance component. In brief, R_S is the solution or series resistance of the material, R_B is the charge transfer resistance at the branch-CNT/electrolyte interface, R_T/SiO_2 is the interfacial resistance across the trunk-CNT/SiO_2 interface, $R_{Leakage}$ is the leakage resistance of the device, and R_{T-B} is the resistance across the trunk-CNT/branch-CNTs interface. A value of R_{T-B} is listed in Figure 2-10(c) for the trunk-only forests corresponds to the charge transfer resistance at the trunk-CNT/electrolyte interface in the absence of branch-CNTs. Compared to the resistance measured across the trunk-CNT/SiO_2 interface which is above 300 Ω in both cases, the relative interfacial resistance between the trunk-CNTS and branch-CNTs is fit to be 40 Ω. Additionally, the series resistance (R_S) is lowered for the hierarchical CNTs due to the greater overall CNT-electrolyte interface area that is expected in the hierarchical CNT forests. Overall, these results give quantitative support that the hierarchical structure is fully electrically addressable. This builds from a relative comparison between the interfacial resistance at the trunk-CNT/branch-CNT interface (40 Ω) and other interfaces in conductive portions of the hierarchical CNT material such as R_B (26 Ω) and R_S (20 Ω). This opens this material

system to a range of potential applications such as energy storage, energy conversion, sensing, and catalytic processes, where the engineered hierarchical substructure that is demonstrated for the first time in this study can enable or improve the function of the CNT-based material in performance.

Application Example

These hierarchical CNT forests were recently used in an application of lithium-sulfur battery cathodes. The research showed successful use of the material as a high specific surface area cathode that accommodates sulfur-carbon chemistry. Structurally-designed hierarchical carbon nanotube (CNT) arrays were combined with site-selective vapor phase sulfur infiltration to produce thick electrodes with controlled sulfur loading and high areal performance. The results illustrate the critical role structural hierarchy plays in sustaining electrical connectivity to enable high utilization of the sulfur embedded in thick electrodes with high gravimetric loading. Here, a primary large-diameter CNT population provides robust conductive trunks that branch into a secondary small-diameter and high-surface-area CNT population capable of giving rapid electrical access to coated sulfur. Site-selective vapor phase sulfur infiltration, based on the capillary effect, controllably targets loading of one or both CNT populations to facilitate gravimetric loading from 60 wt% to 70 wt% sulfur. Cathode performance is excellent, with high areal loading of 6 mg/cm^2, specific charge of 1.092 Ah/g_S (6.5 mAh/cm^2), and excellent rate performance with >60% capacity retained at 10 times the discharge rate. Overall, this work leverages site control of sulfur incorporation into a host cathode enabled by controlled CNT growth techniques to emphasize the important principle of “quality over quantity” in

designing high areal loading strategies with high areal performance and good sulfur utilization.

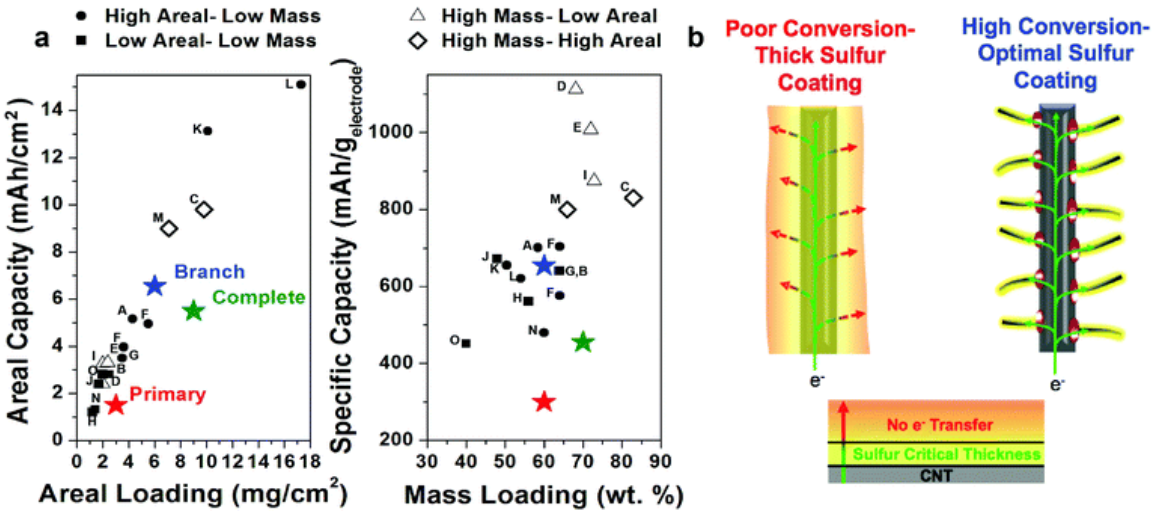

Figure 2-11. (a) Comparison of this cathode to other composite sulfur cathodes, emphasizing the importance of structural cathode design and high sulfur utilization in thick electrodes. The branched cathode was among the best performing solid cathodes, has high sulfur utilization, and has controlled site-selective sulfur infiltration. (b) Schematic explanation of the advantage of the hierarchical CNTs in developing effective thick sulfur electrodes, especially with an ability to selectively infiltrate the small second generation CNTs.

Conclusions

Hierarchical CNT forests were synthesized by nucleating branch-CNTs from the external surface of trunk-CNTs in a forest architecture. To enable this growth, a thin coating of alumina is deposited via ALD on the trunk-CNTs and then iron catalyst is delivered deep within the forest via floating catalyst CVD. The branch-CNTs have a smaller diameter than the trunk-CNTs and can effectively fill the interstitial regions between trunk-CNTs in the forest. The hierarchical CNT materials exhibit an increase in mechanical stiffness by a factor of 5-10 relative to the trunk-CNT forest alone, emphasizing the capability to tune the mechanical properties of CNT forests. Further, electrochemical analysis quantitatively demonstrates the electrical connectivity between trunk and branch-

CNTs that is critical for applications. This work opens a higher order approach to engineer the structure-function relationships of CNT forests that can bridge their application into numerous areas such as energy storage, energy conversion, structural materials, sensing, water purification, and more.

CHAPTER 3

CHAPTER 3 - ELECTRON-BEAM ACTIVATION OF SAPPHIRE FOR CNT PATTERNING

Abstract

Integration of CNTs into functional devices often involves the use of time-consuming and laborious patterning techniques to obtain spatially selective growth, such as in photolithography with masks, resists, and stenciling. A single-step process is presented here to pattern substrates for subsequent CNT forest growth. The novel selective site activation process uses a raster-controlled electron-beam in the presence of water vapor to activate a catalyst support substrate at select locations. In the electron beam (e-beam) rastered areas, the stoichiometry, surface roughness, and coating of the catalyst-support material is modified via radiolysis-driven chemical mechanisms. These areas have preferential catalyst adhesion interactions that allow subsequent CNT growth to only occur in these areas. This technique holds great promise in producing high fidelity patterned CNT forests because of its simplicity and effectiveness.

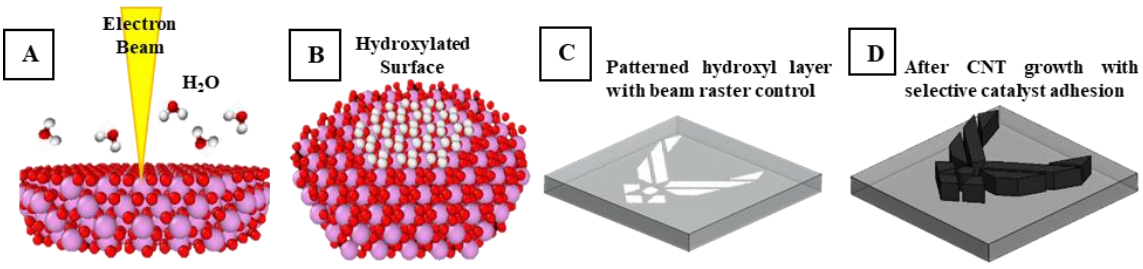

Figure 3-1. Process of creating patterned CNT forest on sapphire (A) cleaned sapphire surface is rastered by ESEM (B) hydroxyls are created and deposited on the surface (C) electron beam rastering and parameter-control allow for patterning at various conditions (D) selective CNT growth resulting from increase catalyst adhesion in activated areas.

Introduction

CNTs are ideal candidates for many applications including electronic devices, molecular sensors, energy storage, structural components, and more[4, 57-60]. Their integration into functional devices requires pathways for spatially selective catalyst deposition and patterned growth of CNT arrays. Common approaches used for selective catalyst deposition include the use of photo- and electron-beam lithography, dip-pen nanolithography, solution-based printing, and template-assisted deposition[61-73]. In the most widely used methods of photo- and e-beam lithography, selective catalyst deposition requires many steps including masking, polymer resist deposition, patterning, and lift-off. On the other hand, dip-pen nanolithography[74] provides a direct high-throughput writing technique without the need for resists but is driven by liquid-solid interactions. Likewise, feature resolution achievable using printing techniques is limited by the extrusion method, ink rheology and ink-substrate interactions. Recently, a single-step, catalyst-deactivation process was used to hinder CNT forest growth in select locations and generate patterns using a copper stencil[71]. This resist-free technique, however, lacks control over pattern fidelity and resolution. **Hence, single-step, mask-less, and resist-free patterning remains an attractive concept for spatially selective growth of CNT forests**.

In addition to challenges involved with integration of spatially selective CNT growth, other fundamental aspects of CNT growth such as catalytic efficiency and growth yield can also hinder maturation of CNT-based technology. The surface basicity and microstructured roughness of the catalyst support is known to influence the catalyst/support interactions and, thus, CNT growth yield[75-78]. An inactive growth surface such as that of α-alumina (0001), commonly known as c-cut sapphire, can be modified to yield an active

CNT growth support. Ion bombardment of a masked substrate activates the substrate for catalyst adhesion exclusively at the irradiated locations. The general mechanism of the activation in these processes is:

- irradiation increases the surface roughness and changes surface stoichiometry
- surface roughness and non-stoichiometric conditions increase the surface energy
- high surface energy prevents catalyst particle agglomeration and Ostwald ripening
- small particles with high areal density improve growth efficiency

Ion bombardment has also been used to engineer reconstructed alumina and achieve spatially- and chiral-selective growth[79], suggesting that energetic particles can be used to finely tune catalyst/support interactions and attain control over growth.

This work[80] reports a novel water-assisted, e-beam induced activation process that can be used to obtain patterned CNT forest growth without the need for masks, resists, or stencils. E-beam irradiation in combination with water vapor inside an environmental scanning electron microscope (ESEM) can be used to locally activate the surface of c-cut sapphire to make it a suitable support for CNT forest growth. This activation process provides excellent pattern fidelity and feature resolution, as well as tunability of surface chemistry and roughness without modifying the surface profile dramatically or requiring multi-step processing. The process uses established software and hardware for e-beam lithography, is easy to use, provides a wide range of activation conditions, and is accessible to a typical ESEM equipped with variable pressure, thus providing an alternative to e-beam lithography for selective catalyst deposition. Beyond patterned CNT growth, the proposed technique provides a pathway for direct control of catalyst/support interactions with desired

spatial and chemical selectivity only limited by the e-beam probe size and radiolysis-driven interactions.

Methods

Activation of catalyst supports using the e-beam chemistry process

Sapphire wafers (University Wafer, Inc.) were cut to approximately 0.5 cm × 0.5 cm square pieces and cleaned thoroughly before patterning and activation. The substrate specifications are as follows: 99.99% crystal purity, <10 Å surface roughness, 0.5° miscut angle, and <2 μm/cm surface flatness. The c-cut sapphire samples were cleaned by first sonicating them in acetone for approximately 5 mins and then rinsing them with isopropanol. The samples were then dried with a high velocity filtered nitrogen flow (0.2 μm filter size) and baked at 500 °C in air for 20 min using a hot plate. The cleaned samples were immediately introduced into the vacuum chamber of the ESEM to avoid surface contamination and to minimize adsorption of water. Support activation was achieved by introducing deionized water vapor into the vacuum chamber of the ESEM (FEI Quanta 650 EF SEM) and subsequently scanning the e-beam at select locations in low vacuum mode (<1 Torr water vapor). SEM parameters such as beam current, dwell time, accelerating voltage, and pixel spacing were controlled while parameters such as working distance and water vapor pressure were kept fixed (10 mm and 0.08–0.1 Torr, respectively). The accelerating voltage was limited to ≥ 5 kV to avoid misalignment of the electron optics and subsequent loss of feature resolution. The pixel spacing, which was determined by both the scan resolution and horizontal field width, was kept between 8 nm and 128 nm. The Air Force logo was patterned using the Nanometer Pattern Generation

System (NPGS) using 10 kV accelerating voltage, 2 ms dwell time, 16 nm pixel spacing, and 0.08 Torr water vapor pressure[81, 82].

CNT Forest growth

CNTs were synthesized via floating-catalyst chemical vapor deposition (FC-CVD) as described in Chapter 2. CNT growth was then examined via SEM and Raman spectroscopy using an FEI SEM (Quanta 650F) and Renishaw Raman Spectrometer (633 cm−1 laser wavelength and ∼120 μW laser power. Catalyst evolution studies (i.e. Ostwald ripening and coarsening) were used to understand how the e-beam chemistry process changes the catalyst-support interaction and catalyst particle size. Catalyst film is deposited on the patterned areas and exposed to annealing conditions equivalent to growth in the absence of a hydrocarbon source. The e-beam deposited iron catalyst film (∼0.3 nm) was annealed in hydrogen (200sccm) at atmospheric pressure and at a temperature of 585 °C to promote catalyst reduction, dewetting, and particle formation. After 10 min, the samples were rapidly cooled with a continuous flow of hydrogen before exposure to air and catalyst evolution studies.

Catalyst evolution studies

Atomic force microscopy (AFM) was used to study size and number distributions of catalyst particles formed on the activated regions and compared against particles formed on an as-cleaned surface. AFM studies used a Veeco AFM (Nanoscope Multimode) equipped with a low noise scanner and MikroMasch probes (HQ:NSC15/Al-BS, 8 nm nominal tip radius, 265–410 kHz resonant frequency, and 20–80 N/m force constant).

Surface characterization

The surface properties of as-cleaned and activated sapphire were studied using both AFM and X-ray photoelectron spectroscopy (XPS). AFM was used to measure surface roughness of as-cleaned and activated regions both before and after catalyst particle formation (prior to CNT growth). On the other hand, XPS was used to characterize the surface chemistry of the catalyst support of as-cleaned and activated regions only before catalyst particle formation and CNT growth. XPS studies were performed using a Kratos XPS (AXIS Ultra, ~10−8 Pa) equipped with an Al Kα X-ray source. A charge compensator (~1.5–2.5V) was used during spectral collection to neutralize charging and adjust the binding energy of the C 1s peak to 284.8 eV. XPS data analyses were done using the CasaXPS software package. Prior to analyzing composition and chemistry, all photoelectron peaks were processed using Shirley background subtraction. Survey spectra showed Al, O and C as the main components. The components in the O 1s region were extracted using a constrained fitting procedure with mixed Gaussian-Lorentzian peaks. During fitting, the full width at half maximum and position of the peaks were allowed to float but the relative change between the O-H and O-Al components was constrained. The spacing between the O-H and O-Al components was fixed to 1.3eV as reported in the literature[83]. Shifts resulting from residual charging (after charge compensation) were corrected during data analysis by assigning the O-Al component in the O 1s region to 531.1eV.

Results and Discussion

Patterned CNT forest growth

A novel electron-beam chemistry process was used to achieve control over catalytic activity with excellent spatial selectivity, determined electron optics and irradiation conditions[80]. Figure 3-2 demonstrates results for a sample subjected to e-beam chemistry and CNT growth conditions. An increase in growth efficiency was observed exclusively in the regions where the pattern was drawn using the e-beam in water vapor despite exposing the entire support to the floating catalyst during growth. Selective growth of CNT forests exclusively in the activated regions demonstrates the high spatial selectivity and excellent pattern fidelity. A small amount of random CNT growth was obtained outside the patterned areas possibly for two reasons: the precipitation of CNTs onto the support via gas-phase decomposition and growth of CNTs, or the sparse growth of CNTs where surface energy is high, such as surface defects, crystal steps, and contaminant sites. Tall forests grew only in the patterned regions without further processing. Providing the appropriate catalyst/support interaction increases the catalytic activity and growth efficiency.

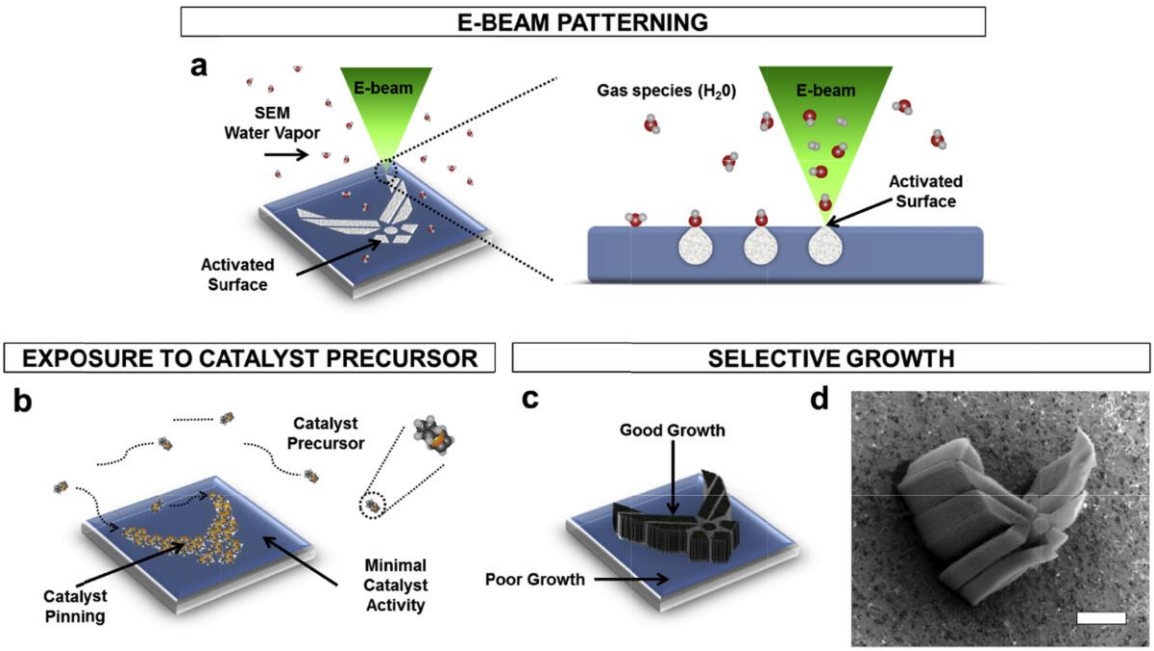

Figure 3-2. Demonstration of patterned CNT growth using the novel e-beam chemistry process. (a–b) Schematic representation of surface activation and growth. (c) Preferential precursor interaction at the activated regions leads to higher catalytic activity. (d) SEM micrographs of a high-fidelity pattern of the U.S. Air Force logo. Scale bar is 10 μm.

Optimizing activation conditions

A parametric study to optimize activation conditions was also completed. An array of patterned boxes was generated using conventional SEM imaging, with a range of irradiation conditions. It was observed that the catalytic activity of patterned regions improved when irradiated with high dwell time, small pixel spacing, low accelerating voltage, and in the presence of water vapor, seen in Figure 3-3.

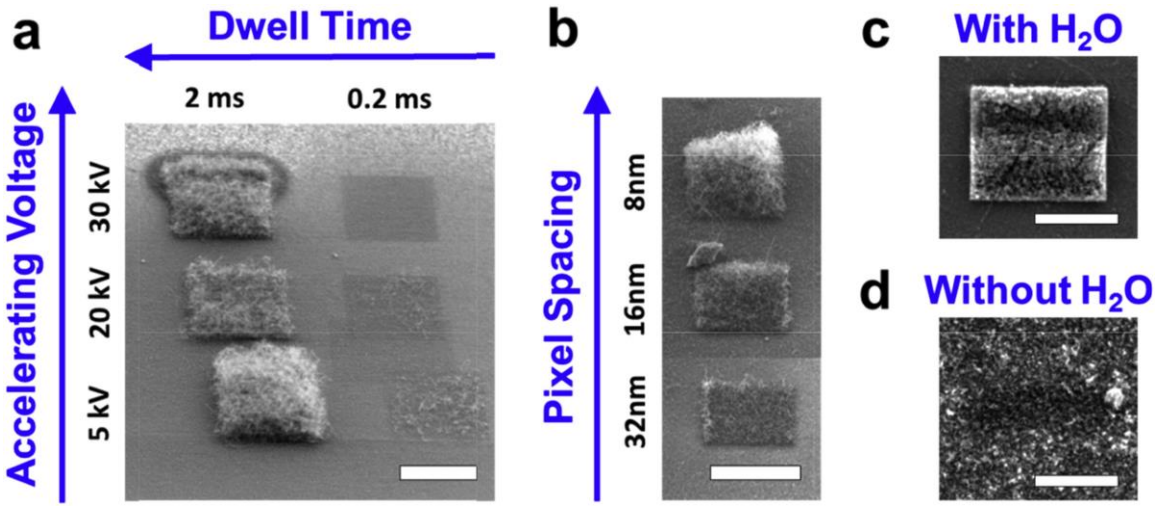

Figure 3-3. Controlled support activation via tuning of e-beam irradiation conditions in the presence of water. (a) Growth yield dependence on accelerating voltage and dwell time, with fixed pixel spacing. (b) Growth yield dependence on pixel spacing with fixed accelerating voltage. Increase in forest height is seen with decrease in accelerating voltage, increase in dwell time and small decrease in pixel spacing. Scale bar is 10 μm. (c) Forest growth using the e-beam chemistry process. (d) Sparse growth obtained in the absence of water-vapor.

Electrons have a classical wavelength in the femtometer range. However, a beam of electrons controlled by an ESEM, and interacting with both vapor phase and solid phase atomic species have an effective range that is much larger, in the nanometer scale. It is this range that determines the theoretical limit of pattern resolution in this process. Table 3-1 lists the factors that determine this feature resolution.

Table 3-1. Factors influencing feature resolution in e-beam processing techniques

Factor	**Sub-factors**
electron-beam probe size	electron optics, accel. voltage, working distance, beam profile
ESEM imaging conditions	dwell time, pixel spacing, vapor pressure, stage tilt
catalyst support material	density, atomic number, electrical conductivity

Interaction volume of the e-beam with the substrate material is the subsurface volume from which secondary electrons are generated when a primary electron strikes the surface. In general, higher accelerating voltage leads to better point resolution because the

beam probe size is decreased. However, secondary electron generation increases with a larger interaction volume. These secondary electrons may cause undesired reactions in areas away from the primary electron exposure, degrading the feature resolution. Such reactions include ionization of vapor phase water molecules and interactions with the molecules chemisorbed at the surface. The scattering cross-section of water increases at lower accelerating voltage[84]. A similar effect causes feature resolution loss in e-beam lithography processes. Therefore, the generation of secondary electrons is the most limiting factor during e-beam chemistry processing. Careful selection of the irradiation conditions (accelerating voltage, dwell time, and pixel spacing) can reduce the interaction volume and minimize secondary electron generation. The goal is to obtain a trade-off between obtaining a small probe size and reducing the generation of secondary electrons. Such a balance will yield optimal pattern fidelity and support activation efficiency.

Possible mechanisms of sapphire activation

The mechanism by which e-beam chemistry modifies the surface of sapphire and improves catalytic activity was investigated by analyzing many common phenomena encountered for various material systems in an ESEM[85, 86]. This mechanistic study found several physical and practical phenomena of beam-vapor-matter interactions and determined which are significant and which are negligible. In short, these interactions are:

- **Significant**: Knotek-Fiebelmann radiolysis, water radiolysis, hydroxyl formation and coverage, and the creation of non-stoichiometric sites
- **Negligible**: hydrocarbon surface contamination, localized beam heating, atomic displacement, knock-on damage, sublimation, and electrostatic charging

The remainder of this section will analyze each of these interactions and assess their effects on the sapphire surface and the catalyst particle evolution.

Role of water vapor

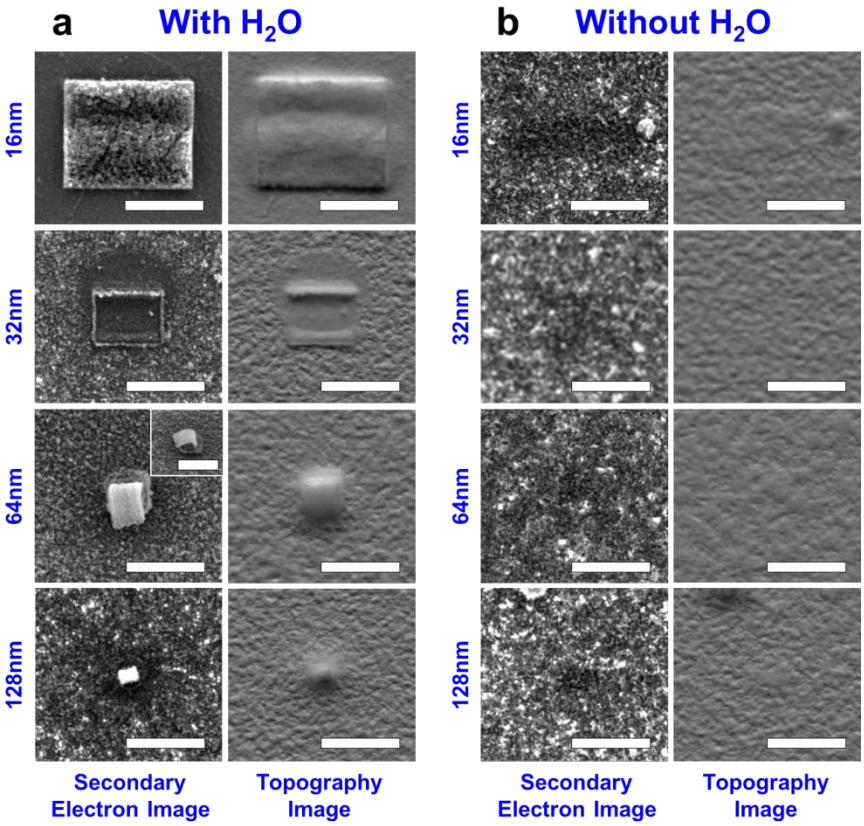

Figure 3-4. Secondary electron images and topography images of regions patterned in the presence (a) and absence (b) of water vapor for patterns generated using 10kV, 10mm working distance, and pixel spacings of 16nm, 32nm, 64nm and 128nm. A water vapor pressure of 0.1 Torr was used in (a). The scale bar in all images corresponds to 10μm.

A control experiment was completed by irradiating sapphire in high vacuum conditions (pressures of 10^{-5}-10^{-6} Torr), in the absence of water vapor, with all other conditions being held constant. The vacuum-irradiated support did not exhibit a significant increase in growth yield in the patterned areas once exposed to the CNT growth conditions, seen in Figure 3-4. This confirms that the presence of water vapor is essential to achieve activation of the catalyst support.

Cooperative radiolysis

Radiolysis of atomic species occurs when the incidence energy exceeds the threshold energy for ionization. This phenomenon can induce damage and loss of material in oxides by promoting the dissociation and desorption of oxygen via an Auger-driven mechanism [87-90]. Knotek-Fiebelmann (KF) radiolysis is responsible for the formation of holes and slots in oxides and several polymorphs of alumina including sapphire when irradiated in vacuum[91-94]. The e-beam can also induce radiolysis of water molecules and has been reported to accelerate the etching of CNTs and degrade of oxide surfaces[9, 84, 95-98]. For e-beam activation to take place, a cooperative mechanism is proposed, between the two radiolysis mechanisms (KF radiolysis and water radiolysis), as in Figure 3-5. KF radiolysis may generate active sites (vacancies) which are prone to interaction with water radiolysis products; water radiolysis products can functionalize the vacancy-rich surface and create non-stoichiometric sites with increased metal affinity and chemical reactivity. Although both radiolysis processes are present during e-beam chemistry, the inability to activate supports in the absence of water and the quenched activation at high accelerating voltage, where ionization cross-sections are smaller, suggest that water radiolysis represents the dominant mechanism for support activation. Therefore, activation efficiency should be tuned by selecting conditions that lead to radiolysis of water vapor.

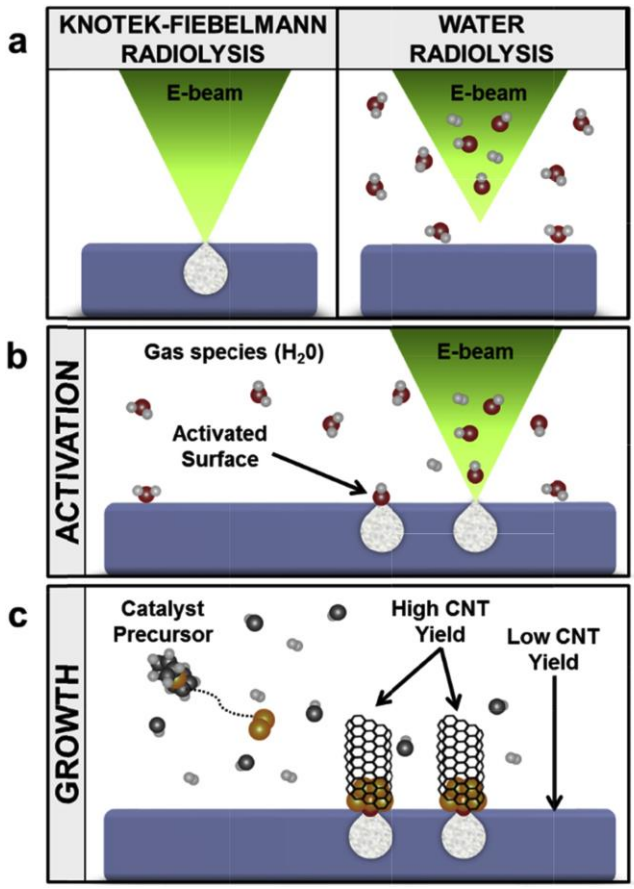

Figure 3-5. Cooperative radiolysis mechanisms responsible for catalyst support activation. (a) Knotek-Fiebelmann generates oxygen vacancies on the surface and water radiolysis generates reactive species. (b) Catalyst support activation is achieved when the two radiolysis mechanisms are coupled. (c) CNT growth takes place selectively in the activated regions.

Hydroxyl surface coverage

XPS analyses were conducted on activated regions immediately after patterning with three different conditions. Table 3-2 lists the conditions, where only dwell time is varied. The 0 μs value represents the control sample with no activation.

Table 3-2. E-beam conditions used for activation in XPS surface study

Parameter	Value
Dwell times	0 μs, 100μs, 400 μs
Acceleration voltage	10 kV
Pixel spacing	128 nm
Working Distance	10 mm
Water vapor pressure	0.1 Torr

The ratio between surface active species in sapphire, such as hydroxyl groups (O-H), and stable oxygen bonded to aluminum (O-Al) are a good indicator of the surface chemistry that occurs[75, 76, 78]. The O-H/O-Al ratios for these samples is shown in Figure 3-7a. An increase in the O-H/O-Al ratio is evident for samples activated using a larger dwell time. These conditions also exhibit an increase in carbon concentration and decrease in oxygen (O) and aluminum (Al) concentrations at the surface (Figure 3-6). The increase in the carbon concentration and thus $C1_s$ signal is ascribed to the ionization and precipitation of hydrocarbon contaminants (carbon over-layer) onto e-beam irradiated regions at nondestructive electron doses[99]. The carbon over-layer was considered during XPS quantification by performing a correction for the attenuation of the oxygen and aluminum signals. This correction was crucial to estimate the O/Al ratios as the photoelectrons generated by the sapphire, below the carbon over-layer, are attenuated by said layer. The model used to perform this correction and calculate the true O and Al intensities takes into consideration the thickness of the carbon over-layer, the ionization cross-section, the mean free path of the photoelectrons, and the contribution of C-O and OH-C=O to the O intensity (in the O-H component)[83]. Figure 3-7c shows the corrected O/Al ratios obtained using the model. As a reference, the O/Al ratio of clean sapphire (1.5) is depicted by a dashed line. Evidently, an increase in O/Al ratio is observed with increase in dwell time. The increase in O/Al ratio is consistent with the behavior exhibited in ion-beam engineered sapphire[75]. Like engineered sapphire, the observed increase in O/Al ratio of the activated supports can be attributed to an increase in hydroxyl surface coverage. For instance, the obtained O/Al ratio of 1.7 for supports activated using a dwell time of 400 μs corresponds to an increase in hydroxyl surface coverage of approximately 30%[83],

highlighting the excellent chemical control of the process. Therefore, e-beam activation can be used to achieve a desired hydroxyl surface coverage by tuning the irradiation conditions.

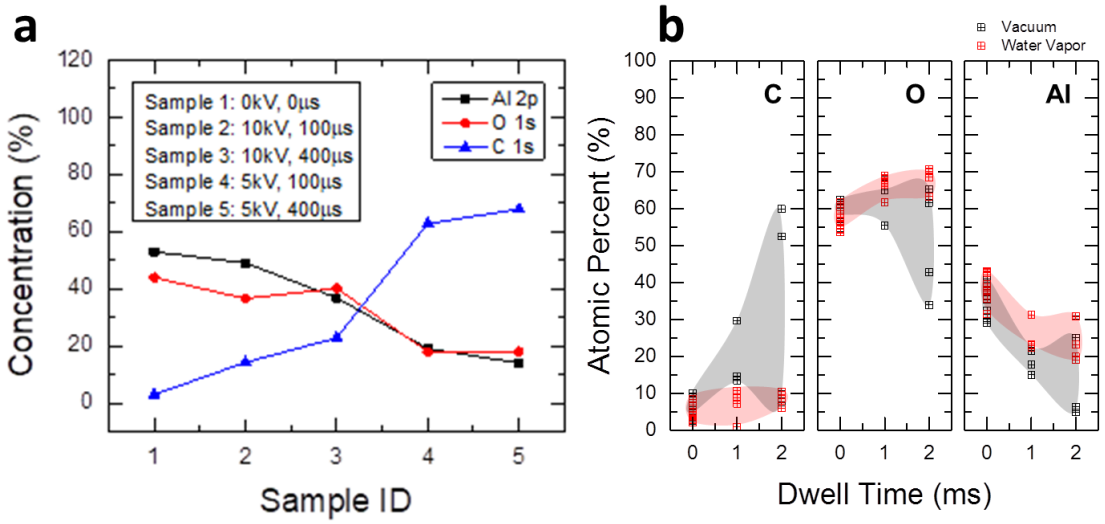

Figure 3-6. (a) XPS data for the water-assisted, e-beam activated surfaces before CNT growth. The relative concentrations for carbon, oxygen and aluminum at 0kV (no irradiated), 5kV and 10kV for the uncorrected areas under the curve of each region. The samples were irradiated using a dwell time of 100µs and 400µs and pixel spacing of 128nm. (b) Atomic Percent for carbon, oxygen and aluminum by EDS analysis for samples irradiated in the absence of water vapor (vacuum) and presence of water vapor. An increase in carbon signal is observed to be more significant in samples irradiated in the absence of water vapor during e-beam patterning.

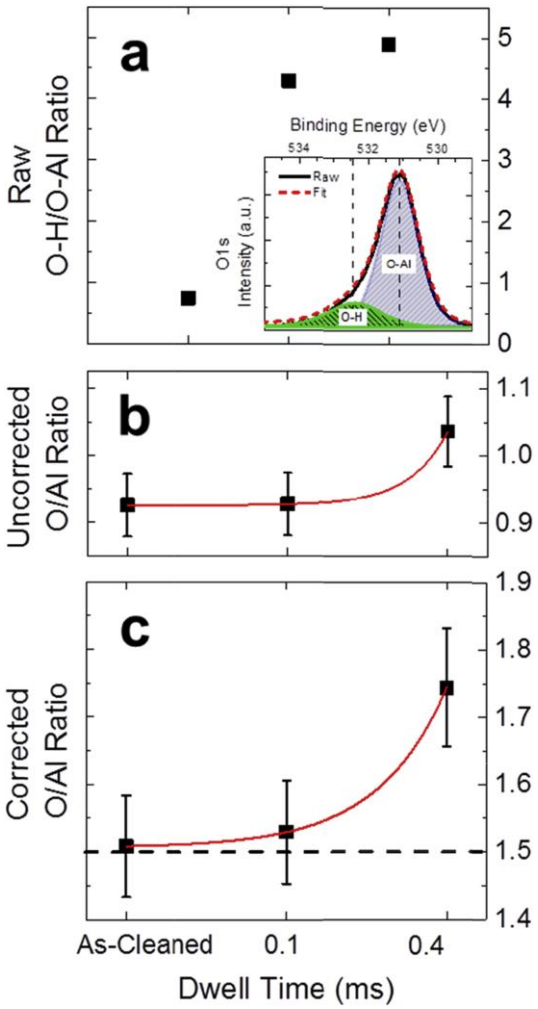

Figure 3-7. Analysis of the surface stoichiometry after e-beam chemistry. a) Raw O-H/O-Al ratios calculated from the oxygen 1s emission line in XPS for as-cleaned sapphire and water-assisted and e-beam activated sapphire with a 128 nm pixel spacing, a dwell time of 100 µs and 400 µs, and accelerating voltage of 10 kV. Inset shows the O-H/O-Al components for the sample irradiated with 10 kV and 400 µs. b) Uncorrected and (c) corrected O/Al intensity ratios for as-cleaned samples and samples exposed to e-beam chemistry. Reference O/Al intensity ratio for sapphire (1.5) is marked by a dashed line in (c). Higher O-H O/Al ratios suggest a non-stoichiometric surface and higher degree of hydroxylation for higher dwell time.

Surface roughness after activation

Surface roughness on activated surfaces was first monitored immediately after activation and again immediately after catalyst film deposition and evolution, seen in Figure 3-8. The surface roughness of activated regions increases by ~20× with respect to the as-cleaned sapphire. The e-beam process is much gentler than the ion beam process and

does not induce large changes in the surface profile, thus making it a more controllable patterning process.

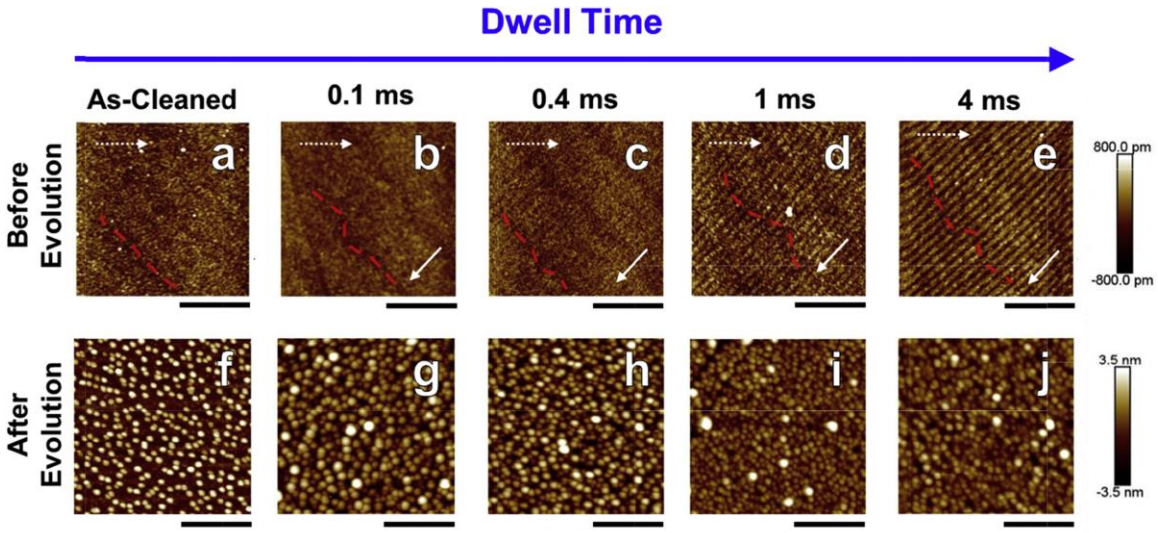

Figure 3-8. Reduced Ostwald ripening and catalyst coarsening obtained from surface roughness analysis. AFM height image series for water-assisted, e-beam activated sapphire before and after catalyst particle evolution. Smaller catalyst size is evident with increase in dwell time because of reduced Ostwald ripening and catalyst coarsening rates. Dashed arrows indicate the AFM scan direction while solid arrows indicate the e-beam scan direction during irradiation. Irradiation conditions: pixel spacing of 128 nm, beam current of 0.2 nA and accelerating voltage of 10 kV. The presence of step edges (a–e) suggests that no significant changes in the surface profile took place. Scale bars in (a–e) are 400 nm and (f–j) are 100 nm.

Carbon over-layer effect

An assessment was made of whether the support activation was affected by the presence of a carbon over-layer, which commonly occurs unintentionally in SEM imaging, due to electron beam induced deposition of amorphous carbon on all surfaces in the SEM vacuum chamber. EDS analyses were done on samples irradiated both in the presence and absence of water vapor to qualitatively compare the rate of hydrocarbon deposition. Here, irradiation was done prior to EDS analyses for an area of (10 μm^2) using the following parameters: acceleration voltage (10 kV), pixel spacing (16 nm), and dwell times (none,1 ms, 2ms). EDS spectra were collected using point analyses (0.8s/point) at multiple

locations of the patterned region. EDS analyses show that hydrocarbon deposition was more evident for samples irradiated in vacuum, indicating that hydrocarbon deposition does not lead to activation. The reduction in hydrocarbon deposition for samples irradiated in vacuum is likely associated with two factors: etching of hydrocarbons by highly reactive neutral O atoms and water radiolysis products, and a reduction in the hydrocarbons deposition rate, which happens preferentially in regions of high local electric fields when water vapor reduces electrostatic charging and charge-induced surface potentials[100, 101]. Furthermore, the removal of organic contaminants at 750 °C, where growth took place, reinforces the idea that hydrocarbons are not responsible for the enhanced catalytic activity.

Localized zone heating

Heat dissipation analysis can be used to determine that the creation of localized hot zones is negligible. Previous studies have shown that 20kV e-beam shows negligible heating on a titanium oxide sample[99, 102]. The peak substrate temperature is determined by summing the global temperature of the bulk substrate with a local hot spot at the e-beam center. This local hot spot temperature is approximated by

$$\Delta T = \frac{3VI(1-\eta)}{2\pi\kappa\left(\frac{R_e}{2}+D\right)} \qquad \textbf{Eq. 3-1}$$

where accelerating voltage V=5 kV, probe current I=0.2 nA (measured in vacuum), backscatter electron coefficient η=0.19 (for Al at 5 kV), thermal conductivity κ=30 W/mK (at room temperature), electron range R_e=100nm (at 1MeV), and probe diameter D ($D<<R_e$). With these conditions, the temperature rise is ΔT=0. 26°C. However, at 5kV, R_e is reduced to R_e=10nm and ΔT=2.6°C. In the presence of water vapor, the probe current *I*

decreases, and the temperature rise should decrease further reduced. Therefore, that neither heating nor any heat related mechanism influences the activation of sapphire.

Electrostatic charging

Electrostatic charging is not a possible mechanism since samples irradiated in high vacuum did not undergo activation despite experiencing higher electrostatic charging. In fact, this pathway acted detrimentally on the activation process; quenching of activation in high vacuum may be caused by charge-induced surface potentials which can create a beam decelerating field[100, 101], lower the effective dose and kinetic energy of the incident beam, and promote excessive hydrocarbon precipitation.

Knock-on damage

The threshold energy required to cause either knock-on damage or sputtering of oxygen and aluminum atoms is higher[85, 86] than the accelerating voltages used in this process, so these two pathways are probably not a viable explanation of the mechanism. Atomic displacement of a material can take place if sufficient energy from incident electrons can be transferred to the target atom, more than the displacement energy of the atom. If an incident electron has energy E_0, then the max allowable transferable energy is

$$E_{max} = 4E_0 \frac{m_e}{m_a} \qquad E_{max} > E_d. \qquad \textbf{Eqs. 3-2,3}$$

Taking E_0=5 keV, the electron mass m_e=9.1x10^{-28} g/atom, and atomic masses m_a(O)=2.66x10-23 g/atom and m_a(Al)=4.48x10^{-23} g/atom. For oxygen, E_{max}(O)=0.684 eV < E_d(O)=44-50 eV, and hence atomic displacement of oxygen is not a possibility. For aluminum, E_{max}(Al)=0.406 eV < E_d(Al)=17 eV, also eliminating atomic displacement of aluminum. At E_0=30keV, these values increase to E_{max}(O)=4.11 eV and E_{max} (Al)=2.44 eV, clearly indicating that employed imaging conditions would not lead to knock-on.

Sublimation

The threshold energy for this displacement to take place is E_0' =180 keV. As in the case of atomic displacement, E_{max} needs to exceed the sublimation energy (E_s) such that $E_{max} > E_s$. Calculated threshold incident energies for the onset of sputtering in solids shows that the sputtering threshold for aluminum is $E_0 > 30$ keV, which states that sputtering at the current irradiation conditions does not satisfy atomic displacement conditions.

Catalyst evolution / particle number density

Figure 3-10 shows that activated regions have increased catalyst particle pinning. The interaction between metals and alumina is highly dependent on the presence of active sites, hydration level, and stoichiometry[103-105]. Surface stoichiometry can alter the physico-chemical properties of the deposited metal film, strengthen metal/support interactions, and enhance catalytic activity[106]. Density functional theory (DFT) calculations have found a correlation between the local density of states and the strength of the metal/support interactions and have shown that unfilled valence band metals can interact more strongly with non-stoichiometric alumina[107]. Increased adhesion may also enhance carbon solubility into the catalyst during growth, as demonstrated using molecular dynamics simulations[108].

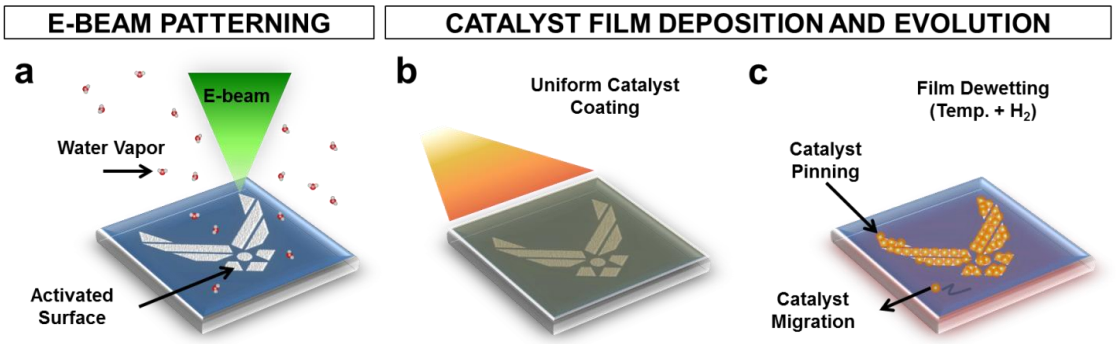

Figure 3-9. Schematic of the protocol followed for catalyst evolution experiments. (a) Surface activation is followed by uniform catalyst film coating via ion sputtering (b) and heat treatment under a hydrogen atmosphere for catalyst evolution (c).

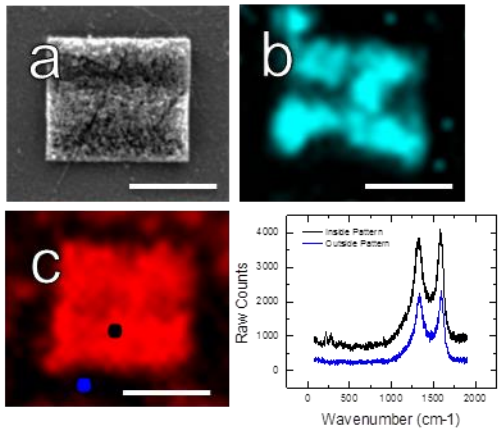

Figure 3-10. Increased CNT catalytic activity on water assisted, e-beam irradiated sapphire. (a) SEM micrograph of CNTs grown on an irradiated area using a 10kV e-beam, 100µs dwell time, 0.2nA beam current and 128nm pixel spacing. (b & c) Raman map corresponding to the peak intensity at 222cm-1 (iron oxide resonance peak) and 1585 cm-1 wavenumber (from the G-Band in CNTs). A larger amount of iron catalyst and CNTs is observed at the irradiated area (b & c). (d) Raman spectra for two regions of interest depicted in (c).

This knowledge of surface stoichiometry and catalyst-support interaction behavior was then further investigated by XPS analyses to understand the preferential catalyst adhesion and increased local particle density.

After catalyst deposition and substrate heating, AFM was used to observe the evolution of surface properties and catalyst particles. The surface roughness decreased and the particle number density increased, as in Figure 3-11. Increasing the dwell time causes

an increase in catalytic activity. Therefore, support activation impedes Ostwald ripening, keeps the catalyst smaller, and hence allows more catalysts to stay catalytically active.

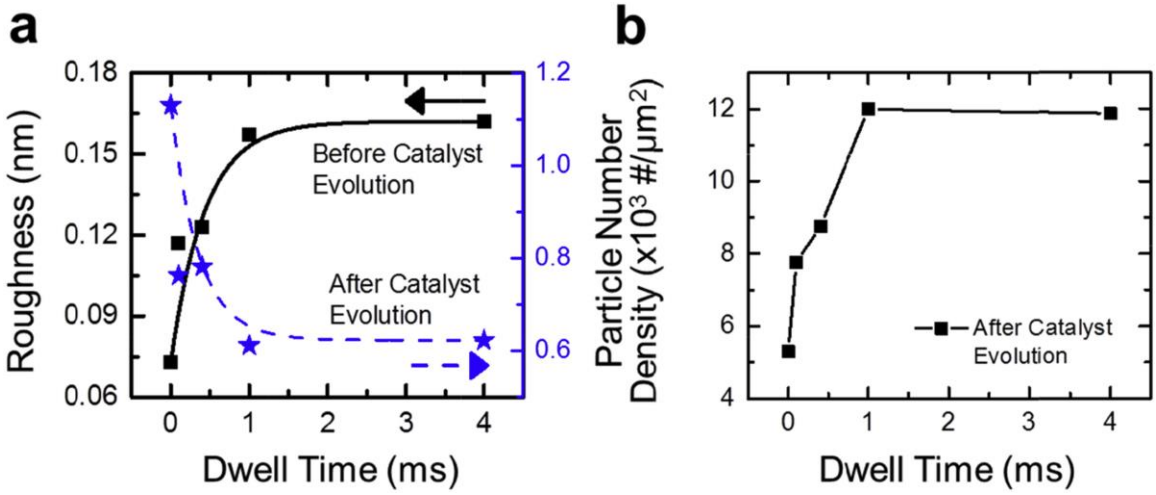

Figure 3-11. Surface roughness dependence on surface activation conditions shows impeded catalyst evolution to retain smaller catalyst size. a) Roughness variation as a function of dwell time for 0.1, 0.4, 1 and 4 ms. Solid and dashed lines represent the exponential fit for surface roughness studies before and after catalyst evolution, respectively. b) Correlation between surface roughness after activation and particle number density after catalyst evolution for select dwell times. Particle number increases with increase in surface roughness.

Pattern Reproducibility

Pattern reproducibility, as in the case of e-beam lithography and other surface modification techniques, is dependent on batch-to-batch variability of support material, as well as environmental conditions to which the support is exposed to, such as humidity of the laboratory space.

Conclusions

A process is demonstrated to induce morphological and chemical modifications that activate c-cut sapphire to support CNT forest growth. The process uses e-beam irradiation in the presence of water vapor to modify the catalyst support surface with spatial and chemical precision. The irradiated supports exhibit an increase in catalytic activity and

subsequent growth of tall, vertically-aligned forests selectively at the irradiated regions. Support activation took place only at exposed locations, with minimal catalytic activity and CNT growth outside the patterned regions despite exposing the entire support to the CNT catalyst and precursors. Catalyst evolution studies and surface stoichiometry measurements suggest that catalytic activity is dictated by the surface roughness and basicity of the modified surface. Support activation is ascribed to two radiolysis-based mechanisms: first, the modification of the support surface and increase in support roughness via desorption and dissociation of oxygen; second, the generation of a non-stoichiometric surface (with enhanced metal particle interaction and catalytic activity) via interaction of the surface with water radiolysis products. The novel e-beam chemistry process presents an attractive alternative for e-beam lithography; its superiority lies in the ability to control catalysts positioning without the need for masks, polymer resists, or etching procedures. More importantly, the technique is not exclusive to CNT growth and could be extended to a variety of substrates and gases to achieve a wide range of chemistries. With future improvement, the process could be used to modify surface stoichiometry and composition using excellent spatial and chemical control.

CHAPTER 4 - PRECISION MILLING OF CNT FORESTS WITH ENVIRONMENTAL SEM

Abstract

A nanoscale fabrication technique to mill carbon nanotube (CNT) forests is introduced. An environmental scanning electron microscope (ESEM) is used to mill or etch away carbon materials with precise and scalable control. The electron beam interacts with the low-pressure water vapor ambient in the ESEM, dissociating water molecules into hydroxyl radicals and other species by radiolysis. In the region near the surfaces of CNTs, the radical species interact with carbon atoms, affecting the chemical bonds and structure. The portion of the electron beam that does not interact with water vapor, irradiates the CNTs and provides additional energy necessary for bond-breaking. The strong covalently bonded carbon atoms are then susceptible to oxidation from the chemical products of radiolysis and get carried away in gaseous form. This technique may be used to trim a selected region of an individual CNT, or it may be used to remove hundreds of cubic microns of material by adjusting ESEM parameters. The machining resolution is close to that of the imaging resolution of the ESEM itself. The technique produces only small quantities of carbon residue along the boundaries of the cutting zone, with minimal effect on the native structural morphology of the CNT forest. Other carbonaceous materials such as graphene, diamond and biological tissue are also viable candidate materials for use with this technique.

Introduction

Carbon nanotubes (CNTs) and graphene are nanostructure carbon materials that attract significant research attention because of their superior strength, durability, thermal,

and electrical properties. Precision machining of carbon nanomaterials has emerged as recent research topic because it offers an excellent way to employ these materials towards a variety of engineering applications. Machining CNTs and graphene requires nanoscale spatial precision to first locate a nanoscale area of interest and then to selectively remove that material. ESEMs are unique because they allow both the mode of locating and imaging a nanoscale region of interest, and a method of performing material interactions.

Consider the machining of vertically aligned CNT forests. Lithographic patterning of catalyst films can precisely define the cross-sectional shape and structure of CNT forests, as shown in Figure 4-1. However, the external surface of the forests is often poorly ordered with non-uniform height. For surface-sensitive applications such as thermal interface materials, the irregular surface may impede optimal surface contact and reduce device performance. Precision trimming of the irregular surface to create a uniform flat surface could potentially offer better, more repeatable performance by maximizing the available contact area.

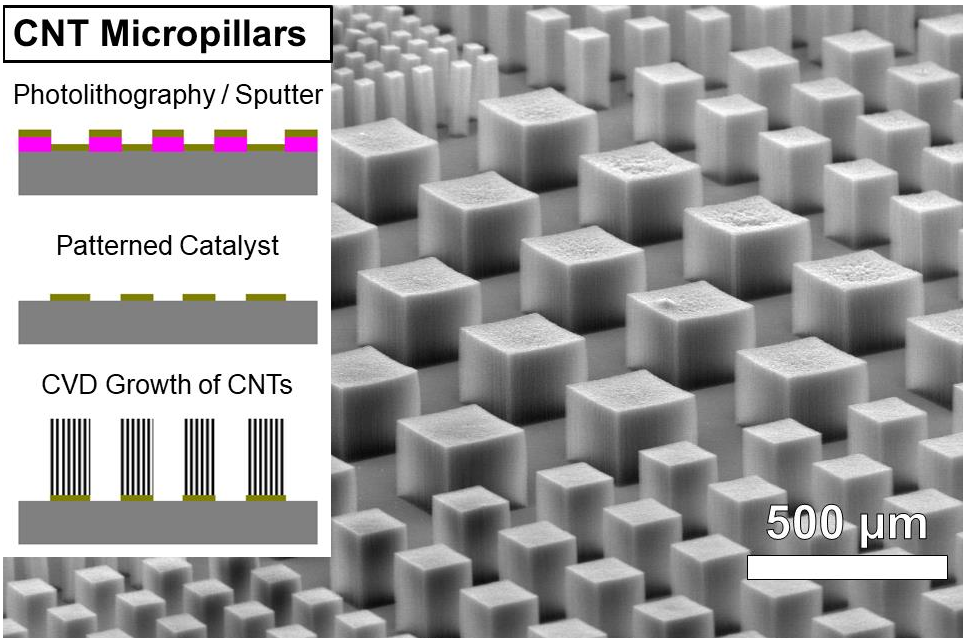

Figure 4-1. Array of lithographically-patterned CNT forest pillars, with varying cross-sectional sizes. Note the non-flat top surfaces. Gradients in growth kinetics cause predictable curvature, either concave or convex. Also, random and localized defects create unpredictable surface morphology [10].

Precision machining techniques for nanomaterials frequently do not resemble conventional macro-scale mechanical machining technologies such as drilling, milling, and polishing by means of hardened tooling. To date, techniques using energetic beams have been most successful at site-selective milling of carbon nanomaterials. These techniques include laser[109], electron beam[95], and focused ion beam (FIB) irradiation[110]. Of these, laser machining techniques provide the most rapid material removal rate[109, 111]. However, the spot size of laser systems is on the order of many microns and is too large to isolate nanometer-scale entities such as a single carbon nanotube segment within a densely populated forest. By contrast, electron and ion beam systems produce a beam that may be focused to a spot that is several nanometers or less in diameter.

FIB systems are specifically designed for nanoscale milling and deposition of materials. These systems use an energetic beam of gaseous metal ions (typically gallium)

to sputter material from a selected area. FIB milling of CNTs is achievable, but often with unintended byproducts including gallium and carbon redeposition in surrounding regions of the forest[110, 112]. When the technique is used for CNT forests, the redeposited material masks and/or alters the morphology of selected milling region, altering the native appearance and behavior of the CNT forest. The gallium may also implant within the CNT, providing electronic doping. Such consequences often make FIB-based milling prohibitive for CNT forests.

Transmission electron microscopes (TEMs) use a finely focused beam of electrons to probe the internal structure of materials. Acceleration voltages for TEM operation typically range from 80-300 kV. Because the knock-on energy of CNTs is 86.4 keV[113], the electron energy produced by TEM is sufficient to directly remove atoms from the CNT lattice and induce highly localized milling, capable of milling CNTs with sub-nanometer precision[114-116]; however, the process is very slow – often requiring minutes to cut through a single CNT. Importantly, TEM-based milling approaches require CNTs to first be removed from a growth substrate and dispersed onto a TEM grid for processing. As a result, TEM-based methods are generally not compatible with CNT forest milling in which the CNTs must remain on a rigid substrate.

Milling of CNT forests by scanning electron microscopes (SEMs) has also received attention. In contrast to TEM-based techniques, SEM instruments are typically unable to accelerate electrons with sufficient energy to impart the knock-on energy required to directly remove carbon atoms. Rather, SEM-based techniques use an electron beam in the presence of a low-pressure gaseous oxidizer[117]. The electron beam selectively damages the CNT lattice and may dissociate the gaseous ambient into more reactive species such as

H_2O_2 and the hydroxyl radical[84]. Water vapor and oxygen are the most commonly reported gases to achieve selective area etching. Because the SEM-based techniques rely on a multiple-step chemical process[97], numerous processing variables may influence the milling rate and precision of the process. Increasing acceleration voltage and beam current directly increase the milling rate because of an increased energy flux[9]. The effect of chamber pressure of is less obvious. A pressure that is too low suffers from a deficiency of the oxidizing agent, decreasing the milling rate. Further, an over-abundance of gaseous species scatters the electron beam and decreases the electron flux in the milling region, also decreasing the material removal rate.

A continuum model was employed to estimate the carbon removal rate [118], whereby electrons interact with precursor molecules near the surface to generate reactive species that etch the substrate surface. From this model, the etch rate is estimated as

$$Etch\ Rate\ \approx \frac{N_A}{Z} x A_\sigma \Gamma_e \qquad \textbf{Eq. 4-1}$$

where N_A is the surface concentration of the etchant species, Z is the surface concentration of available reaction sites, *x* is a stoichiometry factor relating the volatile etching products generated relative to the reactants, A_σ represents the probability of generating the desired etching species from an electron-water vapor collision, and Γ_e is the electron flux at the surface. The factors of *x* and A_σ are assumed to be unity, while Z is assumed to be nearly constant and significantly larger than N_A. A full analysis of this model[9] provides an explanation how the material removal rate is influenced by the acceleration voltage, beam current, dwell time, operating pressure, and CNT orientation.

The focus of this work is to take the understanding of the mechanism ESEM milling of nano-carbon materials and give a detailed procedure of operation. Further,

this work aims to demonstrate that the technique is invaluable option for manipulating CNT pillars for engineering applications. Emphasis is placed on removing relatively large (>100 μm^3) material volume from a CNT forest with relatively aggressive processing conditions.

Methods

A video representation of the following methods section is available online[119]. Visual demonstration of this method is critical because the carbon nanotube milling steps are quite different than those used for conventional SEM-based imaging techniques. The **Materials List** in the next section outlines required software and hardware.

Preparation of CNT Forest Sample for Milling

CNT Synthesis

1. Deposit 10 nm of aluminum oxide (alumina) on a thermally oxidized silicon wafer using atomic layer deposition[76] or other physical vapor deposition methods.
2. Deposit 1 nm of iron on the alumina support layer by sputtering[120] or other physical vapor deposition method.
3. Synthesize CNTs using an established process, such as thermal chemical vapor deposition[121]
    1. Heat a 20 mm diameter tube furnace to 750 °C in 400 standard cubic centimeters (sccm) of flowing helium and 100 sccm hydrogen. Introduce 100 sccm ethylene as a hydrocarbon feedstock gas for a growth rate of approximately 50 μm/min.

SEM Preparation

*When handling the sample and the sample stub, it is important to wear disposable nitrile gloves. This will prevent oils from being transferred to the stub or sample and consequently deteriorating the effectiveness of the ESEM vacuum pumps.

1. Apply carbon tape to a standard 1/2" diameter SEM stub. If tilting the stage is required, overlap the region of the CNT forest sample to be milled over the edge of the stub. If software-controlled electron beam rastering will be used in the milling procedure, secure the CNT sample to an electron beam lithography mount in a similar manner.
2. If milling the CNT cross section, secure the stub to a 45° stub holder with a set screw.
3. Vent the ESEM by selecting the "Vent" icon from the ESEM control software.

4. Open the ESEM stage door and secure the stub to the SEM stage with a set screw.
5. Close the SEM chamber and select “High Vacuum” in the ESEM control software.
6. While the ESEM chamber is pumping, select the electron beam parameters of 5 kV and spot size of 3.0 using the Beam Control tab within the control software.
7. Select the secondary electron detector by selecting Detectors | ETD(SE) in the ESEM control software.
8. Select the “Beam On” icon in the control software. The beam can be activated only once the chamber vacuum is less than 10^{-4} Torr. Use manual SEM focus control knobs to focus the sample.
9. Tilt the sample to 45° using manual tilt stage control knob or by inputting 45° in the “Tilt” field in the “Coordinates” tab of the ESEM software. Focus on the highest sample. Link the focal distance to the working distance by selecting Stage | Link Z to FWD in the ESEM software menu. Input 7 mm into the “Z” field in the “Coordinates” tab within the control software.
10. Adjust focus, stigmation, brightness and contrast using the manual control knobs to resolve a well-focused image.

Beam Adjustment in High Vacuum Mode

1. Locate a region for milling using navigation controls. Double click within the SEM image view or by manually turning the x and y control knobs of the SEM stage control to navigate.
2. Navigate to an adjacent location approximately 100 μm away from the milling region.
3. Consult Figure 4-6 to estimate the material removal rate of the CNT forest as a function of pressure, acceleration voltage, dwell time per pixel, and beam current.
4. Adjust the acceleration voltage to 30 kV and spot size to 5.0 using the ESEM control software. Adjust image focus, brightness, and contrast using the ESEM control knobs. For nanometer-scale milling of individual or few CNTs, select 5 kV and spot size of 3.0.
5. Select a 1 mm aperture by manual aperture adjustment. Adjust focus, stigmation, brightness, and contrast to obtain a well-resolved image, as previously detailed.
6. Decrease magnification to < 1,000x.

SEM Setup in Low Pressure Water Vapor

1. Select a pressure of 10 Pa in the control software dropdown box.
2. Select “Low Pressure” mode in the “Vacuum” settings in the ESEM software to introduce water vapor.
3. Select “Beam On” in the control software upon pressure stabilization. Select a dwell time of <10 μs and a resolution of 1024 x 884 in the drop-down boxes of the control software.
4. Adjust the image brightness, contrast, focus, and stigmation as previously detailed.

5. Navigate to the desired milling region. Rotate the image orientation by selecting Scan | Scan Rotation in the control software, if required. Select a suitable rotation angle that aligns with the native vertical and horizontal scan orientation of the SEM.
6. For milling feature sizes on the order of 1 μm, select a magnification of 40,000x. Select a magnification of 20,000x to mill features with dimensions up to 5 μm.
7. Pause the electron beam by selecting the pause (||) icon. An image of the CNT forest will be displayed and may be used for selecting reduced area milling regions while the beam is paused.

CNT Forest Milling

CNT forest milling using a rectangular selected area

1. Choose the 'Reduced Area' tool in the control software or select Scan-Reduced Area in the software menu. Extend a reduced area rectangle over the area to be milled.
2. Adjust the image resolution to 2048 x 1768. Increase the dwell time to 2 ms. If 2 ms is not available, navigate to the Scan | Preferences and select the "Scanning" tab. Select an existing scan time and type "2.0 ms" into the "Dwell Time" field. Click "OK" to close the menu.
3. Select the pause (||) icon in the control software to activate the electron beam.
4. Select the pause (||) icon so that the beam rasters over the selected area one time. Select the icon immediately after step 2.1.3. The scan duration depends on the size of the selected area, resolution and dwell time and may be approximated by multiplying the number of pixels within the scan area and the dwell time per pixel.
5. Decrease magnification to < 1,000x once the beam has completed rastering the selected area. Revert to the parameters used in step 1.3, including High Vacuum. Select "Beam On" to engage the beam.

CNT forest milling along a horizontal line

1. Select the line scan feature by navigating to Scan | Line in the control software. The size of the electron determines the line width beam. Adjust the image resolution to 2048 x 1768 from the control software dropdown box. Increase the dwell time to 2 ms.
2. Using the still image acquired before pausing the electron beam, place the line over the area to be milled.
3. Select the videoscope icon or navigate to the Scan menu and select "Videoscope." Using the Videoscope tool provides feedback relative to when a line scan has fully completed.
4. Select the pause (||) icon to scan electron beam across the width of the line.
5. Select the pause (||) icon to blank the electron beam.

CNT Forest milling using software-controlled electron beam rastering

1. Pattern Generation
    a. Design a milling pattern of interest using a CAD software package such as AutoCAD.
    b. Using "Nanometer Pattern Generation System" (NPGS) software, import the CAD pattern file.
    c. Convert the shapes to solid features by selected "Filled Polygons" in the NPGS software.

d. Save the drawing as a '.dc2' file in a designated project folder of NPGS.
e. Using NPGS, navigate to the project folder containing the ".dc2" file. Right select the ".dc2" file and select "Run File Editor" to convert the drawing to NPGS code. Typical parameters used to pattern CNT forests at given conditions are as listed below:
    - Center-to-center distance = 5 nm
    - Line Spacing = 5 nm
    - Magnification = 10,000x
    - Desired Beam Current = 26 nA
    - Line Dose = 100 nC/cm

2. Electron Beam Milling using NPGS Lithography Software
3. Select the "NPGS Mode" in NPGS software button to give control of the SEM to NPGS.
4. Highlight the pattern file and select "Process Run File" in NPGS to initiate milling.
5. Select "SEM Mode" in the NPGS software when patterning is finished. Select "High Vacuum" in the ESEM control software.
6. Select "Beam On" to inspect the milled region. Refer to the "Beam Adjustment in High Vacuum" section.

Sample Removal

Vent the chamber by selecting "Vent" in the ESEM control software.
Open the ESEM door. Remove the stub by loosening the set screw.
Close the chamber door. Select "High Vacuum" in the control software.

Results

An ESEM procedure is demonstrated to precisely mill CNT forests. Several ESEM and material situations are explored and demonstrated. The technique offers many benefits over other methods; it does not require delamination of the CNT forest for processing, it does not introduce external heavy elements that may significantly alter the surrounding CNT forest morphology, and it is scalable up to larger volumes of material with programmable shapes and tunable material removal rates. Additionally, this method is expected to be similarly applicable for graphene, diamond, biological cells and other carbon-based materials.

Firstly, a relatively-large micron-scale area was selected for milling, at the top surface of a CNT forest pillar. A high material removal rate was desired, so the ESEM conditions were:

Acceleration Voltage	Water Vapor Pressure	Beam Spot Size	Beam Dwell Time	Aperture Size	Scan Magnification
30 kV	11 Pa	5.0	2 ms	1 mm	20,000x

A rectangular area was rastered with the beam such that the irregular top surface to be removed is enclosed within the rectangle. SEM micrographs of the CNT forest pillar are shown in Figure 4-2 before and after the milling process. The red line in the figure represents the lower bound of the rectangle used for milling.

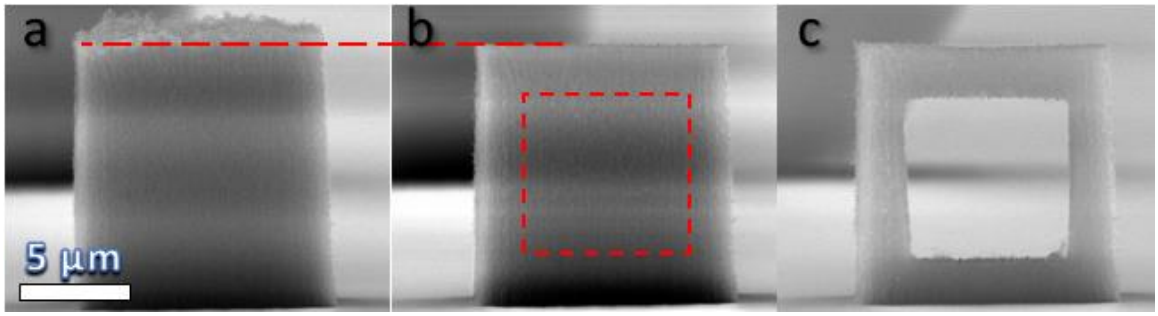

Figure 4-2. A 10 µm wide CNT forest pillar (a) before milling and (b) after milling top edge (c) after milling internal square.

Another CNT forest was milled in both the axial and transverse directions, relative to the native CNT orientation, to investigate the effect of CNT orientation on material removal rate. A factor of roughly two is observed in cutting rate, with the transverse direction being faster, presumably due to the difference in the projected areal density. Much interstitial space betwixt adjacent CNTs allows for faster milling in the perpendicular direction. Material removal rate is discussed further below.

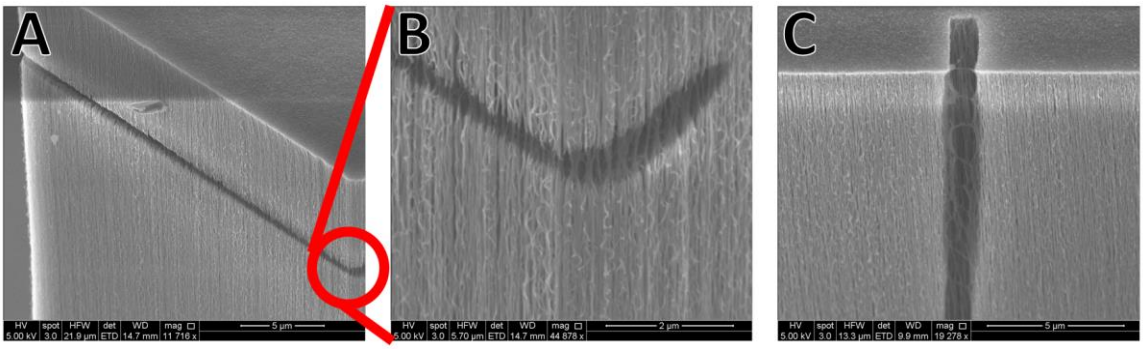

Figure 4-3. A comparison of the effect of CNT orientation on the milling rate. Parallel to the CNT axis is generally slower than perpendicular direction, due to the increased areal density. (a),(b) the electron beam rasters perpendicular to the CNTs, across the forest sidewall. (c) Electron beam is parallel to CNTs, rastering along the top of the forest.

Non-rectangular geometries can be achieved using software-controlled electron beam rastering[81]. As shown in Figure 4-4, a 15 μm diameter circle was milled into a relatively short 20 μm tall CNT forest. The beam was directed in parallel with the growth direction of the CNT forest, which is normal to the substrate. Figure 4-4 shows that the process milled the CNTs to the underlying silicon substrate. Milling parameters used for this test were:

Acceleration Voltage	Water Vapor Pressure	Beam Spot Size	Beam Dwell Time	Aperture Size	Scan Magnification
30 kV	11 Pa	5.0	2 ms	1 mm	10,000x

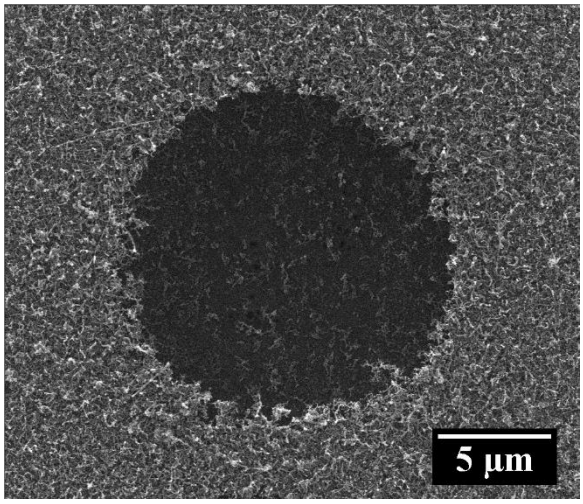

Figure 4-4. Software-controlled electron beam rastering is used to define and mill a 15 µm diameter circle in a CNT forest. In this test, the milling direction was parallel to the CNT growth direction from the top surface to the underlying substrate.

The technique is also fully capable of milling nanoscale features, such as segments of individual CNTs, as seen in Figure 4-5. While milling rectangular areas, the electron beam rasters the enclosed region only one time but the area may be scanned multiple times if additional cutting depth is desired. This precise cutting demonstrates that it is minimally disruptive and preserves native CNT forest structural morphology. ESEM parameters for this test were:

Acceleration Voltage	Water Vapor Pressure	Beam Spot Size	Beam Dwell Time	Aperture Size	Scan Magnification
5 kV	11 Pa	3.0	2 ms	30 µm	140,000x

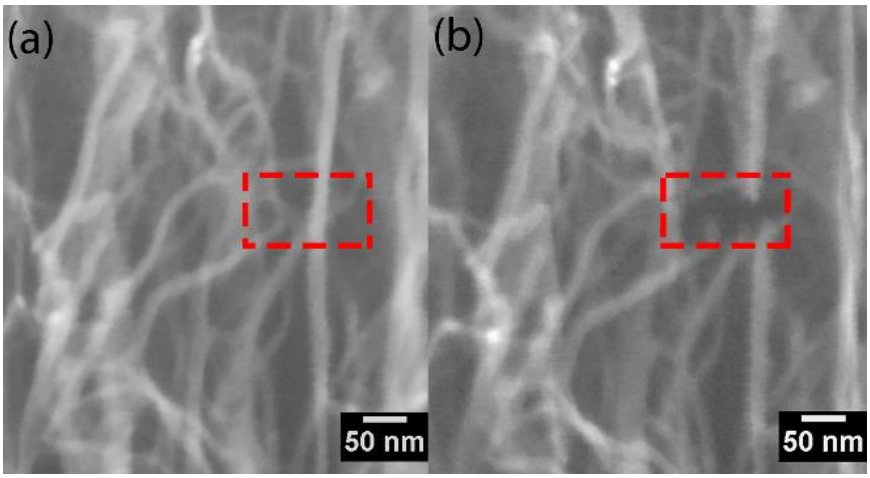

Figure 4-5. SEM micrograph showing individual CNTs from within a forest. The beam was focused to a small rectangle over an individual CNT. (a) before and (b) after milling[9].

Material removal rates (MRR) were measured for a CNT forest[9], as shown in Figure 4-6. The chemical mechanism for etching carbon atoms is ultimately responsible for the MRR, but it is experimentally found to be a function of both ESEM parameters and carbon material parameters. The ESEM parameters affecting MRR are water vapor pressure, acceleration voltage, beam current, and dwell time. The material dependent properties affecting MRR are CNT areal density, diameter, and alignment. Although the exact mechanism of reaction is not explored in this work, water vapor plays a critical role, as evidenced by the lack of CNT damage or etching when performing the procedure in the absence of low-pressure water vapor.

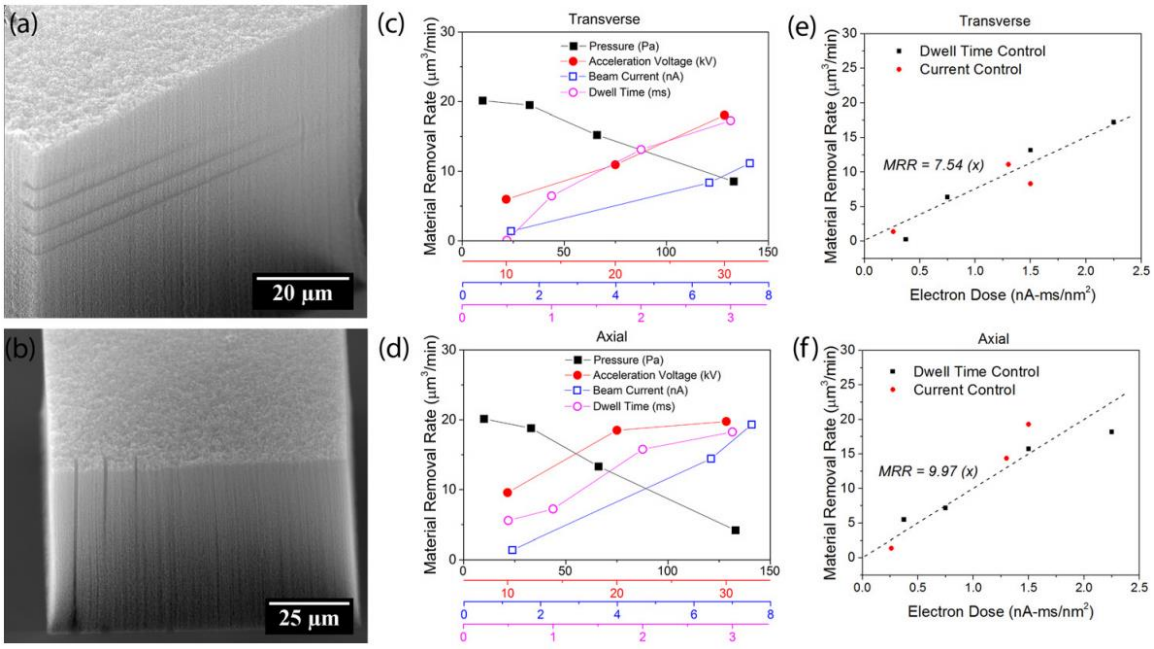

Figure 4-6. Material removal rate (MRR) variation. SEM micrographs demonstrate the MRR in the transverse direction (a) by varying operating pressure from 133, 66, 33, 66, and 11 Pa (top to bottom) and (b) in the axial cutting direction by varying dwell time from 3, 2, 1, and 0.5 ms/pixel (left to right). The MRR is plotted as a function of incremental changes in pressure, acceleration voltage, beam current, and dwell time in the (c) transverse and (d) axial cutting directions. The MRR as a function of electron dose varies nearly linearly in both the (e) transverse and (f) axial milling orientation.[9].

High values of electron beam dwell time, current, and acceleration voltage are frequently avoided for imaging of carbon-based materials, but these aggressive parameters are critical for achieving fast enough cutting rates for micron-scale milling. While qualitative trends of material removal rate are expected to hold for CNT forests, some experimentation may be required to find the optimal parameters for other carbon material systems. Best practices for milling depend on the feature size intended to be milled. In general, the material removal rate may be increased by increasing the acceleration voltage, spot size, and aperture diameter. These parameters all increase the energy flux of the electron beam.

This technique is currently being used to examine the internal structural morphology of CNT forests. Because structural morphology is intimately linked with functional properties[21, 34, 37, 40, 122], characterization of CNT forest morphology in three-dimensional space may provide additional insights into the governing structure-property relationships. With the ability to precisely mill into a forest and observe the internal nanotube interactions, CNT forest synthesis modeling and analytical models can be tuned and validated.

The emphasis of the ESEM milling technique to date has been directed towards rapid material removal with less focus on optimizing conditions for reducing the residual carbon residue. While the technique is relatively clean compared to FIB-based milling, small amounts of carbon residue exists on milled surfaces. A future direction is to explore the mechanism of amorphous carbon deposition in the immediate vicinity of the cut surfaces when large volumes of materials are removed, as shown in Figure 4-7. With a broad parameter space available for exploration, including environmental gas composition, vapor pressure, acceleration voltage, probe current, and electron beam rastering conditions, enhanced surface cleanliness may be achieved.

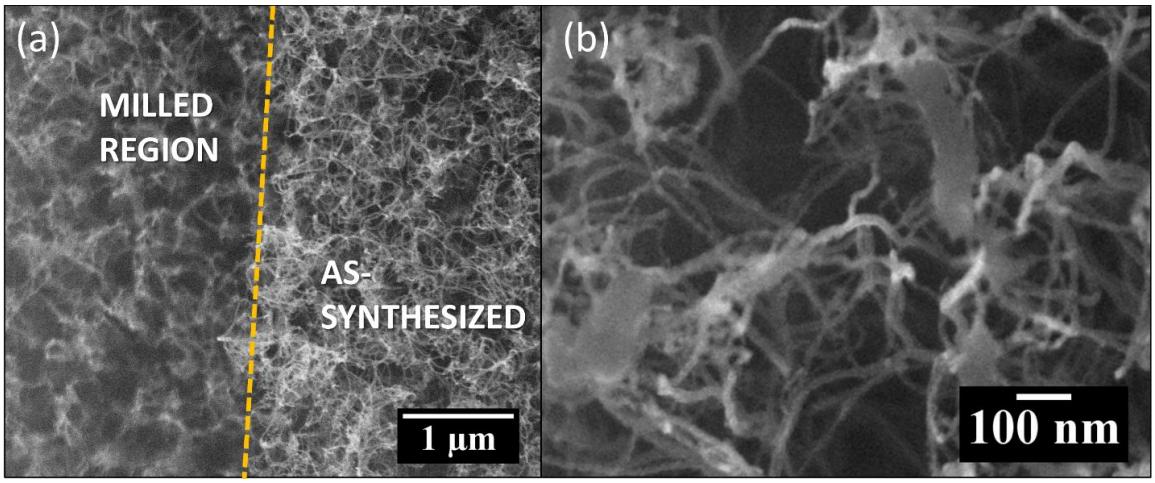

Figure 4-7. SEM micrographs showing the surface finish of ESEM milled CNT forests. (a) The top surface of a CNT forest shows the surface variation between the milled and as-synthesized regions. (b) Higher magnifications reveal that some amorphous carbon deposits are left behind during the cutting process.

Materials List

Table 4-1. Hardware and software necessary to grow CNT forests and selectively etch and mill carbonaceous material

Name	Company	Catalog Number	Comments
100 mm diameter silicon wafer with 1 micron thermal oxide	University Wafer		Sample substrate
Iron sputter target	Kurt J. Lesker	EJTFEXX351A2	Sputter target
Savannah 200	Veeco / Cambridge Nanotech		For atomic layer deposition of alumina
Quanta 600F Environmental SEM	FEI / Thermo Fisher		Environmental scanning electron microscope used to support a low-pressure water vapor ambient environment for CNT forest milling
xT Microscope Control software	FEI / Thermo Fisher	4.1.7	Control software used on Quanta 600F ESEM
Nanometer Pattern Generation System - Software	JC Nabity Lithography Systems	Version 9	Software used for electron-beam lithography
Dedicated computer with			Equipment used for electron-beam lithography

PCI516 Lithography board			
DesignCAD software	TurboCAD	V 21.2	Optional equipment used to generate patterns for electron-beam lithography
E-beam lithography mount	Ted Pella	16405	Electron beam lithography mount with a Faraday cup and gold nanoparticles on carbon tape
Picoammeter	Keithley	6485	Used with the Faraday cup to quantify beam current
12.7 mm diameter SEM stub	Ted Pella	16111	SEM stub
45 degree pin stub holder	Ted Pella	15329	Optional equipment used to mill the cross section of a CNT forest

Conclusions

A detailed description of the process to cut carbonaceous materials via an energetic electron beam in a low-pressure water vapor environment is given. Depending on the controlled parameters of the environmental scanning electron microscope, a wide range of milling sizes, materials and rates are possible. This method has demonstrated both cutting of nanoscale features such as individual CNTs and milling of large regions of CNT forests, spanning cubic microns. The electron beam can be software-controlled to raster in simple lines and rectangles, as well as arbitrary and complex shapes. While the technique is relatively clean compared to FIB-based milling, small amounts of carbon residue exists on milled surfaces. Current research is addressing avenues for reducing this residue. Material removal rates were experimentally tested for CNT forests, and are shown to be a function of ESEM parameters (electron energy & flux) and material properties (CNT areal density and alignment). Qualitative trends of material removal rate are expected to hold for all CNT forests but some experimentation may be required to find the optimal parameters for other carbon materials, such as graphene, diamond, and biological tissue.

CHAPTER 5 - TOWARDS CNT FOREST MECHANICAL INTERFACES

Abstract

The mechanical behavior of ultra-dense vertically aligned carbon nanotube micro-pillars is reported. A variety of previously unreported mechanical loading configurations were explored including off-axis compression at a range of angles, cyclic compression/tension, and substrate delamination tests. Morphological evolution during tests acquired with in-situ SEM imaging shows new deformation mechanisms and stress-strain behavior that is different than the widely reported three-region progression of elastic/plateau/densification. Local strain mapping reveals how the principal strain at a buckling site evolves. These results are particularly interesting for applications in mechanical interfaces, where the interface material has several functions: to join rigid body parts together, transmit load, absorb energy, provide flexibility, accommodate changing rigid body geometry, resist vibration damage, among other non-mechanical attributes such as electrical and thermal conduction, optical transmittance, gas permeability, and more. With these complex mechanical loads and material requirements, it is crucial to understand how CNT forests can survive large forces and strains, apart from the widely reported pure axial compression modes of mechanical testing. This understanding will allow CNT forests to be designed for continuous operation mechanical interface applications.

Introduction

Fractal Mechanical Interface Materials

A mechanical interface, often called a suture joint, is a material system composed of rigid bodies joined by a connective layer, and are found in both natural and engineering composites. For many biological sutures, aligned fibrous connective tissue are found along

the suture interface to join several rigid bodies together, transmit load, absorb energy, and provide flexibility to accommodate growth, respiration and locomotion. Biological interfaces must also undergo numerous mechanical cycles of both compressive and tensile loading without fracture. Such interfaces are often jagged and hierarchical in nature to increase surface area between the adjoining surfaces and to efficiently distribute load. Figure 5-1 depicts a fractal structured mechanical interface.

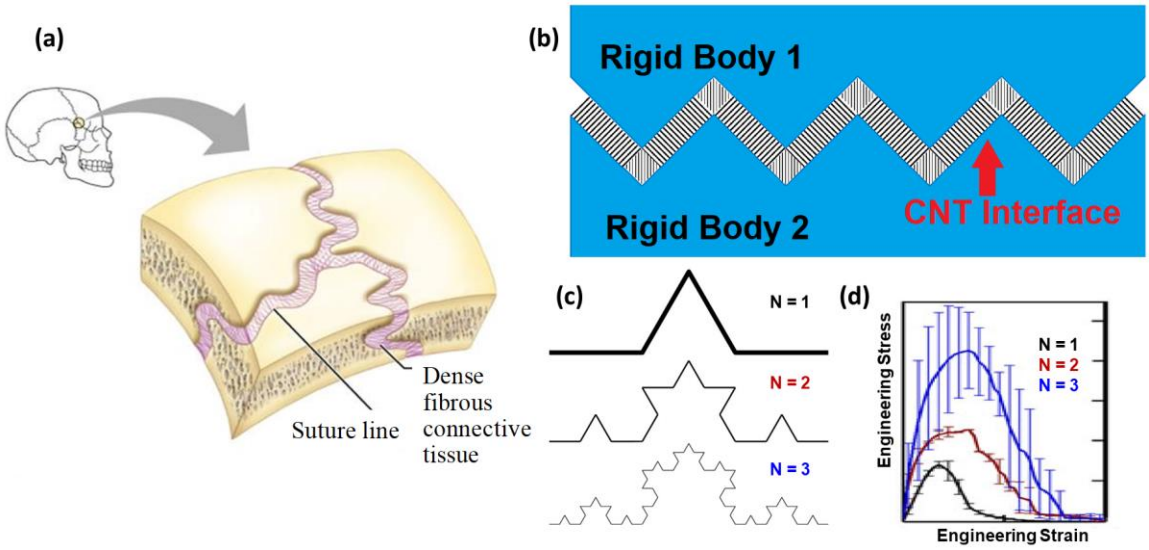

Figure 5-1. Biological inspiration for fractal mechanical interface and effect of fractal order. (a) Human skulls have tortuous suture line cracks which are connected by a dense fibrous connective tissue (b) schematic side-view of the proposed interfacial CNT forest architecture, at fractal order N = 1. (c) Koch curve showing increases fractal orders (d) Mechanical testing of additively manufactured interfaces over three fractal orders. Adapted from [12].

Different from the flat interfaces of standard multi-layered composites, fractal interfaces uniquely dissipate energy in the interfacial layer instead of through the thickness, making the system tougher. The loads are also transmitted more efficiently because of the larger effective cross-sectional area. Therefore, mechanical failure modes are reduced, such as catastrophic separation of layers, vibrational collision damage, and mechanical shock

reflection. Though the fractal geometry improves the effectiveness of the interface, by far the most important consideration in design is the interface material choice.

Viability of CNT forests as a mechanical interface material

The effective design of a mechanical interface requires a material with many special properties and features. The exact application of the interface will dictate which features are most important. Table 5-1 lists properties expected of a mechanical interface material and demonstrates the viability of CNT forests by showing how many desirable properties they possess.

Table 5-1. Mechanical and multi-functional properties required of mechanical interface materials, and the viability of CNT forests

Mechanical Properties	**CNT Forests Capable?**
- Strength to prevent delamination of rigid bodies and prevent collision of the rigid bodies	**Yes**
- Tunable stiffness to allow flexure but prevent	**Yes**
- Toughness to avoid abrupt cracking and fracturing	**Yes**
- Large strain tolerance and recovery, above 50%	**Yes**
- Facilitate simultaneous 3D mechanical loads (axial, transverse)	**?**
- Allow some degree of flexure and twisting	**Yes**
- Strain-rate behavior well understood	**?**
- Frequency-dependent dynamic response well understood	**?**
- Survive many cycles of loading, range of 10^2 - 10^6	**?**
- Strong adhesion to the inner surfaces of the rigid bodies in joint	**?**
Multi-functional Properties	
- Electrical and/or thermal conduction	**Yes**
- Low mass density	**Yes**
- Ability to create patterns, architecture structures	**Yes**
- Efficiently covect and irradiate away the absorbed mechanical energy	**Yes**
- High temperature tolerance	**Yes**
- Defect tolerance	**?**
- Optical attenuation	**Yes**
- Gas permeability	**Yes**
- Hydrophobicity or Hydrophilicity	**Yes**
- Chemical resistance	**Yes**
- Biological compatibility	**?**
- Tunability of all these properties	**Yes**

CNT forests are an excellent candidate material for mechanical interfaces. They mimic the natural fibers found in biological suture interfaces and possess many of the desirable features listed in Table 5-1. Interface conductivity has already been studied and implemented via thermal interfaces. They can be patterned into various shapes and sizes to create architectured structures and functionally coated to exhibit unique and tunable mechanical properties. What stands out in the table is the several unknown mechanical properties of CNT forests relevant to interfaces. The mechanical performance of CNT forests in geometrically complex interfaces with arbitrary loading angle has not been investigated. Neither has the effective delamination strength been reported. Some work has examined multiple load cycles of CNT forests but much more is to be desired. *This work aims to shed light on these three unknown behaviors of CNT forests: combined axial/transverse loading, cyclic loading, and adhesion strength of CNTs to the growth substrate.*

Literature Review – Mechanical Testing of CNT forests and micropillars

The axial mechanical properties of CNT forests and CNT forest micropillars have been thoroughly examined using *in-situ* SEM compression and micro-indentation. Coordinated buckling of CNT forests in response to axial loading is nearly universal[33] and has been observed for forests with heights between several microns to greater than a millimeter. In axial compression, the forest undergoes a 3-region stress-strain behavior: linear elastic, stress plateau, and densification, as shown in Figure 5-2. CNT forests exhibit significant elastic recovery, even after 90% compressive strain but strains of 15% or greater create significant plastic deformation[37]. resilience, deformability, and energy dissipation all increase at faster strain due to inability of individual CNTs in the VACNT matrix to

reconfigure[35]. CNT aerial density and tortuosity represent two key factors governing the overall mechanical response of the CNT forests to local compressive loading[34]. Stiffness of a CNT column is sometimes proportional to its cross-sectional area[41].

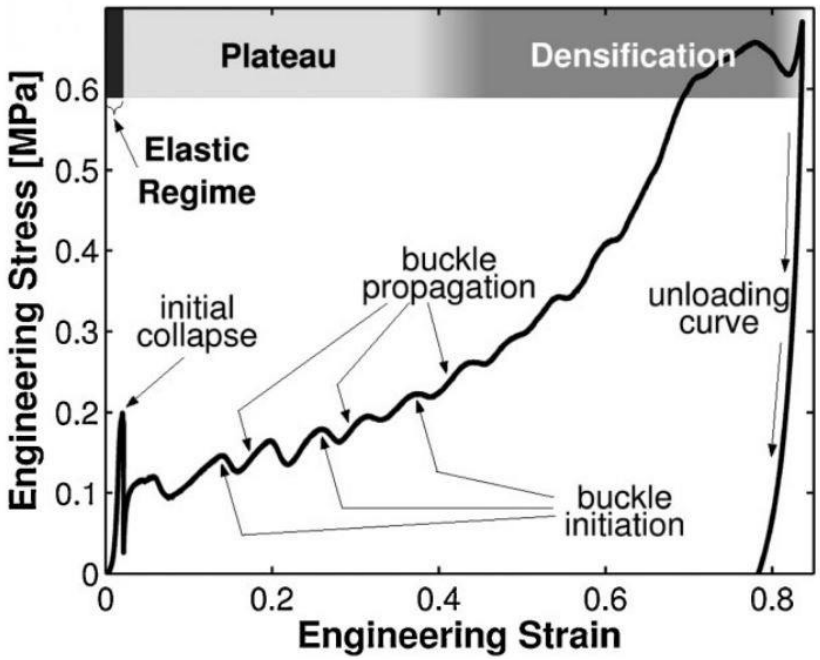

Figure 5-2. Three regions in uniaxial compression of CNT forests: Linear elastic, stress plateau and densification. Adapted from [6].

There is typically a stiffness gradient along the length of the micropillars that arises due to growth kinetics[31]. Like conventional open-cell foam materials, they are capable of absorbing large amounts of mechanical strain energy per unit mass. Their strain behavior is time-dependent due to the formation and breaking of weak van der Waals bonds between CNTs in the forest, often described with the viscoelastic Maxwell model Buckling initiates at ~5% engineering strain along the axial direction, frequently initiating near the bottom (substrate side) of the forest. [123]

Buckling of this type, however, has not been observed when compressing CNT micropillars in the transverse orientation, especially at very high engineering strain.

Instead, transverse compression contributed to increased packing density between neighboring CNTs. The high degree of alignment of CNTs along the axial direction contributes to highly anisotropic mechanical stiffness. Previous reports have found that the simulated and experimental elastic modulus along the axial direction is between 10-100x greater than that in the transverse direction. The material was fully characterized as a transverse isotropic continuum material with five independent elastic constants. The axial compressive modulus exceeds the transverse compressive modulus and out of plane shear modulus by nearly two orders of magnitude. The critical column buckling stress was a strong function of column aspect ratio[29]. The highly anisotropic stiffness and buckling behaviors of CNT forests makes prediction of combined axial and transverse loading a challenge that needs further investigation. Experimental observations of this phenomena have not been reported to date.

The mechanical behavior of cyclically loaded CNT forests is also poorly understood. With the exception of one report[35], the coordinated buckling of compressed CNT forests has resulted in unrecoverable plastic deformation due to interlocking of neighboring CNTs and establishment of numerous CNT-CNT van der Waals interactions. Therefore, CNT forests may require a tensile load to restore them to their original height. The force required to restore a plastically deformed CNT forest to its original height after plastic buckled region has not been explored, nor have the mechanical properties of a CNT forest that has forcefully been recovered to its original height after. Experimentation of this type requires a rigid connection to the top surface of the CNT forest that can apply both compressive and tensile loading. In this work, the free surface of CNT forest micropillars are adhered to an indenter tip using epoxy within a scanning electron microscope. The

cured epoxy is rigid and cures without influencing the CNT forest morphology outside of the bonding area.

CNTs must be able to strongly adhere to a surface on both ends to act as an interface material. After the synthesis process, the forest naturally has some adhesion with the substrate due to catalyst interaction with the support thin film. It is previously unknown what the effective strength of this adhesion is. Buckling driven delamination has been reported at <1 MPa[124], but this strength is expected to be highly dependent on the exact growth process. The top surface of CNTs is free and open and will therefore require post-processing to bond to a rigid body. However, this work focuses on the strength of the substrate side of the forest.

Advances in CNT forest mechanical analysis

In-situ SEM mechanical compression of CNT forests facilitates direct observation of CNT deformation while simultaneously recording force and displacement data. The strength of in-situ testing is the imagery that provides direct evidence of deformation mechanisms. Importantly, the high-contrast grayscale imagery is compatible with digital image correlation (DIC) software to provide quantifiable spatio-temporal deformation and strain during testing. Previous in-situ SEM reports have examined the axial compression behavior of CNT forests synthesized by different techniques, various strain rate application, distributed strain mapping, and comparison between transverse and axial deformation behaviors. Previous tests have applied load only in compression, and mostly along the CNT forest growth axis.

The present work advances CNT forest mechanical analysis towards the goal of complex and biologically inspired interfaces. Conventional nanoindentation and in-situ

SEM compression/tension testing are employed to obtain diverse data sets using CNT forest micropillars. Micropillars are chosen instead of large area forests because they have exposed faces which allow for observation of the deformation mechanisms during testing. A variety of micropillar sizes were explored including both square and circular cross sections, widths ranging from 5-200 μm, and heights all approximately 100 μm. Combined loading (compression and shear) was performed at 0^o, 30^o and 45^o relative to the growth axis. Cyclical loading at high compressive strain was performed by adhering the top surface of CNT pillars to an indentation tip. Delamination loads were obtained in a similar manner for a number of CNT pillar configurations. Finally, CNT pillars were adhered to both the indenter tip and a rigid substrate to further discourage delamination.

Methods

CNT Forest Micro-Pillar Synthesis

CNT forest micropillars were synthesized on (100) silicon wafers coated with 300 nm of thermally grown SiO_2 by patterning Al_2O_3/Fe catalyst layer. The supported catalyst layer, 10 nm of Al_2O_3 and 1 nm of Fe, was sequentially deposited by electron beam evaporation. The patterned substrate was placed in a quartz tube furnace for the CNT growth. The synthesis begins with flowing 100/400 sccm of He/H_2 while ramping the furnace to 775°C, over 10 min, then the temperature was held at 775°C for 10 min with the same gas flow rates to anneal the catalyst film. The gas flow is changed to 100/400/100 sccm of $C_2H_4/He/H_2$ at 775 °C for CNT nucleation and growth for approximately 1 min to produce 100 μm tall pillars. The C_2H_4 flow was extinguished, and the furnace was allowed to cool to 100 °C. A purge of 1000 sccm of He was maintained for 5 min before the samples were retrieved. Figure 5-3 shows the pillars after growth.

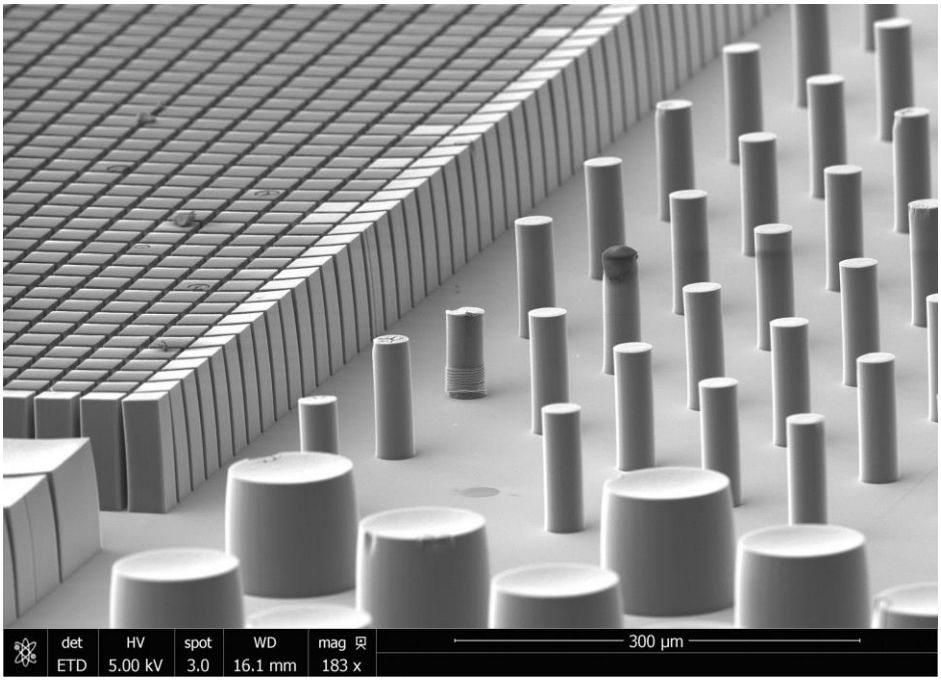

Figure 5-3. CNT Micro-pillar array.

In-situ SEM Mechanical Testing

In-situ mechanical tests were conducted in a FEI Quanta 650F SEM using a test frame (Micro-Test Solutions, LLC) to capture the local microstructural evolution during the course of deformation. The test frame is comprised of a XYZ sample stage for precision positioning, a 10 g load cell and a sub-nanometer resolution piezoelectric actuator to drive the indenter tip. The CNT micropillar samples were mounted to custom stages having an inclined angle of 0 ^{o}, 30 ^{o}, or 45^{o} to match the inclination angle of customized indentation heads.

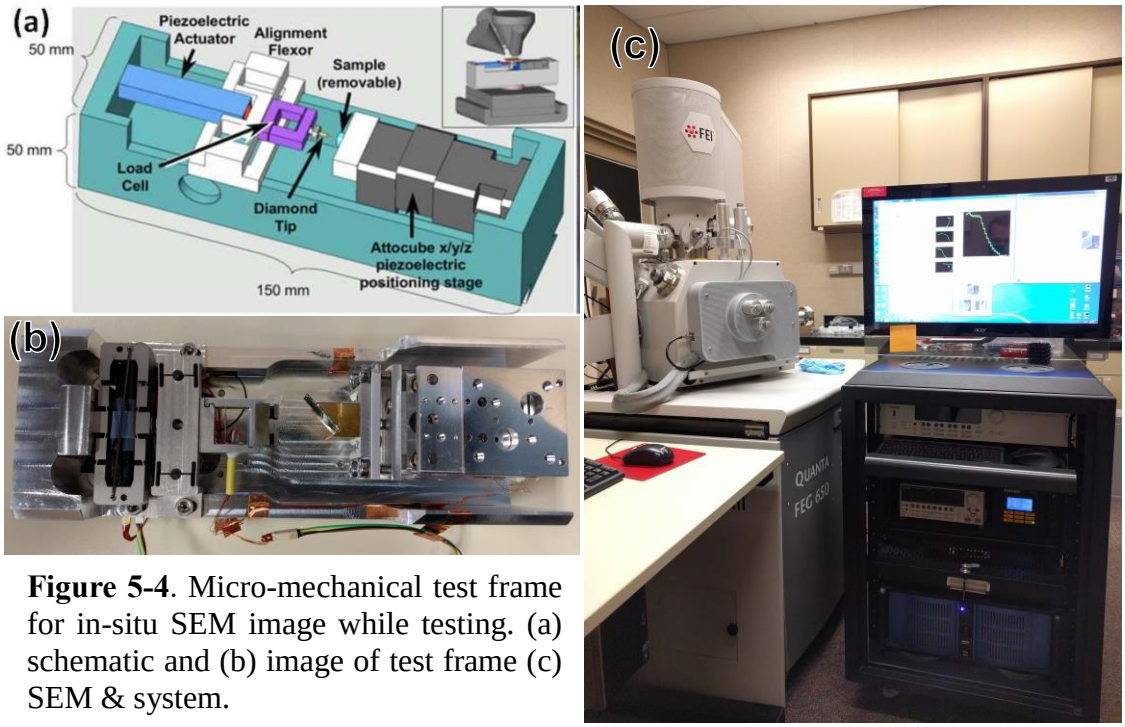

Figure 5-4. Micro-mechanical test frame for in-situ SEM image while testing. (a) schematic and (b) image of test frame (c) SEM & system.

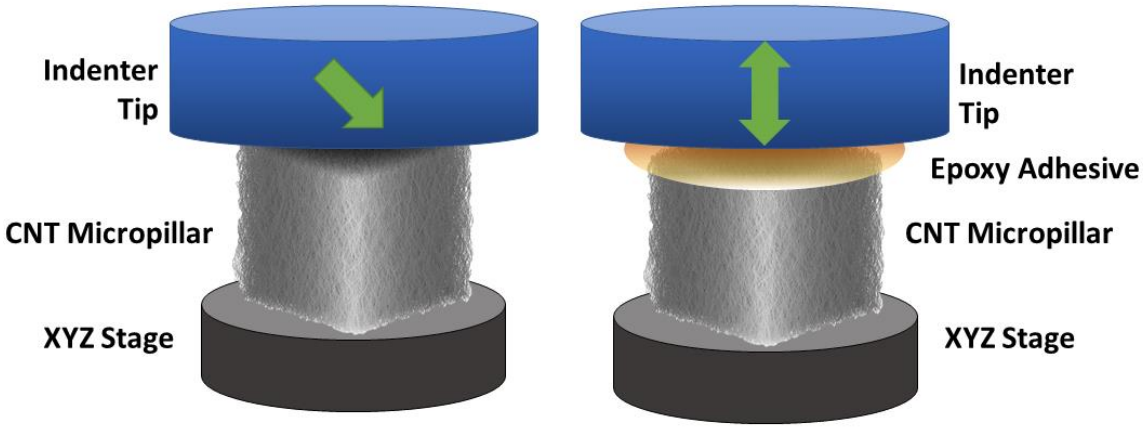

Figure 5-5. Schematic of mechanical tests (a) combined axial and transverse stress imposed on the CNT micropillar (b) pillar top edge adhered to indenter tip for cyclic axial testing.

Indenter heads were comprised of tungsten needle probes that were milled to the appropriate angle using focused ion beam. By angling the contact face of the indenter and the host substrate relative to the actuation stroke of the test frame, combined axial/shear loading configuration were applied. During data acquisition, tip displacement was applied in a step-wise manner, and SEM imaging scans were obtained while the tip was stationary. All data acquisition and experimental control occurred outside of the SEM using LabView software. Because the mechanical load cell of the test frame offers mechanical compliance, actual tip displacement was measured during image post-processing using either ImageJ or VIC-2D software.

Nanoindentation Mechanical Testing

Similar mixed loading data was obtaining using nanoindentation (Agilent G200). Angled compression tips were fabricated by Micro Star Technologies by milling a sapphire indenter tip that was nominally 50 μm in width. Angled sample holders were created by 3D printing to match the inclination angle of the tip. Standard nanoindentation protocols were utilized to apply greater than 50% engineering strain to the CNT micropillars. Multiple loading and unloading cycles were employed to obtain the elastic response of the CNT pillars as a function of strain.

Combined compression and tensile testing was performed on some pillars using the in-situ SEM test frame. For these experiments, a fast-cure 3M two-part epoxy was used. This epoxy was selected after much experimentation because it provided sufficient adhesion to the CNT free tips, conformed to the CNT pillar profile without excess wicking that would otherwise alter the CNT forest morphology, and could be removed from the tip using acetone and mechanical agitation. The epoxy was first mixed and was rapidly applied

to a flat indenter tip. The tip was next installed in the test frame, and the SEM chamber was immediately pumped. The test frame had been previously aligned such that the CNT pillar of interest and the indenter tip were in alignment, thereby reducing the time required to locate and adhere to a pillar of interest after pump down. SEM imaging was commenced immediately after vacuum was sufficient, and liquid epoxy bulb was brought into contact with the free surface of the CNT pillar. Using stage motion, the CNT pillar was pushed at least 2 μm into the epoxy pool to establish adequate contact. Minimal wicking outside of the epoxy contact area was observed. The epoxy was allowed to cure for between 4-12 hours in the vacuum environment to assume full epoxy strength. Mechanical testing then proceeded as normal.

Digital Image Correlation for Spatiotemporal Strain Mapping

Spatiotemporal strain mapping was achieved using VIC-2D software[125]. Here, image sequences were processed and compared to an unstrained image to compute full-field, planar displacements and strains. Optimized correlation algorithms measure pixel-by-pixel displacement and compute strains with tensor operations. DIC parameters used for analysis are: subset size of ~50 pixels, step size of ~10, Gaussian subset weights, optimized 6-tap interpolation, normalized squared differences, low-pass image filtering, exhaustive pixel search, consistency threshold of 0.06, confidence margin of 0.09, and matchability threshold of 0.54. In a similar manner, the height of a CNT pillar could be recorded using a digital extensometer and used to compute engineering strain. The software itself has sub-pixel displacement resolution, and noise generated within the DIC analysis is introduced by SEM scanning artifacts. Spatially resolved mechanics of compressed CNT arrays was first explored in the axial direction [40] and found that strain within the arrays

is distributed non-uniformly and that ε_2 magnitude of approximately 5% local strain is a universal CNT array buckling criterion.

Results

CNT forest micropillars of various cross sections were synthesized to a height of approximately 100 μm. The pillar widths varied between 5-100 μm and featured either square or circular cross sections. For in-situ testing, pillars having a square cross section were most often interrogated such that a flat face was present for DIC post-processing. Individual pillars having widths of 10, 30, and 100 μm were examined for mixed loading experiments, while individual and multiple pillars were used for delamination studies.

Nanoindentation of CNT micropillars

The mechanical behavior of a CNT forest loaded at different angles relative to the long axis were first examined using nanoindentation. As observed in Figure 5-6, the effect of orienting the sample and tip relative to the loading direction is such that combined compressive and shear loading is imparted at the free end of the pillars. The force recorded by the nanoindenter is oriented only in the direction of the indenter tip travel. 10 tests were conducted for each angle, for statistical purposes. In each test, the force is controlled, increasing displacement until a force target is reached, then unloaded to 10% of the target force. The force targets are 1.25, 2.5, 5.0, 10.0 and 20.0 mN. From Figure 5-6a, a dramatic change is observed in the deformation behavior as the angle of compression increases to 45°. Stiffness decreases and buckling strength decreases at higher compressive angles. This is due to the stiffness in the transverse direction being much lower than in the axial direction. The interstitial void space collapses while transversely compressing, so a much larger indent depth is required to reach the same force. These nanoindentation test motivate

a new type of test which can observe the mechanism as it is happening. Hence, the in-situ SEM tests were conducted.

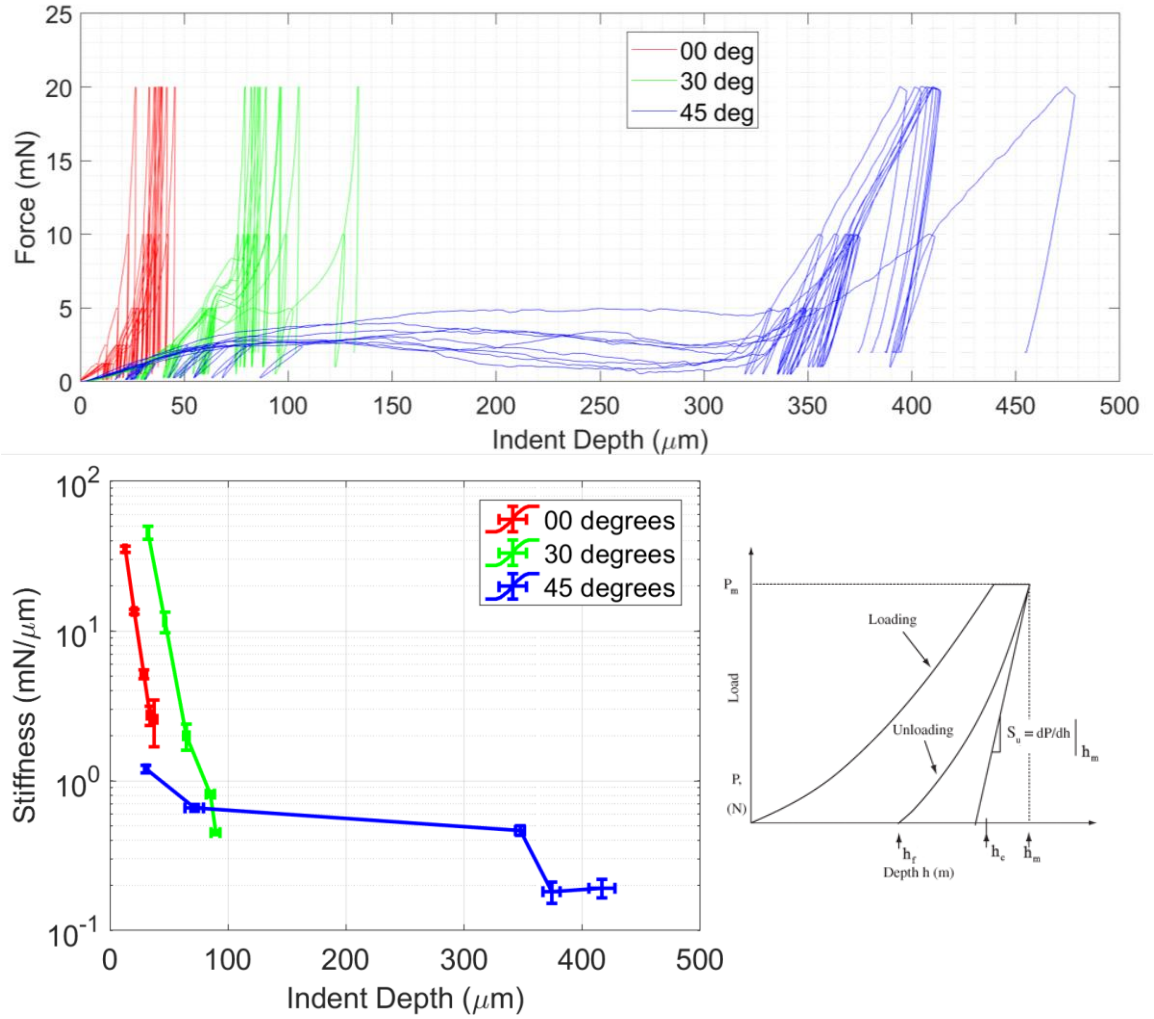

Figure 5-6. Nanoindentation data of a ~500 μm CNT forest. (a) Force vs Indent Depth, showing three different angles of compression. (b) Stiffness as a function of Indent Depth, calculated from the unloading curve of each load cycle, as described in (c).

Combined Axial / Transverse Load Behavior

To investigate the effects of combined axial and transverse stress on aligned CNT populations, an array of about 20 tests was completed, with multiple angles, pillar sizes and indent depths. This gave information on size effects, as well as the deformation behavior. In these studies, the engineering strain is reported as the indenter displacement

times the cosine of the orientation angle (the vertical component of the displacement stroke) divided by the original pillar height. Figure 5-7 shows all stress-strain data from this work. General trends are initially unclear for several reasons. CNT micropillar width has a large influence on behavior. Very high aspect ratio pillars (Length/width >> 1), behave like beams and bend over more so than follow continuous buckle formation and propagation. The compressive load was simultaneously measured during the compression tests. Despite the large differences in deformation behavior, the stress-strain behavior shows some significant and unanticipated similarities. All curves demonstrate characteristics of open-cell foam materials. Initial loading is represented by a linear-elastic regime followed by a nearly horizontal plateau region in which significant mechanical energy is absorbed. Densification the CNT forest structure results in a rapid rise in stress-strain slope, representing an increased stiffness. While the compressive strength of the CNT forests (peak stress before plateau) varies between 1-2 MPa, the plateau stress for all CNT configurations is approximately 1 MPa, with a weak trend of decreasing plateau stress as the orientation angle increases. *If these data trends are applied to the envisioned fractal interface, having many-faceted sides, the mechanical behavior of CNT forest has only a weak correlation with stress orientation.*

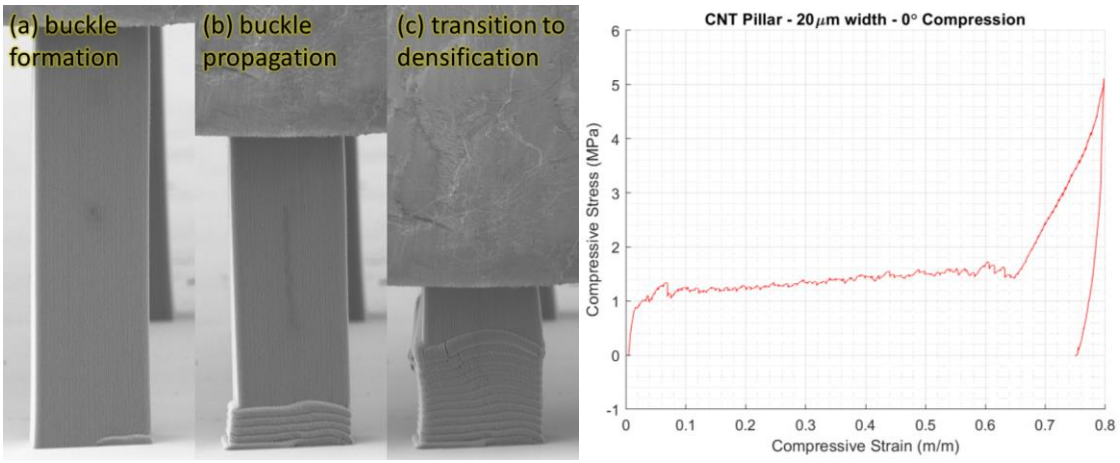

Figure 5-7. In-situ SEM axial compression of a CNT forest micro-pillar (30 μm wide x 120 μm tall) showing sequential accordion-style buckling at the bottom surface, similar to previous reports of the three-region, elastic – plateau – densification.

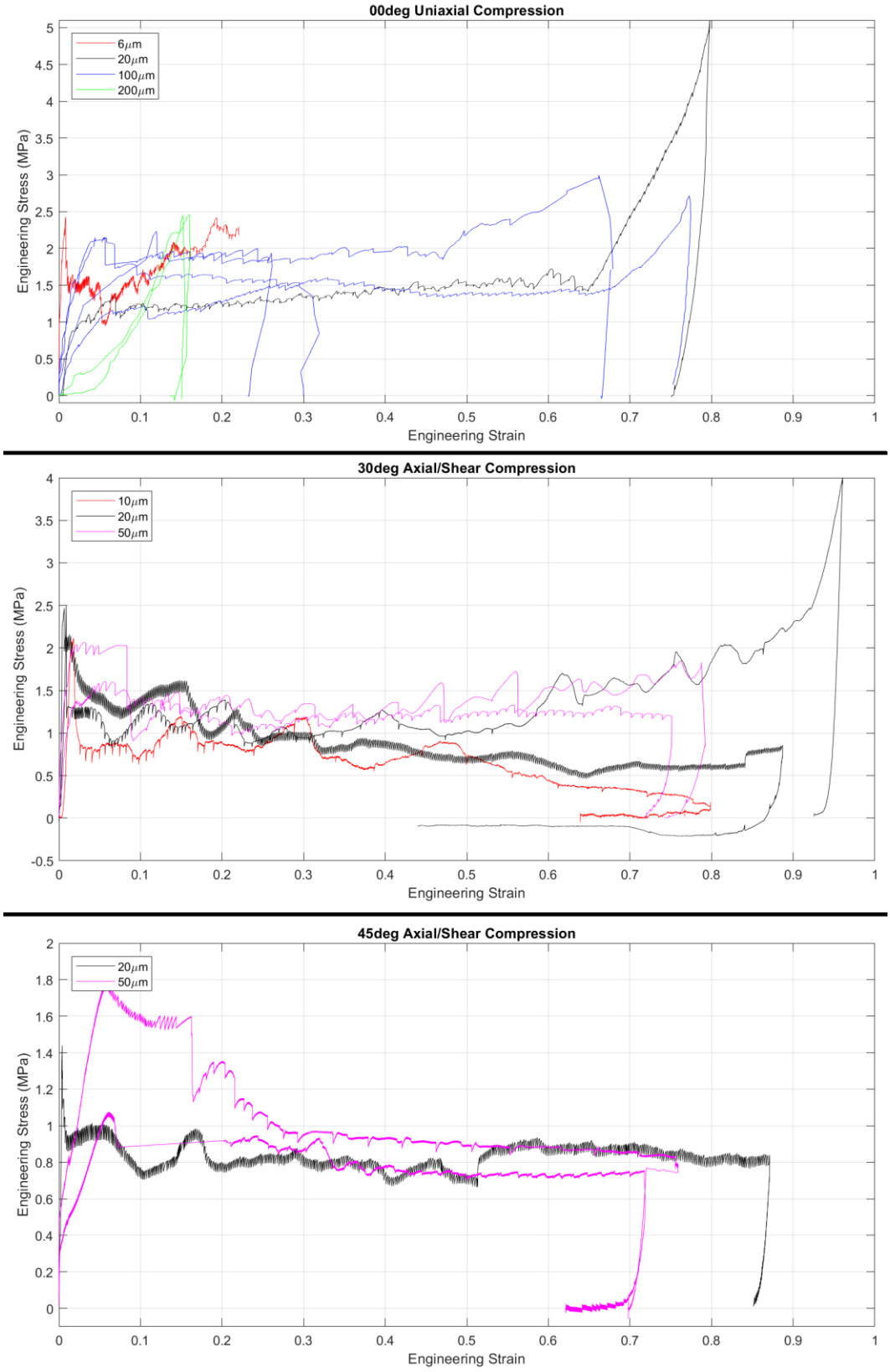

Figure 5-8. Stress-Strain curves for all in situ SEM mechanical test data.

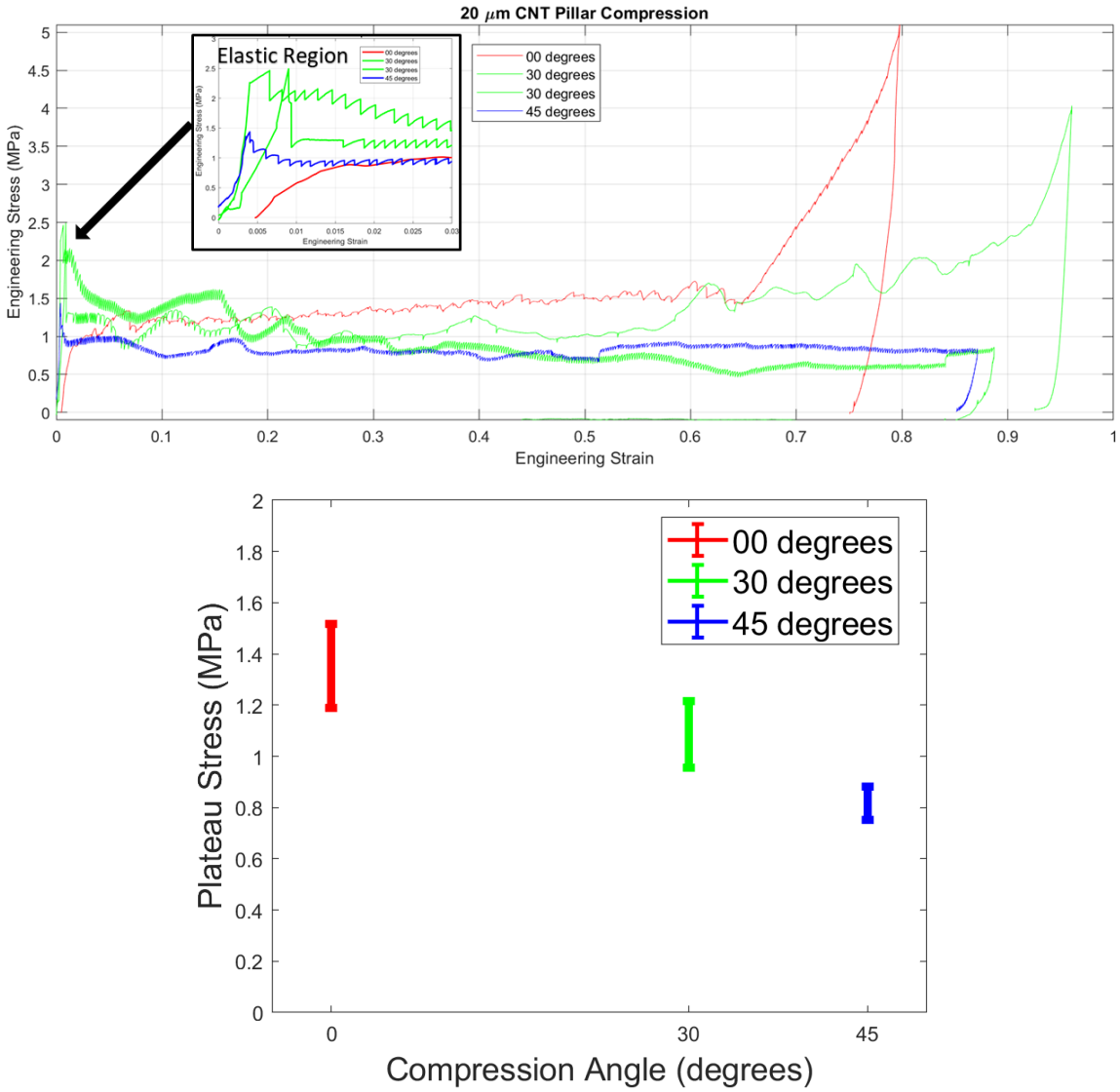

Figure 5-9. (a) Stress-Strain curves 20 μm width CNT pillars showing an extended plateau stress for three compression angles. The densification region gradually decreases and disappears with increasing angle. Inset image shows initial linear elastic region, before buckling initiates. (b) Plateau stress as a function of compression angle, demonstrating a weak correlation. As transverse stresses become more dominant buckles are more easily formed.

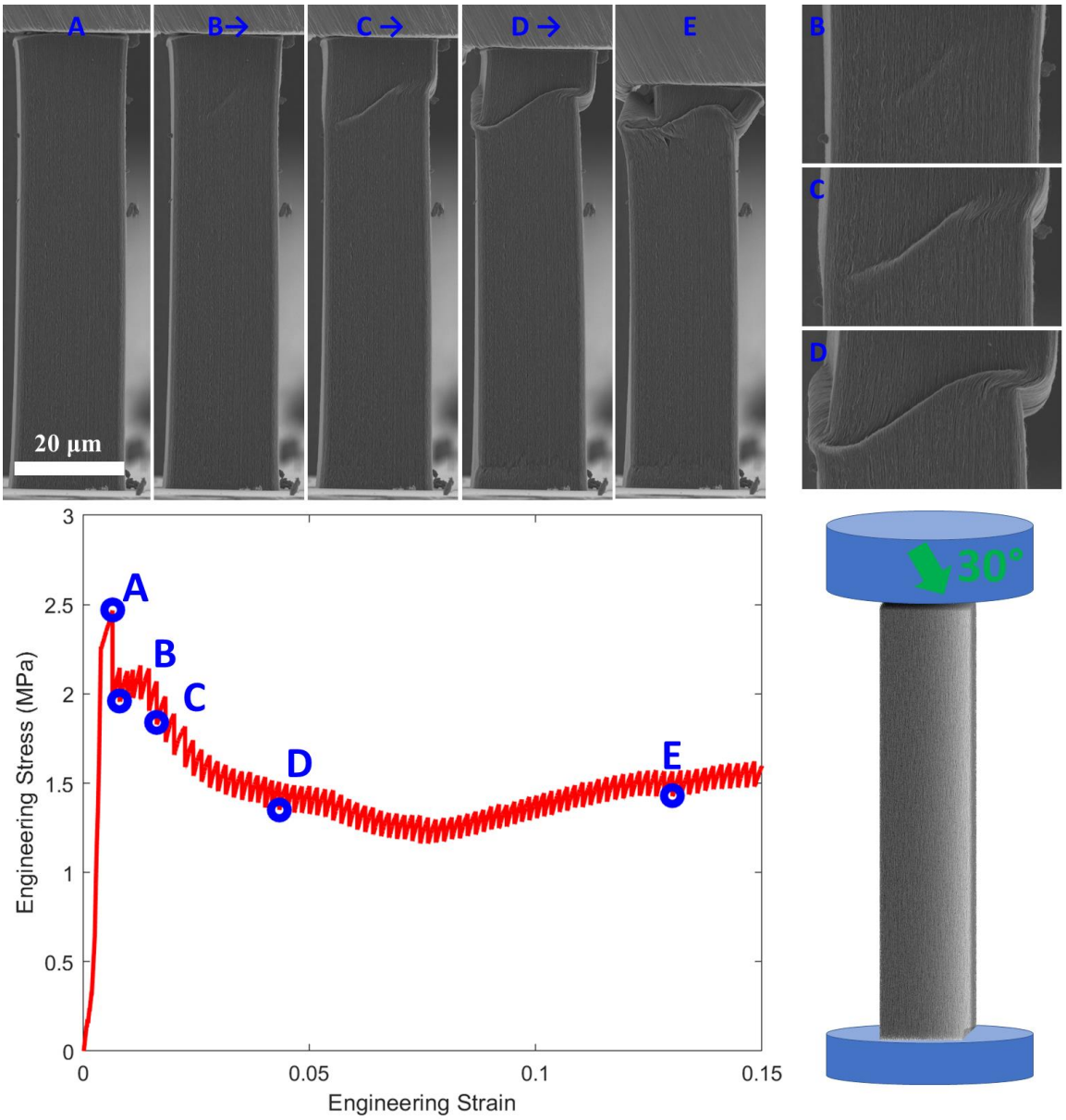

Figure 5-10. Formation & progression of buckles for angled compression shows new deformation mechanisms, i.e. the created of shear planes normal to the axis of compression.

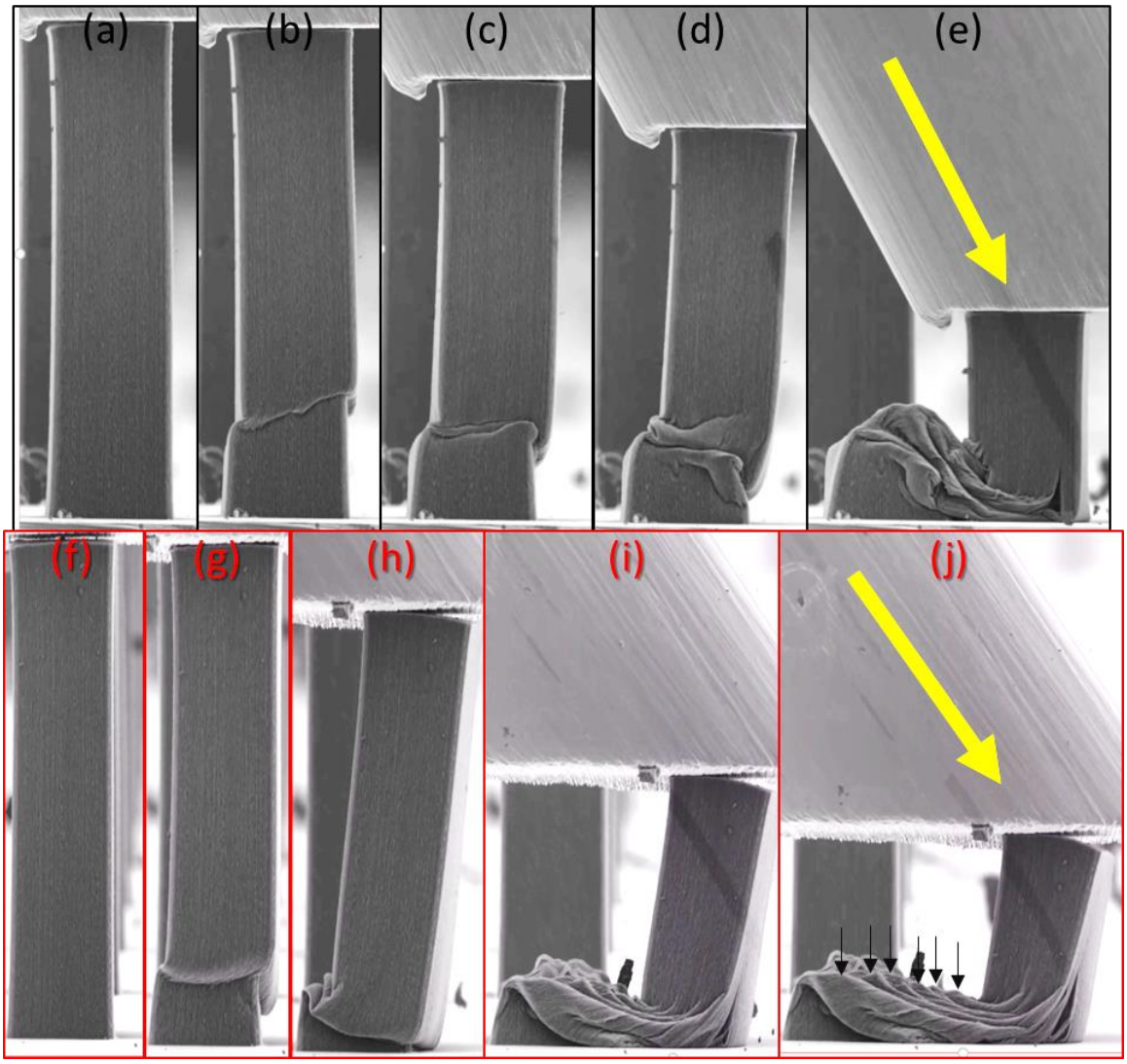

Figure 5-11. In-situ SEM off-axis compression of a CNT forest micropillars (30 µm wide x 120 µm tall). Frames a-e represent a 30° loading orientation while frames f-j represent a 45° loading direction. A shear band first forms near the bottom surface (b and g) which then buckles and curls in the direction of loading (c-d and g-h). Further loading compresses the remaining vertical portion of the pillar against the substrate while period buckling still occurs. Coordinated buckling events occur at regular intervals, as denoted by the arrows in (j).

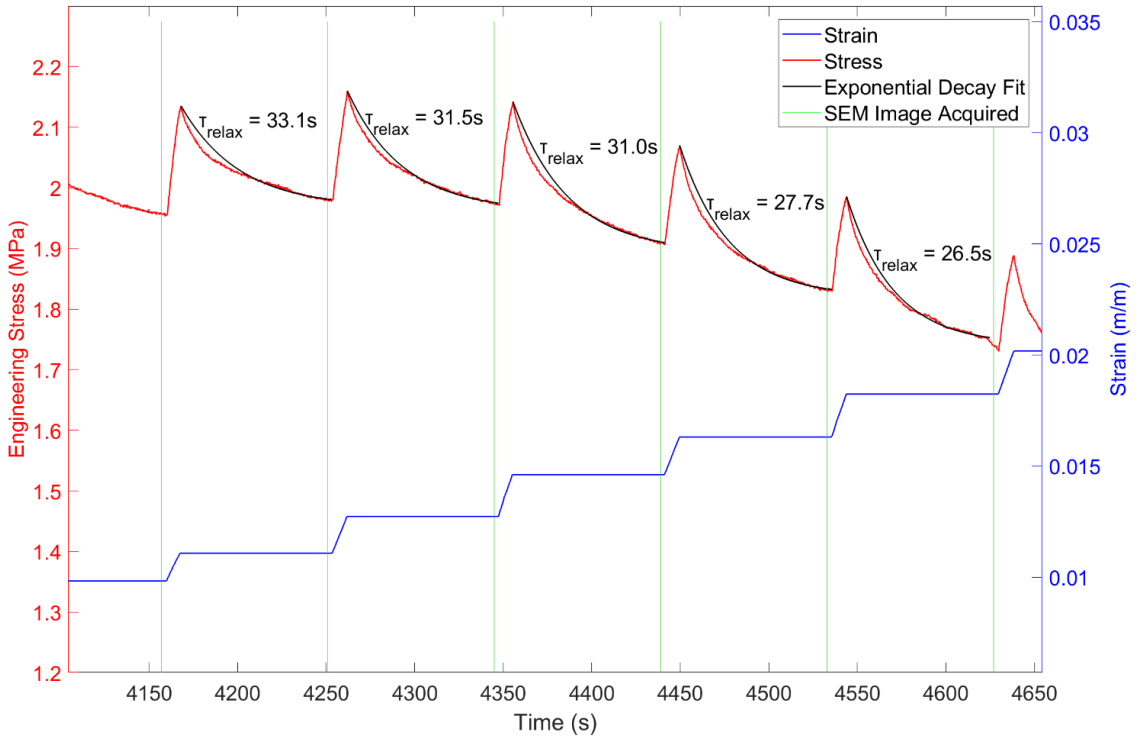

Figure 5-12. Stress relaxation due to SEM imaging of CNT pillars showing viscoelastic response. Stress increases while indenter head is traveling (increasing compressive strain in material), then decreases while indenter head is held fixed and SEM image is acquired.

During in situ testing, strain is applied incrementally rather than continuously due to the periodic SEM image acquisition which requires minimal movement for better clarity and focus. This induces time-dependent stress relaxation behavior in the CNT micropillars. The stress on the micropillar quickly spikes as the strain is applied, and then decreases exponentially with a time constant of approximately $\tau_{relax} = 30$ seconds. This was observed in both compression and tension, as well as during unloading; a plot of these time-dependent responses is shown in Figure 5-12. The time span between strain steps typically ranged between 10 and 50 seconds, during which the SEM image was acquired, and the next strain step applied, for all orientations.

Spatiotemporal strain mapping

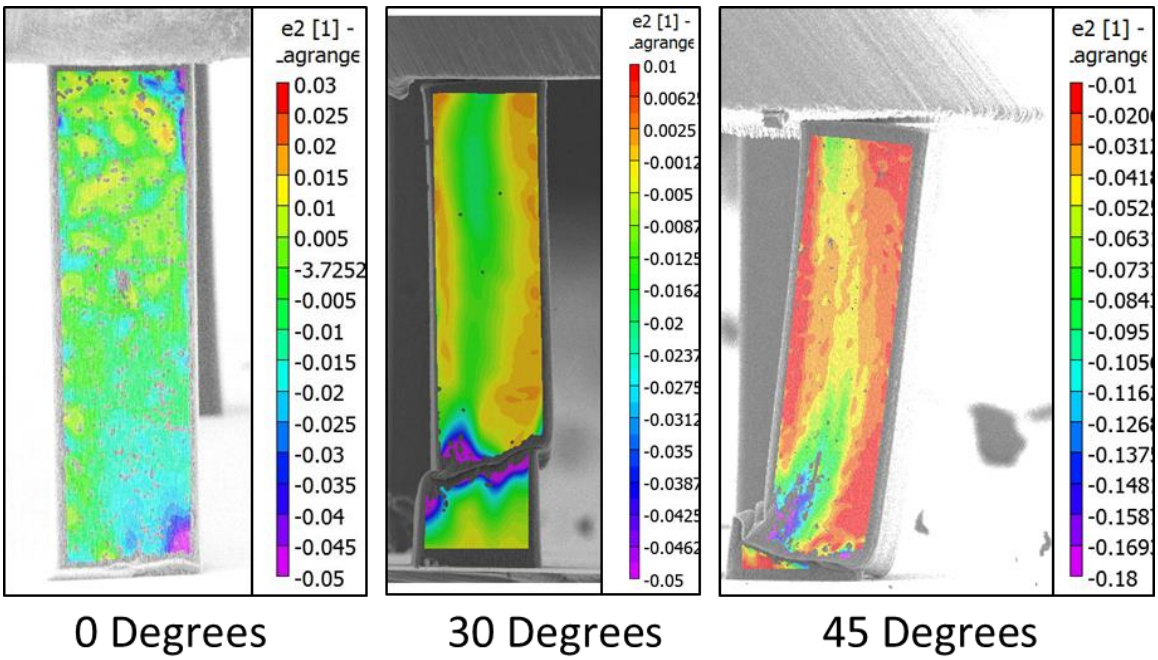

Figure 5-13. Digital image correlation analysis of second principal strain, ε_2, after buckling has initiated, for three angles of compression.

In a manner described in detail in previous work[40], spatial mapping of strain fields within deformed micropillars is achieved via digital image correlation (DIC). Full-field displacement and strain maps are generated based upon the motion of the constituent CNTs, which serve as a traceable high-contrast speckle pattern for DIC analysis. In the current study, the 5% criteria was approximately recreated for the axial case. Buckling in axial compression is oriented normal to the growth axis, which exhibits the most resistance to compressive strain. Above the buckled region, the pillar exhibits nearly neutral strain.

The strain pattern for pillars loaded off-axis exhibited more complex behavior, with principle strain often exceeding 5% compression before the onset of buckling. When loading at 30° relative to the CNT growth axis, the local compressive strain upon formation initial buckle was only slightly greater than 5% (middle panel). At 45° loading, however, the local compressive stress near the buckling region was in excess of 15%. For both the

30 and 45° loading orientations, a band of compressive stress extended from the buckled region to the top of the pillar. This mechanism of CNT deformation has not been observed during axial compression. The orientation of the strain band is hypothesized to be related to the increased strain prior to buckling. The strain band orientation approaches 45° when the pillar is loaded at 45° off axis. In this regime, mechanical resistance is a combination of axial and transverse compression. Previous in-situ SEM studies have shown that transverse compression does not exhibit coordinated buckling, even at strain exceeding 20%. When transverse loading is intermixed with axial loading, it is reasonable to assume that increased strain may be accommodated within the CNT forest before buckle initiation.

Cyclic Tension and Compression Loading

To ensure full mechanical recovery of compressed CNT forest micro-pillars, the top surfaces of pillars were adhered to the flat surface of an indenter tip. For these tests, in-situ SEM is required in order to precisely align the CNT microstructures to the tip without applying unwanted compression to the CNTs. Numerous dry and wet adhesives were investigated for this application. A commercially available quick-set epoxy applied directly to the indenter tip worked well for the task. The epoxy was conformable with low viscosity for several minutes to facilitate easy mating between the indenter tip and the top surface of the CNTs. Further, the epoxy did not wick appreciably into the CNT forest structure, leading to minimal disruption to the natural CNT forest morphology. The epoxy was allowed to cure for no less than two hours prior to experimentation.

Combined compression-tension experiments were performed on CNT pillars in the axial orientation, shown in Figure 5-14. CNT pillars were first compressed and then returned to their neutral starting height by applying a tensile load. The first compression

stroke produced the typical accordion-style buckles near the base of the pillar. Upon completion of the compressive stroke, the tip translated in the opposite direction, pulling the top surface of the CNT pillar. A negligible negative (tensile) force is required to return the pillar to its original height for the first mechanical cycle. During unloading, individual CNT buckles unfold and return to a nearly straight configuration. This behavior is not observed for pure compression tests. The buckles were largely removed during unloading, although residual folds were observed even at full extension.

During the first compressive cycle, the force-displacement behavior of the CNT pillar behaved like an open-cell foam, as seen in Figure 5-14b. The force oscillations observed during compression indicate the forming of numerous buckles near the base of the pillar. The second compressive cycle produced a CNT morphology that was markedly different from the first. The previously buckled region appears softened and bulges out upon compression, acting like a bellows. Correspondingly, the compressive force required to compress the pillar is reduced by a factor of 5 for the first 40 μm of compression. As the top end of the previously softened region begins to encounter the rigid silicon substrate, the force rapidly increases. Significantly more tensile stress of as high as 2 MPa is required to return the pillar to its original height.

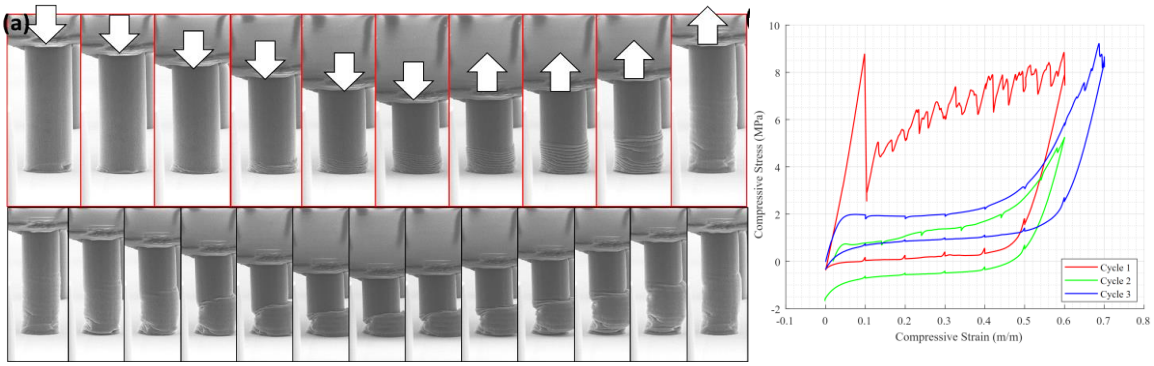

Figure 5-14. In-situ SEM compression and recovery of a 30 μm diameter CNT forest micro-pillar using adhesive on the top compression platen. The CNT forest pillar morphology for the first test (top) is different than that of the second text (bottom). The force vs. displacement of a CNT forest pillar for the first (red), second (green), and third (blue) compression cycles.

Additional mechanical cycling of the pillar shown in Figure 5-14 resulted in unintentional delamination from the growth substrate. This clearly presents an important challenge that may limit the adoption of CNT forests for mechanical interface applications. As a result, a significant focus transitioned to quantifying CNT forest delamination stress, as described in the next section. However, another test was completed by bonding both ends of the CNT pillar to a fixed plate, in order to observe the deformation behavior and disregard the possible delamination, shown in Figure 5-15.

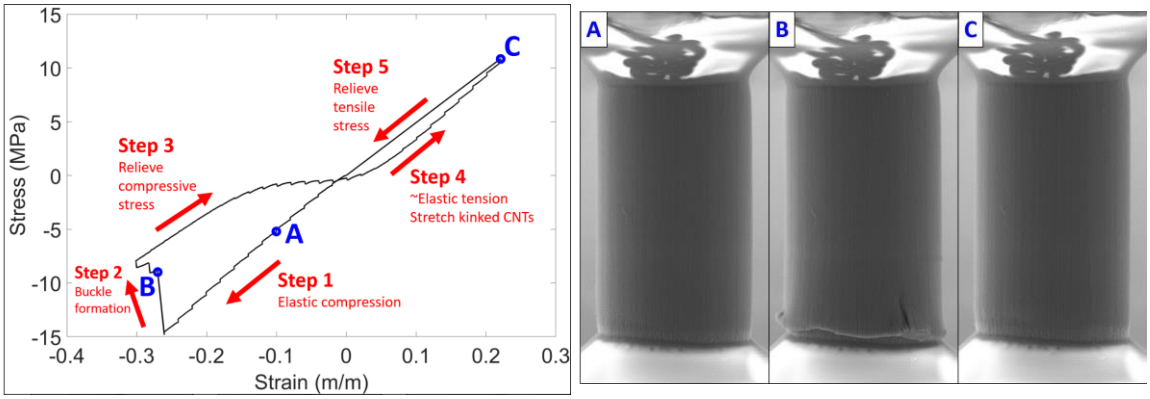

Figure 5-15. Formation and relief of a buckle during full compression/tension cycle. Both top and bottom surfaces are adhered to rigid mounts, to discourage delamination.

This test produced several interesting behaviors. Before buckling, elastic modulus is consistently about ~50 MPa in both compression and tension. Elastic modulus gradually decreases to ~20 MPa while buckles are accumulating but recovers after stretching back out. Buckling strength decreases by 66% after initial buckle event, another 20% after 2nd buckle. Buckling stress is much higher than other tests, presumably due to fixed end conditions and smaller aspect ratio, similar to Euler's buckling condition.

CNT Pillar Delamination from Growth Substrate

Using the same epoxy as previously described, Figure 5-16a shows 3 CNT pillars after simultaneous removal from their growth substrate. Each CNT pillar featured a square cross section of 100 x 100 μm. The epoxy directly above the liberated pillars was buckled due to inadequate epoxy curing. Although the epoxy was viscoelastic during delamination, the resulting force required to delaminate the CNT forests micro-pillars was not affected. The stress-time plot shown in Figure 5-16c indicates that tension was increased at discrete steps. Tensile force is added incrementally until a sudden drop in stress is observed at 3 MPa representing delamination. The stress considers the composite area from all three CNT micro-pillars. It is unknown if all three pillars simultaneously delaminated or if a sequential and cascading delaminating occurred because of the rapid speed of the delamination. Additional delamination tests were conducting on individual CNT pillars. From these subsequent tests, delamination stresses of 7.9 MPa, 14.2 MPa, 4.0 MPa, and 1.4 MPa were observed. The latter 2 tests showed indications of pre-stress near the bottom of the pillar that may have initiated premature delamination. Nevertheless, an average magnitude of approximately 7 MPa delamination stress was obtained from this set of experiments, assuming a solid cross-section.

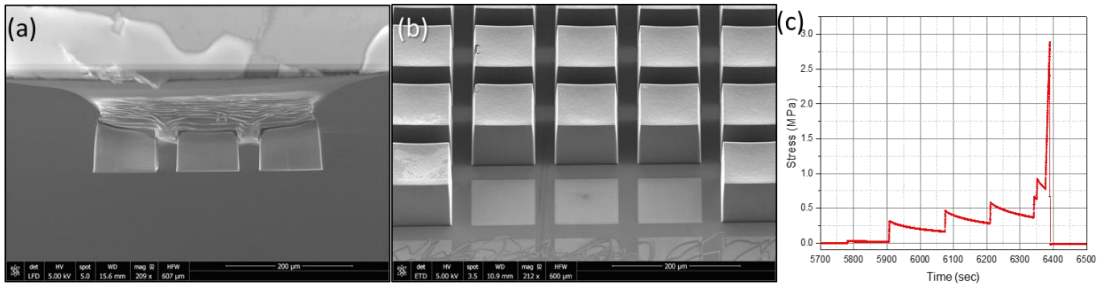

Figure 5-16. SEM images show (a) 3 CNT forest micropillars (each 100 x 100 μm) removed from (b) their host silicon growth substrate. (c) The stress required to remove the pillars approached 3 MPa.

The average force exerted on individual CNTs can be approximated from the delamination stress. Assuming an areal density of approximately 5%, and an average outer diameter of 10 nm, the average load per CNT is estimated at 11 nN. Further assume an inner diameter of 8 nm, the delamination stress between a single CNT is approximately 390 MPa. Closer investigation of the delamination region, shown in Figure5-17b, shows what appears to be numerous pits with diameters on the order of ~10 nm, suggesting that CNTs and their catalyst particles were lifted from the growth substrate. Some CNTs remain, however, suggesting that they either failed in tension or, more likely, were sufficiently short that they were not well entangled within the bulk forest. Nevertheless, this data represents a valuable reference against which CNT interfaces may be designed. Further mechanisms to enhance adhesion strength could further enhance their resistance to delamination under modest loading.

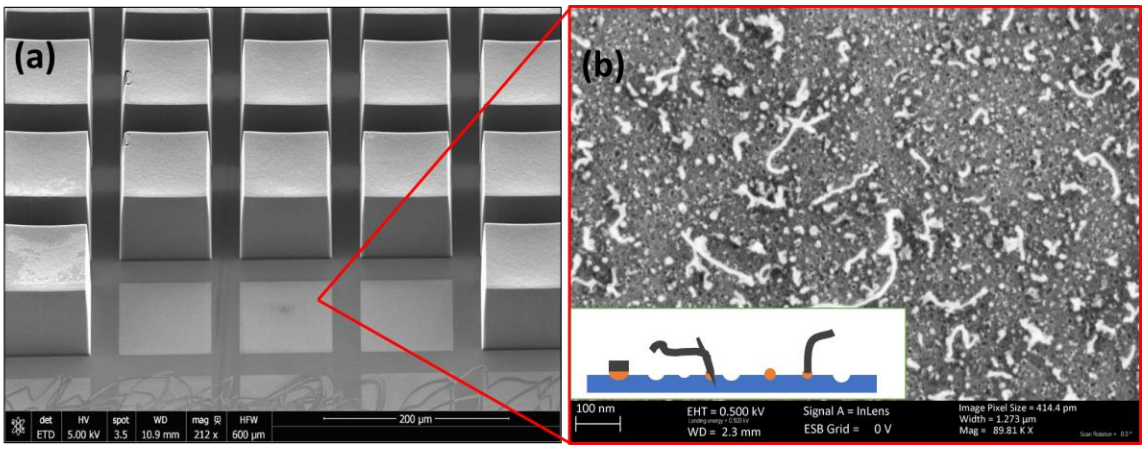

Figure 5-17. SEM micrographs showing (a) the region in which CNT forest micropillars were delaminated from their growth substrate and (b) high-magnification of the delamination surface showing both dark pits and residual short CNTs.

Conclusions

The mechanical behavior of ultra-dense vertically aligned carbon nanotube micro-pillars is reported. A variety of previously unreported mechanical loading configurations were explored including off-axis compression at a range of angles, cyclic compression/tension, and substrate delamination tests. Morphological evolution during tests acquired with in-situ SEM imaging shows new deformation mechanisms and stress-strain behavior that is different than the widely reported three-region progression of elastic/plateau/densification. Mechanical behavior of CNT forests fractal interfaces is found to have only a weak correlation to the stress orientation in relation to the CNT axis. In cyclic loading, the elastic modulus is found to recover to the same value as a pristine pillar after tension is applied to recover all strain. Delamination stress is found to be around 7 MPa for a CNT pillar, or ~10nN per individual CNT. Local strain mapping reveals how the principal strain at a buckling site evolves. These results are particularly interesting for applications in mechanical interfaces, where the interface material has several functions: to join rigid body parts together, transmit load, absorb energy, provide flexibility,

accommodate changing rigid body geometry, resist vibration damage, among other non-mechanical attributes such as electrical and thermal conduction, optical transmittance, gas permeability, and more. With these complex mechanical loads and material requirements, it is crucial to understand how CNT forests can survive large forces and strains, apart from the widely reported pure axial compression modes of mechanical testing. This understanding will allow CNT forests to be designed for continuous operation mechanical interface applications.

REFERENCES

1. Botkin, D.B., *Environmental science : earth as a living planet*. 2014, Hoboken, NJ: John Wiley.
2. Poncharal, P., et al., *Electrostatic Deflections and Electromechanical Resonances of Carbon Nanotubes.* Science, 1999. **283**(5407): p. 1513.
3. Kumar, M., *Carbon Nanotube Synthesis and Growth Mechanism.* IntechOpen, 2011.
4. De Volder, M.F.L., et al., *Carbon Nanotubes: Present and Future Commercial Applications.* Science, 2013. **339**(6119): p. 535-539.
5. Stein, I.Y., D.J. Lewis, and B.L. Wardle, *Aligned carbon nanotube array stiffness from stochastic three-dimensional morphology.* Nanoscale, 2015. **7**(46): p. 19426-19431.
6. Hutchens, S.B., L.J. Hall, and J.R. Greer, *In situ Mechanical Testing Reveals Periodic Buckle Nucleation and Propagation in Carbon Nanotube Bundles.* Advanced Functional Materials, 2010. **20**(14): p. 2338-2346.
7. Pouillon, Y., et al., *Gas Sensing and Thermal Transport Through Carbon-Nanotube-Based Nanodevices*, in *Design and Applications of Nanomaterials for Sensors*, J.M. Seminario, Editor. 2014, Springer Netherlands: Dordrecht. p. 99-136.
8. Chowdhury, S.C., et al., *Molecular simulations of pristine and defective carbon nanotubes under monotonic and combined loading.* Computational Materials Science, 2012. **65**(Supplement C): p. 133-143.
9. Rajabifar, B., et al., *Three-dimensional machining of carbon nanotube forests using water-assisted scanning electron microscope processing.* Applied Physics Letters, 2015. **107**(14): p. 143102.
10. Han, J.-H., et al., *A Mechanochemical Model of Growth Termination in Vertical Carbon Nanotube Forests.* ACS Nano, 2008. **2**(1): p. 53-60.
11. Terrones, M., et al., *Graphene and graphite nanoribbons: Morphology, properties, synthesis, defects and applications.* Nano Today, 2010. **5**(4): p. 351-372.
12. Lin, E., et al., *Tunability and enhancement of mechanical behavior with additively manufactured bio-inspired hierarchical suture interfaces.* Journal of Materials Research, 2014. **29**(17): p. 1867-1875.
13. Iijima, S., *Helical microtubules of graphitic carbon.* Nature, 1991. **354**(6348): p. 56-58.
14. Smalley, R.E., *Discovering the Fullerenes*, in *Rice Quantum Institute*. 1996: Houston, TX. p. 89-103.
15. Xu, J. and T.S. Fisher, *Enhancement of thermal interface materials with carbon nanotube arrays.* International Journal of Heat and Mass Transfer, 2006. **49**(9-10): p. 1658-1666.
16. Cola, B.A., X. Xu, and T.S. Fisher, *Increased real contact in thermal interfaces: A carbon nanotube/foil material.* Applied Physics Letters, 2007. **90**(9): p. 093513.
17. Cola, B.A., et al., *Photoacoustic characterization of carbon nanotube array thermal interfaces.* Journal of Applied Physics, 2007. **101**(5): p. 054313.
18. Yokoyama, D., et al., *Low temperature grown carbon nanotube interconnects using inner shells by chemical mechanical polishing.* Applied Physics Letters, 2007. **91**(26): p. 263101.
19. Myounggu, P., et al., *Effects of a carbon nanotube layer on electrical contact resistance between copper substrates.* Nanotechnology, 2006. **17**(9): p. 2294.
20. Maschmann, M.R., et al., *Bioinspired Carbon Nanotube Fuzzy Fiber Hair Sensor for Air-Flow Detection.* Advanced Materials, 2014. **26**(20): p. 3230-3234.

21. Maschmann, M.R., et al., *Force sensitive carbon nanotube arrays for biologically inspired airflow sensing.* Smart Materials and Structures, 2012. **21**(9): p. 094024.
22. Yamada, T., et al., *A stretchable carbon nanotube strain sensor for human-motion detection.* Nat Nano, 2011. **6**(5): p. 296-301.
23. Sharma, A., et al., *A carbon nanotube optical rectenna.* Nature Nanotechnology, 2015. **10**: p. 1027.
24. Choi, W., et al., *Chemically driven carbon-nanotube-guided thermopower waves.* Nature Materials, 2010. **9**: p. 423.
25. Lee, S.W., et al., *High-power lithium batteries from functionalized carbon-nanotube electrodes.* Nature Nanotechnology, 2010. **5**: p. 531.
26. Cui, X., et al., *Rechargeable Batteries with High Energy Storage Activated by In-situ Induced Fluorination of Carbon Nanotube Cathode.* Scientific Reports, 2014. **4**: p. 5310.
27. Ball, P., *None more black.* Nature Materials, 2016. **15**: p. 500.
28. Jourdain, V. and C. Bichara, *Current understanding of the growth of carbon nanotubes in catalytic chemical vapour deposition.* Carbon, 2013. **58**: p. 2-39.
29. Maschmann, M.R., et al., *Continuum analysis of carbon nanotube array buckling enabled by anisotropic elastic measurements and modeling.* Carbon, 2014. **66**(0): p. 377-386.
30. Ge, L., et al., *Cooperative Adhesion and Friction of Compliant Nanohairs.* Nano Letters, 2010. **10**(11): p. 4509-4513.
31. Deck, C.P., et al., *Mechanical behavior of ultralong multiwalled carbon nanotube mats.* Journal of Applied Physics, 2007. **101**(2): p. 23512-1.
32. Cao, C., et al., *Buckling initiation and displacement dependence in compression of vertically aligned carbon nanotube arrays.* Carbon, 2011. **49**(10): p. 3190-3199.
33. Zbib, A.A., et al., *The coordinated buckling of carbon nanotube turfs under uniform compression.* Nanotechnology, 2008. **19**(17): p. 175704.
34. Pour Shahid Saeed Abadi, P., et al., *Effects of morphology on the micro-compression response of carbon nanotube forests.* Nanoscale, 2012. **4**(11): p. 3373-3380.
35. Pathak, S., et al., *Higher Recovery and Better Energy Dissipation at Faster Strain Rates in Carbon Nanotube Bundles: An in-Situ Study.* ACS Nano, 2012.
36. Gao, Y., et al., *Impact of nanotube density and alignment on the elastic modulus near the top and base surfaces of aligned multi-walled carbon nanotube films.* Carbon, 2012. **50**(10): p. 3789-3798.
37. Maschmann, M.R., et al., *In situ SEM Observation of Column-like and Foam-like CNT Array Nanoindentation.* ACS Applied Materials & Interfaces, 2011. **3**(3): p. 648-653.
38. Maschmann, M.R., et al., *Length dependent foam-like mechanical response of axially indented vertically oriented carbon nanotube arrays.* Carbon, 2011. **49**(2): p. 386-397.
39. Cao, A., et al., *Super-compressible foamlike carbon nanotube films.* Science, 2005. **310**(5752): p. 1307-13.
40. Maschmann, M.R., et al., *Visualizing Strain Evolution and Coordinated Buckling within CNT Arrays by In Situ Digital Image Correlation.* Advanced Functional Materials, 2012. **22**(22): p. 4686-4695.
41. Yaglioglu, O., et al., *Wide Range Control of Microstructure and Mechanical Properties of Carbon Nanotube Forests: A Comparison Between Fixed and Floating Catalyst CVD Techniques.* Advanced Functional Materials, 2012. **22**(23): p. 5028-5037.

42. Bedewy, M., et al., *Population Growth Dynamics of Carbon Nanotubes.* ACS Nano, 2011: p. 8974-8989.
43. Hata, K., et al., *Water-Assisted Highly Efficient Synthesis of Impurity-Free Single-Walled Carbon Nanotubes.* Science, 2004. **306**(5700): p. 1362.
44. Zhong, G., et al., *Growth of Ultrahigh Density Single-Walled Carbon Nanotube Forests by Improved Catalyst Design.* ACS Nano, 2012. **6**(4): p. 2893-2903.
45. Abadi, P.P.S.S., et al., *Deformation response of conformally coated carbon nanotube forests.* Nanotechnology, 2013. **24**(47): p. 475707.
46. Brieland-Shoultz, A., et al., *Scaling the Stiffness, Strength, and Toughness of Ceramic-Coated Nanotube Foams into the Structural Regime.* Advanced Functional Materials, 2014. **24**(36): p. 5728-5735.
47. Pint, C.L., et al., *Three dimensional solid-state supercapacitors from aligned single-walled carbon nanotube array templates.* Carbon, 2011. **49**(14): p. 4890-4897.
48. Kumar, A., et al., *Carbon nanotube arrays decorated with multi-layer graphene-nanopetals enhance mechanical strength and durability.* Carbon, 2015. **84**: p. 236-245.
49. Jackson, J.J., et al., *Pulsed Growth of Vertically Aligned Nanotube Arrays with Variable Density.* ACS Nano, 2010. **4**(12): p. 7573-7581.
50. Lepró, X., et al., *Production and Characterization of Coaxial Nanotube Junctions and Networks of CNx/CNT.* Nano Letters, 2007. **7**(8): p. 2220-2226.
51. Davis, B.F., et al., *Electrically Conductive Hierarchical Carbon Nanotube Networks with Tunable Mechanical Response.* ACS Applied Materials & Interfaces, 2016. **8**(41): p. 28004-28011.
52. Amama, P.B., et al., *Catalyst–support interactions and their influence in water-assisted carbon nanotube carpet growth.* Carbon, 2012. **50**(7): p. 2396-2406.
53. Zhu, L., et al., *The growth of carbon nanotube stacks in the kinetics-controlled regime.* Carbon, 2007. **45**(2): p. 344-348.
54. Schindelin, J., et al., *Fiji: an open-source platform for biological-image analysis.* Nature Methods, 2012. **9**: p. 676.
55. Jorio, A., et al., *Structural (n,m) Determination of Isolated Single-Wall Carbon Nanotubes by Resonant Raman Scattering.* Physical Review Letters, 2001. **86**(6): p. 1118-1121.
56. Share, K., et al., *Surface engineering of nanomaterials for improved energy storage – A review.* Chemical Engineering Science, 2016. **154**: p. 3-19.
57. Zhang, Q., et al., *The Road for Nanomaterials Industry: A Review of Carbon Nanotube Production, Post-Treatment, and Bulk Applications for Composites and Energy Storage.* Small, 2013. **9**(8): p. 1237-1265.
58. Behabtu, N., et al., *Strong, Light, Multifunctional Fibers of Carbon Nanotubes with Ultrahigh Conductivity.* Science, 2013. **339**(6116): p. 182.
59. Dalton, A.B., et al., *Super-tough carbon-nanotube fibres.* Nature, 2003. **423**(6941): p. 703-703.
60. Qi, P., et al., *Toward Large Arrays of Multiplex Functionalized Carbon Nanotube Sensors for Highly Sensitive and Selective Molecular Detection.* Nano Letters, 2003. **3**(3): p. 347-351.
61. Manfrinato, V.R., et al., *Aberration-Corrected Electron Beam Lithography at the One Nanometer Length Scale.* Nano Letters, 2017. **17**(8): p. 4562-4567.

62. Bennett, R.D., et al., *Creating Patterned Carbon Nanotube Catalysts through the Microcontact Printing of Block Copolymer Micellar Thin Films.* Langmuir, 2006. **22**(20): p. 8273-8276.
63. Masahiko, I., et al., *Diameter-Controlled Carbon Nanotubes Grown from Lithographically Defined Nanoparticles.* Japanese Journal of Applied Physics, 2004. **43**(10B): p. L1356.
64. Duesberg, G.S., et al., *Growth of Isolated Carbon Nanotubes with Lithographically Defined Diameter and Location.* Nano Letters, 2003. **3**(2): p. 257-259.
65. Huang, Z.P., et al., *Growth of large periodic arrays of carbon nanotubes.* Applied Physics Letters, 2003. **82**(3): p. 460-462.
66. De Volder, M.F.L., et al., *Hierarchical Carbon Nanowire Microarchitectures Made by Plasma-Assisted Pyrolysis of Photoresist.* ACS Nano, 2011. **5**(8): p. 6593-6600.
67. Lee Duck, H., et al., *Hierarchically Organized Carbon Nanotube Arrays from Self-Assembled Block Copolymer Nanotemplates.* Advanced Materials, 2008. **20**(13): p. 2480-2485.
68. Li, J., et al., *Highly-ordered carbon nanotube arrays for electronics applications.* Applied Physics Letters, 1999. **75**(3): p. 367-369.
69. Polsen, E.S., A.G. Stevens, and A.J. Hart, *Laser Printing of Nanoparticle Toner Enables Digital Control of Micropatterned Carbon Nanotube Growth.* ACS Applied Materials & Interfaces, 2013. **5**(9): p. 3656-3662.
70. Papadopoulos, C. and B. Omrane, *Nanometer-scale Catalyst Patterning for Controlled Growth of Individual Single-walled Carbon Nanotubes.* Advanced Materials, 2008. **20**(7): p. 1344-1347.
71. Yemini, R., et al., *Patterning of Forests of Carbon Nanotubes (CNTs) Using Copper Overlayers as Iron Catalyst Deactivators.* The Journal of Physical Chemistry C, 2016. **120**(22): p. 12242-12248.
72. Santiago, E., M.W. Caroline, and M. Karen, *Patterning of metallic nanoparticles for the growth of carbon nanotubes.* Nanotechnology, 2008. **19**(13): p. 135306.
73. Sharma, R., et al., *Site-Specific Fabrication of Fe Particles for Carbon Nanotube Growth.* Nano Letters, 2009. **9**(2): p. 689-694.
74. Salaita, K., Y. Wang, and C.A. Mirkin, *Applications of dip-pen nanolithography.* Nature Nanotechnology, 2007. **2**: p. 145.
75. Islam, A.E., et al., *Engineering the Activity and Lifetime of Heterogeneous Catalysts for Carbon Nanotube Growth via Substrate Ion Beam Bombardment.* Nano Letters, 2014. **14**(9): p. 4997-5003.
76. Amama, P.B., et al., *Influence of Alumina Type on the Evolution and Activity of Alumina-Supported Fe Catalysts in Single-Walled Carbon Nanotube Carpet Growth.* ACS Nano, 2010. **4**(2): p. 895-904.
77. Amama, P.B., et al., *Role of Water in Super Growth of Single-Walled Carbon Nanotube Carpets.* Nano Letters, 2009. **9**(1): p. 44-49.
78. Amama, P.B., et al., *Understanding properties of engineered catalyst supports using contact angle measurements and X-Ray reflectivity.* Nanoscale, 2016. **8**(5): p. 2927-2936.
79. Yang, N., et al., *A Forest of Sub-1.5-nm-wide Single-Walled Carbon Nanotubes over an Engineered Alumina Support.* Scientific Reports, 2017. **7**: p. 46725.
80. Carpena-Núñez, J., et al., *Water-assisted, electron-beam induced activation of carbon nanotube catalyst supports for mask-less, resist-free patterning.* Carbon, 2018.

81. Nabity, J.C. *Nanometer Pattern Generation System*. 2018; Direct Write Lithography using a commercial Electron Beam or Ion Beam Microscope]. Available from: http://www.jcnabity.com/.
82. Myers, B.D. and V.P. Dravid, *Variable Pressure Electron Beam Lithography (VP-eBL): A New Tool for Direct Patterning of Nanometer-Scale Features on Substrates with Low Electrical Conductivity.* Nano Letters, 2006. **6**(5): p. 963-968.
83. van den Brand, J., et al., *Correlation between hydroxyl fraction and O/Al atomic ratio as determined from XPS spectra of aluminium oxide layers.* Surface and Interface Analysis, 2004. **36**(1): p. 81-88.
84. Royall, C.P., B.L. Thiel, and A.M. Donald, *Radiation damage of water in environmental scanning electron microscopy.* Journal of Microscopy, 2001. **204**(3): p. 185-195.
85. Egerton, R.F., *Mechanisms of radiation damage in beam-sensitive specimens, for TEM accelerating voltages between 10 and 300 kV.* Microscopy Research and Technique, 2012. **75**(11): p. 1550-1556.
86. Egerton, R.F., P. Li, and M. Malac, *Radiation damage in the TEM and SEM.* Micron, 2004. **35**(6): p. 399-409.
87. Stevens-Kalceff, M.A., *Electron-Irradiation-Induced Radiolytic Oxygen Generation and Microsegregation in Silicon Dioxide Polymorphs.* Physical Review Letters, 2000. **84**(14): p. 3137-3140.
88. Knotek, M.L. and P.J. Feibelman, *Ion Desorption by Core-Hole Auger Decay.* Physical Review Letters, 1978. **40**(14): p. 964-967.
89. Ichimura, S. and R. Shimizu, *Observation of electron beam damage in thin-film SiO2 on Si with scanning Auger electron microscope.* Journal of Applied Physics, 1979. **50**(9): p. 6020-6022.
90. Knotek, M.L. and P.J. Feibelman, *Stability of ionically bonded surfaces in ionizing environments.* Surface Science, 1979. **90**(1): p. 78-90.
91. Moroño, A., E.R. Hodgson, and S.M. González de Vicente, *Electrical surface degradation of electron irradiated sapphire and silica.* Journal of Nuclear Materials, 2009. **386-388**: p. 1002-1005.
92. Mochel, M.E., et al., *Electron beam cutting in amorphous alumina sheets.* Applied Physics Letters, 1984. **44**(5): p. 502-504.
93. Mochel, M.E., et al., *Electron beam writing on a 20-Å scale in metal β-aluminas.* Applied Physics Letters, 1983. **42**(4): p. 392-394.
94. Pells, G.P. and D.C. Phillips, *Radiation damage of α-Al2O3 in the HVEM: II. Radiation damage at high temperature and high dose.* Journal of Nuclear Materials, 1979. **80**(2): p. 215-222.
95. Martin, A.A., G. McCredie, and M. Toth, *Electron beam induced etching of carbon.* Applied Physics Letters, 2015. **107**(4): p. 041603.
96. Stevens-Kalceff, M.A., *Micromodification of silicon dioxide in a variable pressure/environmental scanning electron microscope.* Applied Physics Letters, 2001. **79**(19): p. 3050-3052.
97. Yuzvinsky, T.D., et al., *Precision cutting of nanotubes with a low-energy electron beam.* Applied Physics Letters, 2005. **86**(5): p. 053109.
98. Le Caër, S., *Water Radiolysis: Influence of Oxide Surfaces on H2 Production under Ionizing Radiation.* Water, 2011. **3**(1).

99. Kern, P., et al., *Local electron beam induced reduction and crystallization of amorphous titania films.* Applied Physics Letters, 2006. **89**(2): p. 021902.
100. Solá, F., et al., *Growth and characterization of branched carbon nanostructures arrays in nano-patterned surfaces from porous silicon substrates.* Micron, 2009. **40**(1): p. 80-84.
101. Meyza, X., et al., *Secondary electron emission and self-consistent charge transport and storage in bulk insulators: Application to alumina.* Journal of Applied Physics, 2003. **94**(8): p. 5384-5392.
102. Kern, P., et al., *Electron-Beam-Induced Topographical, Chemical, and Structural Patterning of Amorphous Titanium Oxide Films.* The Journal of Physical Chemistry B, 2006. **110**(47): p. 23660-23668.
103. Kupcik, T., et al., *Macroscopic and spectroscopic investigations on Eu(III) and Cm(III) sorption onto bayerite (β-Al(OH)3) and corundum (α-Al2O3).* Journal of Colloid and Interface Science, 2016. **461**: p. 215-224.
104. Zhang, W. and J.R. Smith, *Nonstoichiometric Interfaces and Al2O3 Adhesion with Al and Ag.* Physical Review Letters, 2000. **85**(15): p. 3225-3228.
105. Łodziana, Z. and J.K. Nørskov, *Adsorption of Cu and Pd on α-Al2O3(0001) surfaces with different stoichiometries.* The Journal of Chemical Physics, 2001. **115**(24): p. 11261-11267.
106. Wischert, R., et al., *γ-Alumina: The Essential and Unexpected Role of Water for the Structure, Stability, and Reactivity of "Defect" Sites.* Journal of the American Chemical Society, 2012. **134**(35): p. 14430-14449.
107. Hirunsit, P., C. Luadthong, and K. Faungnawakij, *Effect of alumina hydroxylation on glycerol hydrogenolysis to 1,2-propanediol over Cu/Al2O3: combined experiment and DFT investigation.* RSC Advances, 2015. **5**(15): p. 11188-11197.
108. Burgos, J.C., E. Jones, and P.B. Balbuena, *Effect of the Metal−Substrate Interaction Strength on the Growth of Single-Walled Carbon Nanotubes.* The Journal of Physical Chemistry C, 2011. **115**(15): p. 7668-7675.
109. Lim, K.Y., et al., *Laser Pruning of Carbon Nanotubes as a Route to Static and Movable Structures.* Advanced Materials, 2003. **15**(4): p. 300-303.
110. Sears, K., et al., *Focused ion beam milling of carbon nanotube yarns to study the relationship between structure and strength.* Carbon, 2010. **48**(15): p. 4450-4456.
111. Labunov, V., et al., *Femtosecond laser modification of an array of vertically aligned carbon nanotubes intercalated with Fe phase nanoparticles.* Nanoscale Research Letters, 2013. **8**(1): p. 375.
112. Raghuveer, M.S., et al., *Nanomachining carbon nanotubes with ion beams.* Applied Physics Letters, 2004. **84**(22): p. 4484-4486.
113. Zobelli, A., et al., *Electron knock-on cross section of carbon and boron nitride nanotubes.* Physical Review B, 2007. **75**(24): p. 245402.
114. Banhart, F., J. Li, and M. Terrones, *Cutting Single-Walled Carbon Nanotubes with an Electron Beam: Evidence for Atom Migration Inside Nanotubes.* Small, 2005. **1**(10): p. 953-956.
115. Smith, B.W. and D.E. Luzzi, *Electron irradiation effects in single wall carbon nanotubes.* Journal of Applied Physics, 2001. **90**(7): p. 3509-3515.
116. Krasheninnikov, A.V., et al., *Stability of carbon nanotubes under electron irradiation: Role of tube diameter and chirality.* Physical Review B, 2005. **72**(12): p. 125428.

117. Liu, P., F. Arai, and T. Fukuda, *Cutting of carbon nanotubes assisted with oxygen gas inside a scanning electron microscope.* Applied Physics Letters, 2006. **89**(11): p. -.
118. Lassiter, M.G. and P.D. Rack, *Nanoscale electron beam induced etching: a continuum model that correlates the etch profile to the experimental parameters.* Nanotechnology, 2008. **19**(45): p. 455306.
119. Brown, J., B.F. Davis, and M.R. Maschmann, *Precision Milling of Carbon Nanotube Forests Using Low Pressure Scanning Electron Microscopy.* JoVE, 2017(120): p. e55149.
120. Almkhelfe, H., et al., *Gaseous product mixture from Fischer-Tropsch synthesis as an efficient carbon feedstock for low temperature CVD growth of carbon nanotube carpets.* Nanoscale, 2016. **8**(27): p. 13476-13487.
121. Oliver, C.R., et al., *Statistical Analysis of Variation in Laboratory Growth of Carbon Nanotube Forests and Recommendations for Improved Consistency.* ACS Nano, 2013. **7**(4): p. 3565-3580.
122. Pathak, S., J.R. Raney, and C. Daraio, *Effect of morphology on the strain recovery of vertically aligned carbon nanotube arrays: An in situ study.* Carbon, 2013. **63**: p. 303-316.
123. Suhr, J., et al., *Fatigue resistance of aligned carbon nanotube arrays under cyclic compression.* Nature Nanotechnology, 2007. **2**(7): p. 417-21.
124. Abadi, P.P.S.S., et al., *Buckling-driven delamination of carbon nanotube forests.* Applied Physics Letters, 2013. **102**(22): p. 223103.
125. Correlated Solutions, I. *VIC-2D 6*. 2018; Available from: http://correlatedsolutions.com/vic-2d/.